

**EXPLORING THE TRADE SPACE FOR TWO-MANEUVER
TRANSFERS FROM EARTH TO CISLUNAR LIBRATION
POINT ORBITS**

by

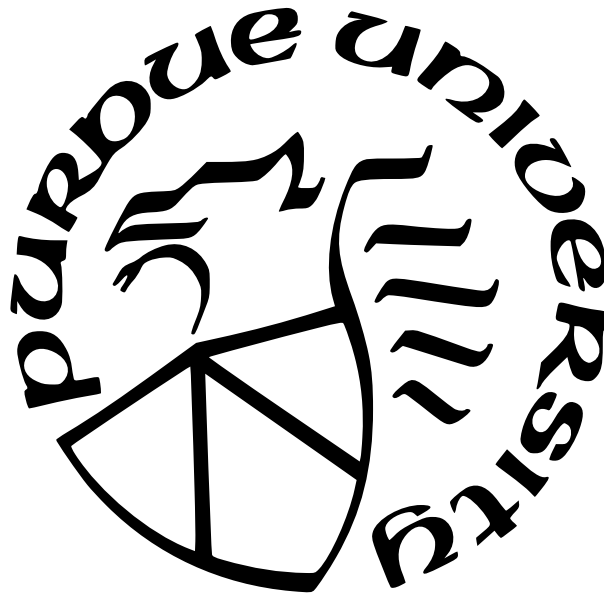
Ricardo Gomez

A Thesis

Submitted to the Faculty of Purdue University

In Partial Fulfillment of the Requirements for the degree of

Master of Science in Aeronautics and Astronautics



School of Aeronautics and Astronautics

West Lafayette, Indiana

December 2021

**THE PURDUE UNIVERSITY GRADUATE SCHOOL
STATEMENT OF COMMITTEE APPROVAL**

Dr. Kathleen Howell, Chair

School of Aeronautics and Astronautics

Dr. Carolin Frueh

School of Aeronautics and Astronautics

Dr. James Longuski

School of Aeronautics and Astronautics

Approved by:

Dr. Gregory A. Blaisdell

Para Joche:
A seguir explorando contigo

ACKNOWLEDGMENTS

Primero que nada, tengo que agradecer a mi papa y a mi mama por todo el apoyo que me han dado; sé que tomar la decisión, de dejar atrás todo lo que habían construido y empezar de nuevo, no pudo haber sido fácil, pero nos ha puesto en una mejor posición como familia y me dio la oportunidad de estudiar ingeniería aeroespacial y astrodinámica. Aparte de eso, estoy agradecido de que hayan tomado la iniciativa sobre nuestra educación, siendo parte de la fundación de Los Caminos; un colegio que sin duda me preparo para aprovechar estas oportunidades académicas cuando se presentaron. Doy las gracias también a mi madrina Mariela por haberme dado la oportunidad de estudiar en Purdue; un sitio que 7 años más tarde me sigue enseñando cosas nuevas. Por supuesto, le doy las gracias también al resto de mi familia. He sido muy afortunado de haber contado con el apoyo de todos ustedes.

I am extremely grateful for my advisor, Professor Kathleen C. Howell. A professor that is equally focused on expanding the research in her field and preparing the next generation of engineers; your dedication to teaching is admirable and not something I take for granted. More importantly, your willingness to prioritize the well being of your students is everything one would hope from a mentor; your flexibility, understanding, and support during difficult times means a lot to both myself and my family, and we are deeply grateful. I am fortunate to be a part of your research group, and I look forward to continuing this endeavor.

Next, I would like to also thank my friends. To current and past members of our research group, thank you for all the collaboration and support provided. The atmosphere that has been developed within this group is exceptional and I hope to continue it moving forward. To my friends from undergrad, Brandt, Will, Schmidtty and the rest of BAAEs and the Chutmey; your continued support these past few years has helped me overcome this task. To Wayne Schlei, who became a friend and mentor as he provided advice about the inner workings of the resarch group and industry; I thank you for your support. To my girlfriend Rachel, thank you for being by my side for these past 3 years. Having you as my partner has been a privilege and I appreciate your support in the good times and the bad. I hope we can continue supporting each other as we pursue these challenges in the future.

I would also like to thank my committee members, Professors Carolin Frueh and James Longuski. I appreciate you taking the time out of your busy schedule to review my work and provide valuable feedback. Additionally, your teachings and support, from my time as an undergraduate to now, have been particularly valuable and I thank you for that. Finally I would like to thank the Purdue School of Aeronautics and Astronautics, Dr. Waterloo Tsutsui and The Aerospace Corporation Award No.: 21013643 for providing the funding necessary to achieve the work presented.

TABLE OF CONTENTS

LIST OF FIGURES	8
ABSTRACT	11
1 INTRODUCTION	12
1.1 Previous Contributions	12
1.2 Document Overview	13
2 SYSTEM MODELS	15
2.1 The Circular Restricted Three-Body Problem	15
2.1.1 Equations of Motion	15
2.1.2 Jacobi Constant	22
2.1.3 Equilibrium Solutions	23
2.1.4 Zero Velocity Surfaces	25
3 DYNAMICAL SYSTEMS THEORY	27
3.1 Linear Variational Equations and Motion Near the Equilibrium Points	27
3.2 State Transition Matrix	32
3.3 Differential Corrections	34
3.3.1 Single Shooter Application to Periodic Orbits in CRTBP	37
3.4 Continuation Methods	38
3.4.1 Natural Parameter Continuation	38
3.4.2 Natural Parameter Continuation Application to Periodic Orbits in CRTBP	39
3.5 Stability of Periodic Orbits	40
3.5.1 Invariant Manifold Theory	41
3.5.2 Bifurcation Theory	42
Other Period Multiplying Bifurcations	45
3.6 Other topics to consider	47

4	TRANSFERS TO THE EARTH-MOON L_1 VICINITY	48
4.1	Transfers with Direct Insertion into Baseline Orbit	48
4.2	Transfers Leveraging Stable Manifolds of Baseline Orbit	52
4.2.1	Tangent Vs Non-Tangent Insertion Transfers	52
4.2.2	Expanding Beyond Baseline Orbit	61
4.3	Expanding Transfer Trade Space on Regions of Interest	66
	Continuation Methodology	67
	Transfer Solutions	68
4.3.1	Continuation to Alternate Manifold Arcs on Single Orbit	74
	Continuation Methodology	75
	Transfer Results	75
4.3.2	Continuation to Similar Manifold Arcs on Additional Orbits Along the Family	81
	Continuation Method	82
	Transfer Solutions	84
4.3.3	Continuation to Several Manifold Arcs Along Family of Orbits	88
	Continuation Methodology	88
	Transfer Solutions	90
5	SUMMARY AND FUTURE WORK	94
5.1	Investigation Summary	94
5.2	Future work	95
	REFERENCES	97

LIST OF FIGURES

2.1	Three-Body Problem Inertial Frame Definition	17
2.2	Rotating Frame Definition	18
2.3	Equilibrium Points in the Rotating Frame	25
2.4	ZVCs at a range of energy levels in the Earth-Moon system	26
3.1	Linear oscillatory behavior in L_1 vicinity of Earth-Moon CRTBP	32
3.2	Initial guess (blue) and corrected (red) L_1 Lyapunov orbit in Earth-Moon system	38
3.3	Lyapunov orbit families in the Earth-Moon system	40
3.4	L_1 Lyapunov orbit invariant manifolds in the Earth-Moon system	42
3.5	Eigenvalue behavior for different types of bifurcations, visualized on unit circle .	44
3.6	L_1 and L_2 Halo orbit family in Earth-Moon system	45
3.7	L_2 Halo 5-period orbit bifurcating families	46
4.1	Tangent insertion options	49
4.2	Transfers to L_1 Lyapunov orbits perpendicular crossings	49
4.3	Tangent transfers to baseline orbit	50
4.4	Departure angle definition	50
4.5	Tangent transfer characteristics to baseline orbit	51
4.6	Left half-manifold arcs of baseline orbit	52
4.7	Stable right half-manifold arcs of baseline orbit	53
4.8	Tangential transfers to stable left half-manifold arc of baseline orbit	54
4.9	Tangential transfers to stable right half-manifold arc of baseline orbit	55
4.10	Insertion location along manifold arc	56
4.11	Insertion angle definition	56
4.12	Insertion ΔV comparison	57
4.13	Insertion ΔV comparison	57
4.14	Transfer arc JC comparison	58
4.15	JC variation along 500 km LEO with 3 km/s TLI	59
4.16	Transfer arc TLI comparison	60
4.17	Departure angle (θ) comparison	61

4.18	Left half-manifold of L_1 Lyapunov orbits	62
4.19	Selected left half-manifold arcs	62
4.20	Transfer characteristics for left half-manifold arcs of alternate L_1 Lyapunov orbits	63
4.21	Selected left half-manifold arcs	64
4.22	Transfer characteristics for right half-manifold arcs of alternate L_1 Lyapunov orbits	65
4.23	Near orbit ROI for baseline orbit	67
4.24	Sample transfers to baseline orbit ROI	68
4.25	Insertion ΔV for ROI	69
4.26	Trans-Lunar Injection for ROI	69
4.27	Maneuver characteristics for ROI	70
4.28	Departure angle for ROI	70
4.29	Apoapse ROI definition visualization	71
4.30	Sample transfers to baseline orbit apogee ROI	71
4.31	Transfer characteristics for apoapse ROI of baseline orbit	72
4.32	Maneuver characteristics for apoapse ROI	73
4.33	Insertion angle variation for apoapse ROI	74
4.34	Solution surface evolution for different manifold arcs of baseline orbit	76
4.35	Insertion ΔV for ROI	77
4.36	Trans-Lunar Injection for ROI	77
4.37	Departure angle for ROI	78
4.38	Insertion cost of solutions at various departure angles	78
4.39	Insertion ΔV for apoapse ROI	79
4.40	TLI for apoapse ROI	80
4.41	Departure angle for apoapse ROI	80
4.42	Insertion cost of solutions at various departure angles	81
4.43	Similar manifold arcs along L_1 Lyapunov family	82
4.44	Solution surface evolution for manifold arcs of varying orbits	83
4.45	Insertion ΔV for ROI	84
4.46	Trans-Lunar Injection for ROI	85
4.47	Departure angle for ROI	85

4.48	Surface variation along L_1 Lyapunov family	86
4.49	Transfer characteristics for apoapse ROI of various orbit	87
4.50	Solution volume evolution for manifold arcs of varying orbits	89
4.51	Insertion ΔV along L_1 Lyapunov family	90
4.52	TLI along L_1 Lyapunov family	91
4.53	Departure angle along L_1 Lyapunov family	91
4.54	Transfer characteristics for apoapse ROI along L_1 Lyapunov family	92
4.55	Insertion cost of solutions at various departure angles	93

ABSTRACT

In recent times, as the National Aeronautics and Space Administration (NASA) focuses on establishing a sustained presence in cislunar space, there has been an increase in planned missions to the cislunar vicinity for lunar exploration. Due to this increase in planned missions, the use of cislunar structures available in the Circular Restricted Three-Body Problem (CRTBP) has become of greater interest. Traditionally, transfers that leverage CRTBP structures in the cislunar vicinity have been generated as point designs. As a consequence of the non-linearity of this model, transitioning these point designs to other epochs or mission scenarios is non-trivial. Hence, a trade space of transfer solutions, that leverage the underlying dynamics, is of interest for rapid mission design. In this study, numerical methods and dynamical systems theory are leveraged to extract available dynamical structures in the model, which are subsequently exploited for transfer design. A trade space of relatively low time of flight, two-maneuver transfers, from a 500 km altitude Low Earth Orbit (LEO) to the Earth-Moon L_1 Lyapunov orbit family is generated and analyzed.

1. INTRODUCTION

The exploration of structures in the Earth-Moon Circular Restricted Three-Body Problem (CRTBP) near the cislunar region is of great interest. The ARTEMIS mission (THEMIS continuation) was the first mission to successfully leverage Earth-Moon CRTBP dynamical structures in space [1]. Since, multiple missions that leverage such structures in the Earth-Moon system have been proposed [2][3][4]. Mainly, the National Aeronautics and Space Administration (NASA) has identified one of these dynamical structures in cislunar space as the target orbit for its gateway program [5]. It follows, that, to support the gateway program and lunar exploration, an increase of missions to cislunar space is forthcoming. Transfer design to the cislunar vicinity has frequently been achieved by generating reference trajectories as point designs. Due to the non-linearity of the CRTBP, these solutions are not easily transitioned to different mission scenarios, leading to mission designers having to restart the design process; or if the previous arc meets the mission constraints, the same solution will be reused, even if transfer solutions that better suit the mission's needs exist. Consequently, a trade space of transfer solutions that leverage the underlying dynamics and allows for rapid, informed, mission design is of interest. A trade space of two-maneuver transfer solutions from Low Earth Orbit (LEO) to the Earth-Moon L_1 Lyapunov family is generated and evaluated in this study, as to identify preferable solutions that leverage the underlying dynamics of the model.

1.1 Previous Contributions

Multiple authors have considered transfers from the Earth to CRTBP structures in the cislunar vicinity. Recently, Pritchett evaluated transfer trajectories to lunar orbits leveraging low-thrust for the Lunar IceCube mission [6], Zimovan-Spreen focused on trajectories that transit towards the orbit selected for the gateway program, by leveraging structures of higher period orbits in the target orbits vicinity [7], and Scheuerle investigated ballistic lunar transfers that leverage the solar perturbation to reduce insertion cost into their target orbit [8]. More specifically, several authors have focused on interior, two-maneuver, transfers from Earth to the cislunar vicinity. Rausch evaluated direct transfers from an Earth

parking orbit to Halo orbits in cislunar space[9], Folta evaluated design considerations for direct transfers to periodic and quasi-periodic orbits in the L_1 and L_2 vicinity [10], while, Dunham et al. and Jesick focused on direct insertion transfers with free return possibilities for human exploration missions [11][12]. In 2008, Parker and Born conducted an extensive study of two-maneuver transfers to L_1 and L_2 Halo orbits, focused on both direct insertion transfers and transfers that leverage the target orbits stable manifold, while comparing the benefits of trading time of flight for maneuver cost [13]. An extension of this problem was conducted by Pavlak in 2013, with a focus on three-maneuver and free return transfers [14]. Additional authors have also evaluated this problem[15][16][17]. The work presented here is not an all encompassing list, but merely a representative set of the previous contributions available. These previous studies provide insight into available transfer solutions and guide the transfer generation process followed in this study.

1.2 Document Overview

The focus of this study is to construct and analyze transfers from LEO to the L_1 Lyapunov family. This document is structured to that end, as:

- **Chapter 2:** The dynamical model implemented in the study is described in this chapter. While the general gravitational field acting on a particle of interest is defined by the N-body problem, the lower fidelity CRTBP is used in order to uncover useful structures for transfer design. This model possesses an integral of the motion, and a set of 5 equilibrium solutions, which provide insight into the motion available.
- **Chapter 3:** To analyze motion in the CRTBP, numerical tools leveraging dynamical systems theory are implemented. The linear variational equations are leveraged to realize linear motion in the vicinity of the equilibrium points. The State Transition Matrix (STM) allows for the study of stability information of reference trajectories. Differential corrections facilitates the transition from these linear predictions into the full non-linear model. Additionally, differential corrections allows for the targeting of desired conditions in a given trajectory, a capability that is leveraged in transfer design. Continuation methods are exploited to expand on the set of available solutions,

and generate a more complete picture. Finally, the stability characteristics of periodic orbits in this model are utilised to uncover helpful dynamical structures in their vicinity.

- **Chapter 4:** This chapter focuses on the generation and evaluation of relatively low time of flight transfer solutions from LEO to the L_1 Lyapunov family. Transfers that insert directly into the target orbit are analyzed before expanding the space to include insertion into stable manifolds of said orbit. Next, the performance of tangent and non-tangent insertion transfers is compared. Locations along the stable manifold that provide transfers with low-cost insertion maneuvers are identified as Regions of Interest (ROI). Finally, the solution space in these ROIs is expanded to additional manifold arcs on a given orbit, and to other orbits in the same family, to generate a representative set of the transfers available to this family of orbits, for the times of flight analyzed.
- **Chapter 5:** The final chapter provides an overview of the presented results in the form of key takeaways. Additionally, a road map of future work to expand this study is included.

2. SYSTEM MODELS

The two-body problem is a model that includes two isolated bodies moving under their mutual gravitational attraction. It is assumed that both bodies are centrobaric. The two-body problem is well known and possesses analytical solutions that are leveraged for dynamical analysis in space mission design. A model that includes three or more bodies is more complex, where the influence of the mutual gravitational forces govern the behavior. The inclusion of an additional body results in a mathematical model that does not possess an analytical solution. While more complex, this model provides distinct dynamical structures that are not available in the lower-fidelity two-body model and which potentially offer unique options for cislunar mission design.

2.1 The Circular Restricted Three-Body Problem

A model that leverages the mutual gravitational influence of three celestial bodies is known as the three-body problem. If one of the bodies possesses a mass that is negligible in comparison to the other two bodies, a simplified version of this model emerges and is denoted the Circular Restricted Three-Body Problem (CRTBP). The CRTBP provides additional insight into the motion of the infinitesimal body as a particle of interest. With the two bodies of finite mass exhibiting Keplerian motion, a new set of differential equations governs a wide variety of behaviors for the particle of interest. However, with no analytical solution, the motion of the infinitesimal body is necessarily explored via numerical integration. Dynamical systems theory also offers some understanding of the fundamental structures in the problem that influence the behavior. The motion governed in this dynamical regime, and the underlying structures in cislunar space, are currently of great interest. To analyze the motion in this model, the equations of motion are first derived.

2.1.1 Equations of Motion

To derive the equations of motion in the CRTBP, begin with the more general N-body problem (NBP). The NBP models the gravitational force of N-1 bodies on a single body in

the system to examine their influence on the subsequent evolution of its path. Assume that all the bodies are centrobaric and, thus, are represented as particles. Then, the force vector due to a single gravity field on the particle of interest [18] is defined as

$$\vec{f}_{ij} = Gm_i \frac{m_j \vec{r}_{ij}}{r_{ij}^3} \quad (2.1)$$

where G is the universal gravitational constant, m_i and m_j are the masses of the particle of interest and one of the $N-1$ gravitational bodies, respectively, and \vec{r}_{ij} is the position vector of the particle i relative to particle j . Combining the gravitational influence of all other $N-1$ gravitational bodies on particle i leads to the resultant force, i.e.,

$$\vec{f}_i = \sum_{j=1}^{N-1} \vec{f}_{ij} = Gm_i \sum_{j=1}^{N-1} \frac{m_j \vec{r}_{ij}}{r_{ij}^3} \quad (2.2)$$

It then follows from equation (2.2) that the force on an individual particle in the general three-body problem is simply

$$\vec{f}_i = Gm_i \sum_{j=1}^2 \frac{m_j \vec{r}_{ij}}{r_{ij}^3} = Gm_i \left(\frac{m_1 \vec{r}_{i1}}{r_{i1}^3} + \frac{m_2 \vec{r}_{i2}}{r_{i2}^3} \right) \quad (2.3)$$

The CRTBP then is comprised of 3 total bodies; P_1 , the larger celestial body (mass m_1), P_2 , the smaller celestial body (mass m_2), and P_3 , the particle of interest of mass m_3 (i.e., a spacecraft, for example). It is assumed that the mass of P_3 is negligible in comparison to the masses of P_1 and P_2 , hence, the motion of P_1 and P_2 is defined by two-body Keplerian dynamics. An inertial frame centered on the barycenter B is then defined. The inertial $\hat{X} - \hat{Y}$ plane represents the P_1 and P_2 orbital plane as:

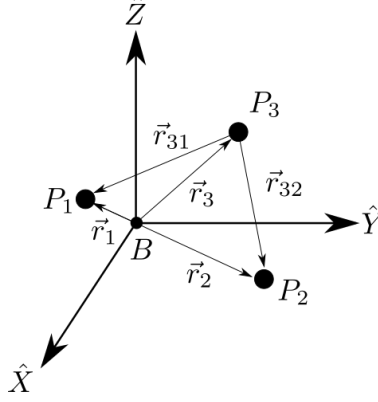


Figure 2.1. Three-Body Problem Inertial Frame Definition

The force experienced by an object of constant mass is equal to its mass times its acceleration ($\vec{F} = m\vec{a}$) [18]. Using $\dot{\vec{r}}$ and $\ddot{\vec{r}}$ to represent the first and second time derivatives of \vec{r} , respectively, equation (2.3) is rewritten in the form

$$m_3\ddot{\vec{r}}_3 = -G \left(\frac{m_3m_1}{r_{13}^3} \vec{r}_{13} + \frac{m_3m_2}{r_{23}^3} \vec{r}_{23} \right) \quad (2.4)$$

The model is, then, further simplified by assuming circular motion of the primaries about B , so that the distance between P_1 and P_2 remains fixed. A rotating frame is defined, given B as the origin, which moves with the motion of the primaries P_1 and P_2 , such that the unit vector \hat{x} is defined along the line from P_1 to P_2 , \hat{z} is parallel to the direction of the angular momentum vector for the orbit of the primaries, and \hat{y} completes the orthonormal set as apparent in Figure 2.2.

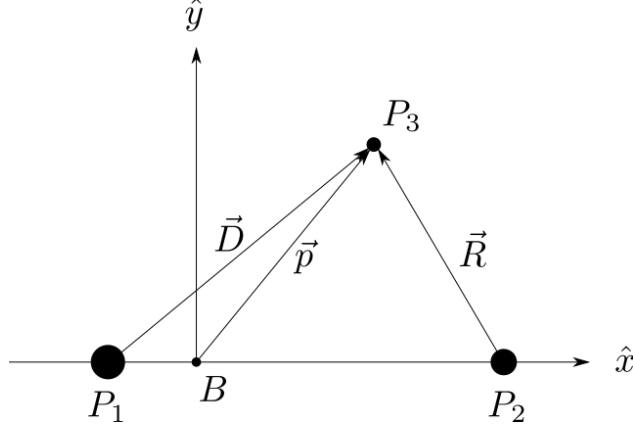


Figure 2.2. Rotating Frame Definition

Notice that P_1 and P_2 are fixed points in the rotating frame. Given the definitions in Figure 2.2, equation (2.4) is rewritten as follows

$$\ddot{\vec{p}} = -G \frac{m_1}{D^3} \vec{D} - G \frac{m_2}{R^3} \vec{R} \quad (2.5)$$

For convenience, and to expand their use, the equations of motion are non-dimensionalized by exploiting a set of characteristic quantities. The characteristic quantities are defined for the fundamental properties of length, mass and time. For the characteristic length, l^* , the semimajor axis of the orbit of P_2 about P_1 is typically employed. The sum of the primary masses, m_1 and m_2 , is leveraged as the characteristic mass, m^* . Finally, the characteristic time, t^* , is defined such that the nondimensional gravitational constant $G_{non-dim}$ is equal to one. In summary:

$$l^* = r_1 + r_2$$

$$m^* = m_1 + m_2$$

$$t^* = \sqrt{\frac{l^{*3}}{Gm^*}}$$

Now, convenient nondimensional quantities are defined; the nondimensional primary masses are

$$\mu = \frac{m_2}{m^*}$$

$$1 - \mu = \frac{m_1}{m^*}$$

The nondimensional position vectors for the infinitesimal mass, P_3 , relative to the primaries are denoted

$$\vec{r} = \frac{\vec{R}}{l^*} \quad \text{and} \quad \vec{d} = \frac{\vec{D}}{l^*}$$

Then, the non-dimensional position of P_3 with respect to the barycenter is defined

$$\vec{\rho} = \frac{\vec{p}}{l^*} = x\hat{x} + y\hat{y} + z\hat{z}$$

where the nondimensional components in terms of the rotating frame are x , y , and z . The position vectors for the primaries relative to the barycenter are then expressed as

$$\vec{r}_1 = -\mu\hat{x}$$

$$\vec{r}_2 = (1 - \mu)\hat{x}$$

The nondimensional position of P_3 relative to P_1 and P_2 , \vec{d} and \vec{r} are decomposed into

$$\vec{d} = (x + \mu)\hat{x} + y\hat{y} + z\hat{z}$$

$$\vec{r} = (x - 1 + \mu)\hat{x} + y\hat{y} + z\hat{z}$$

Finally, G , the mean motion (N) and time are non-dimensionalized using

$$G_{non-dim} = \frac{G}{(l^*)^3} m^* (t^*)^2 = 1$$

$$N = \sqrt{\frac{G(m_1 + m_2)}{a_{dim}^3}} = \sqrt{\frac{Gm^*}{a(l^*)^3}} = \sqrt{\frac{Gm^*}{(l^*)^3}}$$

$$n = Nt^* = \sqrt{\frac{Gm^*}{(l^*)^3}} \sqrt{\frac{(l^*)^3}{Gm^*}} = 1$$

$$\tau = \frac{t}{t^*}$$

where n and τ are the nonsimensional mean motion and time, respectively. The classical equations of motion are produced as the characteristic quantities are introduced into equation (2.5) and yield

$$\frac{d^2 \vec{\rho}}{d\tau^2} = \ddot{\vec{\rho}} = -(1 - \mu) \frac{\vec{d}}{d^3} - \mu \frac{\vec{r}}{r^3} \quad (2.6)$$

Note, the dots represent derivatives with respect to nondimensional time, τ . The left side of the previous expression requires a kinematic expansion to derive the equation of motion. Recall

$$\vec{\rho} = \frac{\vec{p}}{l^*} = x\hat{x} + y\hat{y} + z\hat{z}$$

and, since this vector quantity is defined in a rotating frame, its time derivative is derived from the basic kinematic equation as

$${}^i\dot{\vec{\rho}} = {}^r\dot{\vec{\rho}} + {}^i\vec{\omega}^r \times \vec{\rho}$$

$${}^i\dot{\vec{\rho}} = \dot{x}\hat{x} + \dot{y}\hat{y} + \dot{z}\hat{z} + (n\hat{z}) \times (x\hat{x} + y\hat{y} + z\hat{z})$$

$${}^i\dot{\vec{\rho}} = (\dot{x} - ny)\hat{x} + (\dot{y} + nx)\hat{y} + \dot{z}\hat{z}$$

where ${}^i\dot{\vec{\rho}}$ is the derivative with respect to the inertial frame, ${}^r\dot{\vec{\rho}}$ is the derivative with respect to the rotating frame and ${}^i\vec{\omega}^r = n\hat{z}$ is the rate at which the rotating frame rotates with respect to the inertial frame. Similarly

$${}^i\ddot{\vec{\rho}} = {}^r\ddot{\vec{\rho}} + {}^i\vec{\omega}^r \times \dot{\vec{\rho}}$$

$${}^i\ddot{\vec{\rho}} = (\ddot{x} - n\dot{y})\hat{x} + (\ddot{y} + n\dot{x})\hat{y} + \ddot{z}\hat{z} + (n\hat{z}) \times ((\dot{x} - ny)\hat{x} + (\dot{y} + nx)\hat{y} + \dot{z}\hat{z})$$

$${}^i\ddot{\vec{\rho}} = (\ddot{x} - 2n\dot{y} - n^2x)\hat{x} + (\ddot{y} + 2n\dot{x} - n^2y)\hat{y} + \ddot{z}\hat{z} \quad (2.7)$$

Finally equations (2.6) and (2.7) are combined, and yield three scalar equations such that

$$\ddot{x} - 2n\dot{y} - n^2x = -\frac{(1-\mu)(x+\mu)}{d^3} - \frac{\mu(x-1+\mu)}{r^3} \quad (2.8)$$

$$\ddot{y} + 2n\dot{x} - n^2y = -\frac{(1-\mu)y}{d^3} - \frac{\mu y}{r^3} \quad (2.9)$$

$$\ddot{z} = -\frac{(1-\mu)z}{d^3} - \frac{\mu z}{r^3} \quad (2.10)$$

Additionally, the equations of motion are further simplified by introducing the pseudo-potential function as

$$U^* = \frac{1-\mu}{d} + \frac{\mu}{r} + \frac{n^2(x^2 + y^2)}{2} \quad (2.11)$$

which is employed to rewrite the equations of motion as follows

$$\ddot{x} - 2n\dot{y} = U_x^* \quad (2.12)$$

$$\ddot{y} + 2n\dot{x} = U_y^* \quad (2.13)$$

$$\ddot{z} = U_z^* \quad (2.14)$$

where U_i^* represents the partial derivative of the pseudo-potential function with respect to state i , $\frac{\partial U^*}{\partial q_i}$. Finally, if an initial position and velocity state is in the x-y plane and $\dot{z}_0 = 0$, it remains in the x-y plane, as \ddot{z} equals zero for the entire trajectory.

2.1.2 Jacobi Constant

Integrals of the motion offer further insight into potential structures in the CRTBP. Previous authors have successfully determined an integral of the motion in the CRTBP[19]. This integral of the motion emerges as an energy-like constant, denoted the Jacobi Constant (JC). To produce an expression for this integral of the motion, operate on the differential equations such that a scalar equation can be integrated. Begin by leveraging the dot product between $\dot{\vec{\rho}}$ and $\ddot{\vec{\rho}}$, computed such that

$$\dot{\vec{\rho}} \cdot \ddot{\vec{\rho}} = \dot{x}\ddot{x} + \dot{y}\ddot{y} + \dot{z}\ddot{z} = U_x^*\dot{x} + U_y^*\dot{y} + U_z^*\dot{z}$$

Since the model is time-independent, the right side of the equation represents the total time derivative of the pseudo-potential ($\frac{dU^*}{d\tau}$). Then, integrating the scalar dot product results in

$$\frac{\dot{x}^2 + \dot{y}^2 + \dot{z}^2}{2} = U^* + \text{constant}$$

$$\mathbf{v}^2 = 2U^* - JC \quad (2.15)$$

$$JC = 2U^* - \mathbf{v}^2 \quad (2.16)$$

where \mathbf{v} is the magnitude of the velocity in the rotating frame, and the constant of integration is labeled as $-\frac{JC}{2}$. This integral of the motion reduces the dimensionality of the

problem by one and provides insight concerning boundaries of motion for a given energy level.

This energy-like quantity is leveraged to determine the minimum Δv that is required to link states with two different energies at a desired location. The minimum Δv occurs when the change in velocity works exclusively towards changing velocity magnitude, and not adjusting direction (i.e., applying maneuver along initial velocity vector). This assumption on the maneuver direction defines that for the minimum case $\Delta v = \mathbf{v}_2 - \mathbf{v}_1$, and

$$\mathbf{v}_1 = \sqrt{2U^* + JC_1}$$

thus,

$$\Delta v_{min} = \sqrt{2U^* + JC_2} - \sqrt{2U^* + JC_1} \quad (2.17)$$

that demonstrates a minimum Δv as not only a function of the difference in JC , but also dependent upon location (through the pseudo-potential function). Of course, this quantity is minimized when the JC s are nearly equal in value, or when U^* approaches infinity. During transfer scenarios where the JC of both the initial and final arcs are fixed, the theoretical minimum Δv offers a point of comparison in support of mission design efforts.

2.1.3 Equilibrium Solutions

Equilibrium solutions offer insight into available motion in the CRTBP. To determine the equilibrium solutions, all time derivatives in the equations of motion are set to zero, by definition. Applying these conditions to the equations of motion reduces them to

$$-x = -\frac{(1-\mu)(x+\mu)}{d^3} - \frac{\mu(x-1+\mu)}{r^3} \quad (2.18)$$

$$-y = \left[-\frac{(1-\mu)}{d^3} - \frac{\mu}{r^3} \right] y \quad (2.19)$$

$$0 = \left[-\frac{(1-\mu)}{d^3} - \frac{\mu}{r^3} \right] z \quad (2.20)$$

Notice that satisfying the last equation, requires that equilibrium solutions lay in the $\hat{x} - \hat{y}$ plane. Additionally, for $y = 0$, the second equation is satisfied; thus, some equilibrium solutions exist on the \hat{x} axis and the focus is initially on this type of solution. Simplifying the remaining equation yields

$$0 = x - \frac{(1 - \mu)(x + \mu)}{(x + \mu)^3} - \frac{\mu(x - 1 + \mu)}{(x - 1 + \mu)^3}$$

$$0 = x - (1 - \mu) \frac{\text{sgn}(x + \mu)}{(x + \mu)^2} - \mu \frac{\text{sgn}(x - 1 + \mu)}{(x - 1 + \mu)^2}$$

Three different cases arise that provide equilibrium solutions depending on the sign of the encapsulated quantities. The solutions then vary depending on the location along the \hat{x} axis: $x < -\mu$ (i.e., further along the negative \hat{x} -axis than P_1), $-\mu < x < 1 - \mu$ (i.e., between P_1 and P_2) and $x > 1 - \mu$ (i.e., further along the positive \hat{x} -axis than P_2). These points are denoted as the collinear points as they all lie on the same line (the \hat{x} -axis). To construct the remaining equilibrium solutions, y is allowed to be nonzero. Removing the $y = 0$ assumption, the following expression must hold to satisfy equation (2.19).

$$\frac{(1 - \mu)}{d^3} + \frac{\mu}{r^3} - 1 = 0 \tag{2.21}$$

Introducing the previous expression into equation (2.18) and rearranging leads to

$$x \left[\frac{(1 - \mu)}{d^3} + \frac{\mu}{r^3} - 1 \right] + \mu \left[\frac{(1 - \mu)}{d^3} + \frac{\mu}{r^3} \right] - \frac{\mu}{r^3} = 0$$

$$x[0] + \mu[1] - \frac{\mu}{r^3} = 0$$

This expression exemplifies that $r^3 = 1$, hence $r = 1$. Introducing $r = 1$ back into equation (2.21) demonstrates that d must also be 1. Recall that r and d are the distances from the primaries, this constraint is represented by a circle of radius 1 emanating from each primary, which leads to the conclusion that two additional equilibrium points arise where these circles intersect.

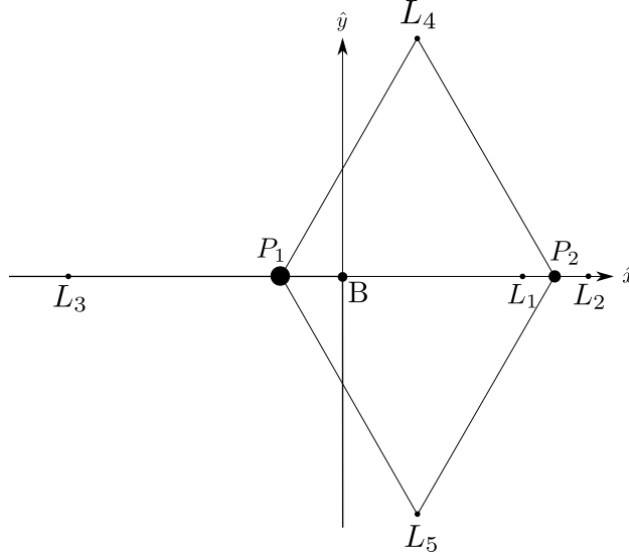


Figure 2.3. Equilibrium Points in the Rotating Frame

Information about dynamical structures in the CRTBP is gained by leveraging the stability characteristics of these equilibrium points, providing insight into motion in their immediate vicinity.

2.1.4 Zero Velocity Surfaces

Though an analytical solution to the equations of motion does not exist for analyzing the behavior, conditions that bound the available regions for P_3 are available. From the JC equation (2.15), notice that for the velocity of P_3 to be real, the quantity $2U^* - JC$ must be greater than zero; Since U^* is solely a function of position, locations where this inequality holds for a given JC (or energy level) are computed. This expression yields the boundary condition $2U^* - JC = 0$, where the velocity is equal to zero and, hence, is denoted Zero Velocity Surface (ZVS). A section of these surfaces intersect the $\hat{x} - \hat{y}$ plane, generating a curve, denoted the Zero Velocity Curve (ZVC). Notice that at the equilibrium points (where $\mathbf{v} = 0$) there is an energy value denoted JC_{L_i} . At this energy level there is an associated ZVC that includes the point L_i .

The available ZVC behaviors are characterized into different categories depending on energy level. These categories, in decreasing JC , are, when JC is greater than JC_{L_1} , when $JC_{L_1} > JC > JC_{L_2}$, when $JC_{L_2} > JC > JC_{L_3}$, when $JC_{L_3} > JC > JC_{L_{4-5}}$ and finally when $JC < JC_{L_{4-5}}$, which is a case where the ZVC no longer exists. Visual representations of these categories are shown below

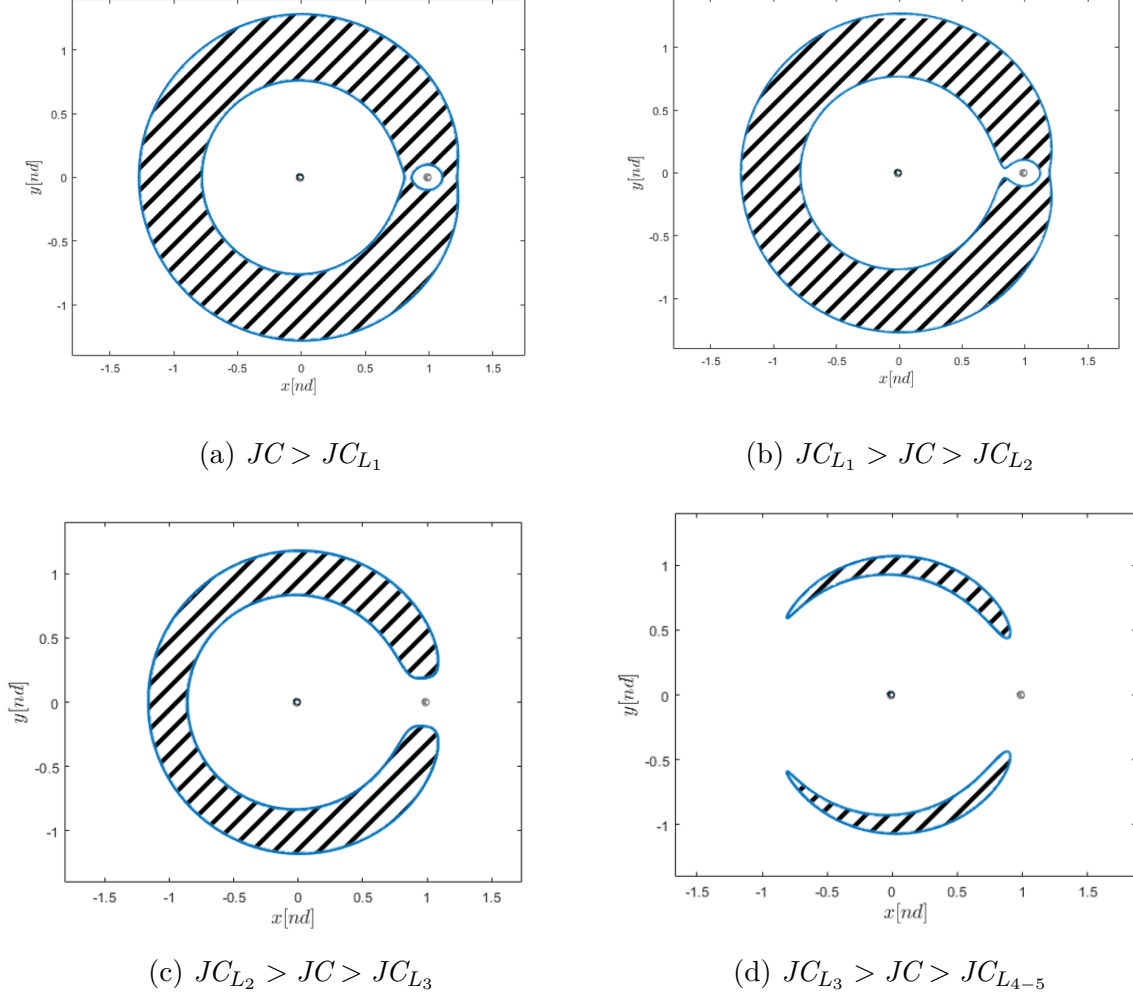


Figure 2.4. ZVCs at a range of energy levels in the Earth-Moon system

Notice that as JC increases, the available transit region shrinks; hence, to transit from P_1 to P_2 near the L_1 vicinity, the JC of a transfer arc must be less than JC_{L_1} . This principle provides a bound for the energy of transfer arcs used for transit into the cislunar vicinity.

3. DYNAMICAL SYSTEMS THEORY

Dynamical systems theory provides a variety of tools to predict motion in non-linear systems (like the CRTBP). Through the use of linear variational equations, motion around equilibrium points is determined. Differential corrections allows for the transition of the linear predictions into desirable motion in the non-linear system. Shooting methods are used in the context of differential corrections to converge on periodic solutions or other transfer solutions of interest, which when combined with continuation methods, can yield families of solutions. Invariant manifold theory allows for the study of natural pathways in and out of periodic solutions. Finally bifurcation theory allows for the discovery of periodic orbit family intersections, which lead to the construction of alternate families. These techniques are leveraged in this investigation as they provide different dynamical structures that are useful for transfer design.

3.1 Linear Variational Equations and Motion Near the Equilibrium Points

The stability information of the equilibrium points offers an understanding of the available motion in their immediate vicinity. To extract the stability information of points in the CRTBP, the linear variational equations are used. The state vector for the CRTBP system is defined to develop the variational equations for the system, as

$$\bar{x} = \begin{bmatrix} x \\ y \\ z \\ \dot{x} \\ \dot{y} \\ \dot{z} \end{bmatrix}$$

The equations of motion (equations (2.8)-(2.10)) are used to define the time derivative function as

$$\bar{f}(\bar{x}) = \dot{\bar{x}} = \begin{bmatrix} \dot{x} \\ \dot{y} \\ \dot{z} \\ 2\dot{y} + U_x^* \\ -2\dot{x} + U_y^* \\ U_z^* \end{bmatrix}$$

With these definitions, the linearization about the equilibrium solutions is, then, conducted. From the state vector of the equilibrium point $L_i(\bar{x}_{L_i})$, the perturbed solution is defined using a small variation (δx) such that

$$\bar{x} = \bar{x}_{L_i} + \delta x$$

Next, the time derivative of the perturbed state is computed

$$\bar{f}(\bar{x}) = \bar{f}(\bar{x}_{L_i} + \delta x) = \dot{\bar{x}}_{L_i} + \delta \dot{x}$$

and, since δx is not an explicit state, but a variation vector, a Taylor Series expansion must be used to represent $\delta \dot{x}$, as

$$\dot{\bar{x}}_{L_i} + \delta \dot{x} \approx \bar{f}(\bar{x}_{L_i}) + \left. \frac{\partial \bar{f}}{\partial \bar{x}} \right|_{\bar{x}_{L_i}} \delta \bar{x} + \dots$$

where all additional terms are higher order terms that are ignored for the purposes of this linear analysis. Additionally, the evaluation of this quantity at the equilibrium point provides $\dot{\bar{x}}_{L_i} = \bar{f}(\bar{x}_{L_i}) = 0$ by definition, so the expression reduces to

$$\delta \dot{x} \approx \left. \frac{\partial \bar{f}}{\partial \bar{x}} \right|_{\bar{x}_{L_i}} \delta \bar{x} \quad (3.1)$$

where $\frac{\partial \bar{f}}{\partial \bar{x}}$ is the Jacobian matrix of the system equations of motion

$$\frac{\partial \bar{f}}{\partial \bar{x}} = A = \begin{bmatrix} \frac{\partial \dot{x}}{\partial x} & \frac{\partial \dot{x}}{\partial y} & \frac{\partial \dot{x}}{\partial z} & \frac{\partial \dot{x}}{\partial \dot{x}} & \frac{\partial \dot{x}}{\partial \dot{y}} & \frac{\partial \dot{x}}{\partial \dot{z}} \\ \frac{\partial \dot{y}}{\partial x} & \frac{\partial \dot{y}}{\partial y} & \frac{\partial \dot{y}}{\partial z} & \frac{\partial \dot{y}}{\partial \dot{x}} & \frac{\partial \dot{y}}{\partial \dot{y}} & \frac{\partial \dot{y}}{\partial \dot{z}} \\ \frac{\partial \dot{z}}{\partial x} & \frac{\partial \dot{z}}{\partial y} & \frac{\partial \dot{z}}{\partial z} & \frac{\partial \dot{z}}{\partial \dot{x}} & \frac{\partial \dot{z}}{\partial \dot{y}} & \frac{\partial \dot{z}}{\partial \dot{z}} \\ \frac{\partial \ddot{x}}{\partial x} & \frac{\partial \ddot{x}}{\partial y} & \frac{\partial \ddot{x}}{\partial z} & \frac{\partial \ddot{x}}{\partial \dot{x}} & \frac{\partial \ddot{x}}{\partial \dot{y}} & \frac{\partial \ddot{x}}{\partial \dot{z}} \\ \frac{\partial \ddot{y}}{\partial x} & \frac{\partial \ddot{y}}{\partial y} & \frac{\partial \ddot{y}}{\partial z} & \frac{\partial \ddot{y}}{\partial \dot{x}} & \frac{\partial \ddot{y}}{\partial \dot{y}} & \frac{\partial \ddot{y}}{\partial \dot{z}} \\ \frac{\partial \ddot{z}}{\partial x} & \frac{\partial \ddot{z}}{\partial y} & \frac{\partial \ddot{z}}{\partial z} & \frac{\partial \ddot{z}}{\partial \dot{x}} & \frac{\partial \ddot{z}}{\partial \dot{y}} & \frac{\partial \ddot{z}}{\partial \dot{z}} \end{bmatrix}$$

Evaluating this matrix in the CRTBP, and, introducing it to equation (3.1) provides

$$\delta \dot{\bar{x}} \approx A \delta \bar{x} = \begin{bmatrix} 0 & 0 & 0 & 1 & 0 & 0 \\ 0 & 0 & 0 & 0 & 1 & 0 \\ 0 & 0 & 0 & 0 & 0 & 1 \\ U_{xx}^* & U_{xy}^* & U_{xz}^* & 0 & 2 & 0 \\ U_{yx}^* & U_{yy}^* & U_{yz}^* & -2 & 0 & 0 \\ U_{zx}^* & U_{zy}^* & U_{zz}^* & 0 & 0 & 0 \end{bmatrix} \begin{bmatrix} \delta x \\ \delta y \\ \delta z \\ \delta \dot{x} \\ \delta \dot{y} \\ \delta \dot{z} \end{bmatrix}$$

where U_{ij}^* represents the partial derivative of U^* with respect to state i and state j ($\frac{\partial^2 U^*}{\partial q_i \partial q_j}$).

Finally, the expression is decomposed into its scalar components to get the variational equations of motion:

$$\partial \ddot{x} - 2\partial \dot{y} = U_{xx}^* \partial x + U_{xy}^* \partial y + U_{xz}^* \partial z$$

$$\partial \ddot{y} + 2\partial \dot{x} = U_{yx}^* \partial x + U_{yy}^* \partial y + U_{yz}^* \partial z$$

$$\partial \ddot{z} = U_{zx}^* \partial x + U_{zy}^* \partial y + U_{zz}^* \partial z$$

These variational equations of motion are used to analyze the stability characteristics of the equilibrium points, revealing information about motion in their proximity. Since the

equilibrium points all lie in the \hat{x} - \hat{y} plane, the variational equations of motion are reduced by evaluating at $z = 0$

$$\partial\ddot{x} - 2\partial\dot{y} = U_{xx}^* \partial x + U_{xy}^* \partial y \quad (3.2)$$

$$\partial\ddot{y} + 2\partial\dot{x} = U_{yx}^* \partial x + U_{yy}^* \partial y \quad (3.3)$$

$$\partial\ddot{z} = U_{zz}^* \partial z \quad (3.4)$$

Notice that equation (3.4) completely governs out of plane motion, as it is decoupled from the rest of the equations of motion. This separation allows for a reduced four-dimensional system when focusing on planar motion

$$\delta\dot{\bar{x}} \approx A\delta\bar{x} = \begin{bmatrix} 0 & 0 & 1 & 0 \\ 0 & 0 & 0 & 1 \\ U_{xx}^* & U_{xy}^* & 0 & 2 \\ U_{yx}^* & U_{yy}^* & -2 & 0 \end{bmatrix} \begin{bmatrix} \partial x \\ \partial y \\ \partial \dot{x} \\ \partial \dot{y} \end{bmatrix}$$

where the eigenvalues of the A matrix provide the stability information of the equilibrium points. These eigenvalues are found through $\det(\lambda I - A) = 0$ and solving for λ (i.e., the roots of the characteristic polynomial)

$$\lambda^4 + (4 - U_{xx}^* - U_{yy}^*)\lambda^2 + U_{xx}^* U_{yy}^* - U_{yx}^* U_{xy}^* = 0 \quad (3.5)$$

Recall that the collinear points lie on the \hat{x} -axis, which allows for the simplification of equation (3.5), such that

$$\lambda^4 + (4 - U_{xx}^* - U_{yy}^*)\lambda^2 + U_{xx}^* U_{yy}^* = 0$$

This expression is represented as a second order polynomial, as

$$\Lambda^2 + 2\beta_1\Lambda - \beta_2^2 = 0$$

where $\Lambda = \lambda^2$, $\beta_1 = 2 - \frac{U_{xx}^* + U_{yy}^*}{2}$ and $\beta_2^2 = -U_{xx}^* U_{yy}^*$. The roots of the binomial evaluate to

$$\Lambda_1 = -\beta_1 + \sqrt{\beta_1^2 + \beta_2^2}$$

$$\Lambda_2 = -\beta_1 - \sqrt{\beta_1^2 + \beta_2^2}$$

thus,

$$\lambda_{1,2} = \pm\sqrt{\Lambda_1}$$

$$\lambda_{3,4} = \pm\sqrt{\Lambda_2}$$

For the collinear points, U_{xx}^* evaluates as > 0 , and, $U_{yy}^* < 0$. This evaluation leads to $\beta_2^2 > 0$ which defines $\Lambda_1 > 0$ and $\Lambda_2 < 0$. It follows, that, λ_1 and λ_2 are real, while λ_3 and λ_4 are imaginary. A solution to the variational equations of motion is defined as a combination of the eigenvalues as exponentials

$$\bar{\xi}(t) = C_1 e^{\lambda_1 t} \vec{v}_1 + C_2 e^{\lambda_2 t} \vec{v}_2 + C_3 e^{\lambda_3 t} \vec{v}_3 + C_4 e^{\lambda_4 t} \vec{v}_4$$

where \vec{v}_i is the corresponding eigenvector to λ_i , and C_i are constants defined based on the initial conditions. Initial conditions that isolate the desired eigenvalue behavior are available. Notice, then, that solutions that exponentially approach or depart from the equilibrium point exist (from λ_1 or λ_2), as well as periodic solutions that oscillate around the equilibrium points (from λ_3 and λ_4). Initial conditions that lead to periodic motion in the Earth-Moon CRTBP are computed and propagated in the linearized system as

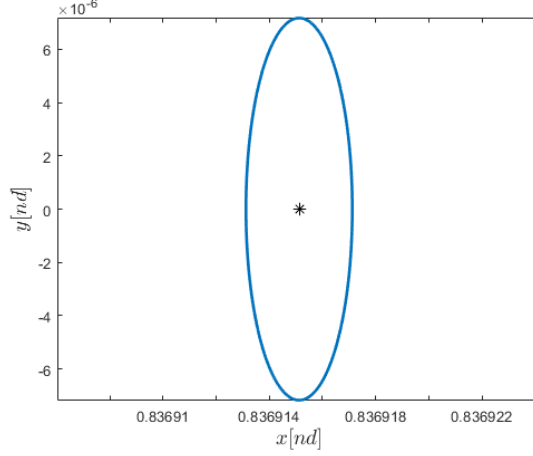


Figure 3.1. Linear oscillatory behavior in L_1 vicinity of Earth-Moon CRTBP

These linearized solutions provide insight into the available motion in the full non-linear system.

3.2 State Transition Matrix

A more general relationship relating an initial variation from a reference solution $\delta\bar{x}(t_0)$, to a final variation after propagation $\delta\bar{x}(t_f)$, provides additional insight into motion in the model. This more general solution is written in the form

$$\delta\bar{x}(t_f) = \Phi(t_f, t_0)\delta\bar{x}(t_0) \quad (3.6)$$

where t_0 and t_f are some initial and final times, and $\Phi(t_0, t_f)$ is

$$\Phi(t_f, t_0) = \begin{bmatrix} \frac{\partial x_f}{\partial x_0} & \frac{\partial x_f}{\partial y_0} & \frac{\partial x_f}{\partial z_0} & \frac{\partial x_f}{\partial \dot{x}_0} & \frac{\partial x_f}{\partial \dot{y}_0} & \frac{\partial x_f}{\partial \dot{z}_0} \\ \frac{\partial y_f}{\partial x_0} & \frac{\partial y_f}{\partial y_0} & \frac{\partial y_f}{\partial z_0} & \frac{\partial y_f}{\partial \dot{x}_0} & \frac{\partial y_f}{\partial \dot{y}_0} & \frac{\partial y_f}{\partial \dot{z}_0} \\ \frac{\partial z_f}{\partial x_0} & \frac{\partial z_f}{\partial y_0} & \frac{\partial z_f}{\partial z_0} & \frac{\partial z_f}{\partial \dot{x}_0} & \frac{\partial z_f}{\partial \dot{y}_0} & \frac{\partial z_f}{\partial \dot{z}_0} \\ \frac{\partial \dot{x}_f}{\partial x_0} & \frac{\partial \dot{x}_f}{\partial y_0} & \frac{\partial \dot{x}_f}{\partial z_0} & \frac{\partial \dot{x}_f}{\partial \dot{x}_0} & \frac{\partial \dot{x}_f}{\partial \dot{y}_0} & \frac{\partial \dot{x}_f}{\partial \dot{z}_0} \\ \frac{\partial \dot{y}_f}{\partial x_0} & \frac{\partial \dot{y}_f}{\partial y_0} & \frac{\partial \dot{y}_f}{\partial z_0} & \frac{\partial \dot{y}_f}{\partial \dot{x}_0} & \frac{\partial \dot{y}_f}{\partial \dot{y}_0} & \frac{\partial \dot{y}_f}{\partial \dot{z}_0} \\ \frac{\partial \dot{z}_f}{\partial x_0} & \frac{\partial \dot{z}_f}{\partial y_0} & \frac{\partial \dot{z}_f}{\partial z_0} & \frac{\partial \dot{z}_f}{\partial \dot{x}_0} & \frac{\partial \dot{z}_f}{\partial \dot{y}_0} & \frac{\partial \dot{z}_f}{\partial \dot{z}_0} \end{bmatrix}$$

This 6 x 6 matrix, where the rows represent the partial derivative of the variation on a final state with respect to the variation of each initial state, is known as the state transition matrix (STM)[20]. The STM possesses some useful properties. Consider separating equation (3.6) into 2 segments, stopping at some intermediate time t_1 , such that

$$\delta\bar{x}(t_1) = \Phi(t_1, t_0)\delta\bar{x}(t_0)$$

$$\delta\bar{x}(t_f) = \Phi(t_f, t_1)\delta\bar{x}(t_1)$$

These equations are combined as

$$\delta\bar{x}(t_f) = \Phi(t_f, t_1)\delta\bar{x}(t_1) = \Phi(t_f, t_1)\Phi(t_1, t_0)\delta\bar{x}(t_0)$$

From this combination, the first useful property of the STM is deduced, $\Phi(t_f, t_0) = \Phi(t_f, t_1)\Phi(t_1, t_0)$.

This property is leveraged when segments are propagated separately, and the total STM, from t_0 to t_f , is desired. Additionally, equation (3.6) is rearranged as

$$\Phi^{-1}(t_f, t_0)\delta\bar{x}(t_f) = \delta\bar{x}(t_0)$$

and, from the same definition in equation (3.6)

$$\delta\bar{x}(t_0) = \Phi(t_0, t_f)\delta\bar{x}(t_f)$$

Hence, another property of the STM is $\Phi(t_f, t_0) = \Phi^{-1}(t_0, t_f)$. Finally

$$\delta\bar{x}(t_0) = \Phi(t_0, t_0)\delta\bar{x}(t_0)$$

So $\Phi(t_0, t_0)$ must be the identity matrix. The properties described above, are leveraged to facilitate the construction of the STM in this model.

To obtain the STM of a desired segment, numerical integration is done alongside the states of said segment. The differential equation for the STM is found by taking the time derivative of equation (3.6) evaluated at some time t as

$$\delta \dot{\bar{x}}(t) = \dot{\Phi}(t, t_0) \delta \bar{x}(t_0)$$

Recall that $\delta \dot{\bar{x}}(t) = A(t) \delta \bar{x}(t)$, such that

$$A(t) \delta \bar{x}(t) = \dot{\Phi}(t, t_0) \delta \bar{x}(t_0)$$

introducing the expression from equation (3.6) provides

$$A(t) \Phi(t, t_0) \delta \bar{x}(t_0) = \dot{\Phi}(t, t_0) \delta \bar{x}(t_0)$$

which provides the differential equation for the STM, as

$$\dot{\Phi}(t, t_0) = A(t) \Phi(t, t_0)$$

Since the CRTBP model does not possess an analytical solution to its equations of motion, these linear predictions of motion provided by the STM, are essential for analyzing the motion.

3.3 Differential Corrections

Generating desired solutions in the non-linear CRTBP is complex, so a numerical corrections scheme is implemented. Insights gained from the linear approximations of the CRTBP model are leveraged to compute the desired solutions. A multi-dimensional Newton-Raphson algorithm is employed to converge on solutions that meet specific constraints. A Newton-

Raphson scheme allows for root-finding of some continuous function $\bar{F}(\bar{X})$ [21]. This method works by defining a vector of design variables

$$\bar{X} = \begin{bmatrix} X_1 \\ X_2 \\ \vdots \\ X_n \end{bmatrix}$$

and a vector of desired constraint equations

$$\bar{F}(\bar{X}) = \begin{bmatrix} F_1(\bar{X}) \\ F_2(\bar{X}) \\ \vdots \\ F_m(\bar{X}) \end{bmatrix}$$

Since the Newton-Raphson method is a root finding scheme, constraints are formulated such that all $F_i(\bar{X}_f) = 0$ when fulfilled, where \bar{X}_f is the set of design variables that satisfies the constraints. Achieving perfect convergence (i.e., $|\bar{F}(\bar{X}_f)| = 0$) using numerical methods is infeasible, thus, convergence is defined when the norm of the constraint vector is less than a chosen tolerance $|\bar{F}(\bar{X}_f)| < tol$. To compute \bar{X}_f , the set of design variables that satisfies the constraints, an expression that relates it to the initial design variable vector \bar{X}_0 and the initial constraint vector $\bar{F}(\bar{X}_0)$ is desired. A first order Taylor Series expansion of $\bar{F}(\bar{X}_f)$ about \bar{X}_0 yields

$$\bar{F}(\bar{X}_f) \approx \bar{F}(\bar{X}_0) + DF(\bar{X}_0)[\bar{X}_f - \bar{X}_0] \approx \bar{0} \quad (3.7)$$

where DF is the $n \times m$ matrix representing the partial derivative of the constraint vector with respect to the design variable vector as

$$DF(\bar{X}) = \frac{\partial \bar{F}(\bar{X})}{\partial \bar{X}} = \begin{bmatrix} \frac{\partial F_1(\bar{X})}{\partial X_1} & \frac{\partial F_1(\bar{X})}{\partial X_2} & \cdots & \frac{\partial F_1(\bar{X})}{\partial X_n} \\ \frac{\partial F_2(\bar{X})}{\partial X_1} & \frac{\partial F_2(\bar{X})}{\partial X_2} & \cdots & \frac{\partial F_2(\bar{X})}{\partial X_n} \\ \vdots & \vdots & \ddots & \vdots \\ \frac{\partial F_m(\bar{X})}{\partial X_1} & \frac{\partial F_m(\bar{X})}{\partial X_2} & \cdots & \frac{\partial F_m(\bar{X})}{\partial X_n} \end{bmatrix}$$

The expression in equation (3.7) is rearranged to solve for the final set of desired design variables, such that

$$\bar{X}_f = \bar{X}_0 - DF(\bar{X}_0)^{-1} \bar{F}(\bar{X}_0)$$

However, since this provides a linear approximation to a non-linear system, the predicted \bar{X}_f will likely not satisfy the constraint vector to the desired tolerance in a single evaluation. Hence, the process is iterated as

$$\bar{X}_{i+1} = \bar{X}_i - DF(\bar{X}_i)^{-1} \bar{F}(\bar{X}_i)$$

Until the actual \bar{X}_f that will satisfy the constraints to the desired tolerance is found. Notice that if $m < n$ (i.e., there are more free variables than constraints) the system is under-constrained and an infinite number of solutions are available[22]. Additionally, in the case of an under-constrained system, the DF matrix is not invertible. To analyze this kind of system, a minimum-norm solution is implemented, as it returns the nearest solution to the initial guess. This formulation provides

$$\bar{X}_{i+1} = \bar{X}_i - (DF(\bar{X}_i)DF(\bar{X}_i)^T)^{-1} \bar{F}(\bar{X}_i)$$

where $DF(\bar{X}_i)^T$ represents the transpose of the matrix $DF(\bar{X}_i)$. These methods are leveraged to locate desired periodic orbits as well as transfer solutions in the non-linear CRTBP.

3.3.1 Single Shooter Application to Periodic Orbits in CRTBP

Periodic motion is shown to exist in the vicinity of the equilibrium points when considering a linear approximation. These approximations are used as an initial guess in the full non-linear model. Symmetry in the CRTBP is also exploited to compute periodic orbits in the vicinity of the equilibrium points. This symmetry provides that, when starting from a perpendicular crossing of the $\hat{x} - \hat{z}$ plane, periodic motion can be guaranteed by constraining a following crossing to also be perpendicular[23]. Propagating a perpendicular crossing of the linearized system, as an initial condition, for half a period, does not lead to a perpendicular crossing in the non-linear CRTBP equations of motion. Given that this condition is not met, differential corrections are required to achieve the desired result. In the general case there are 4 free variables (x_0, z_0, \dot{y}_0 and T , the time of flight) and 3 constraints (y_f, \dot{x}_f and \dot{z}_f), making the system under-constrained, meaning there are infinitely many solutions. The design variable and constraint vectors are defined as

$$\bar{X} = \begin{bmatrix} x_0 \\ z_0 \\ \dot{y}_0 \\ T \end{bmatrix}, \bar{F} = \begin{bmatrix} y_f \\ \dot{x}_f \\ \dot{z}_f \end{bmatrix} \quad (3.8)$$

such that

$$DF(\bar{X}) = \begin{bmatrix} \frac{\partial y_f}{\partial x_0} & \frac{\partial y_f}{\partial z_0} & \frac{\partial y_f}{\partial \dot{y}_0} & \frac{\partial y_f}{\partial T} \\ \frac{\partial \dot{x}_f}{\partial x_0} & \frac{\partial \dot{x}_f}{\partial z_0} & \frac{\partial \dot{x}_f}{\partial \dot{y}_0} & \frac{\partial \dot{x}_f}{\partial T} \\ \frac{\partial \dot{z}_f}{\partial x_0} & \frac{\partial \dot{z}_f}{\partial z_0} & \frac{\partial \dot{z}_f}{\partial \dot{y}_0} & \frac{\partial \dot{z}_f}{\partial T} \end{bmatrix} = \begin{bmatrix} \Phi_{21} & \Phi_{23} & \Phi_{25} & \dot{y}_f \\ \Phi_{41} & \Phi_{43} & \Phi_{45} & \ddot{x}_f \\ \Phi_{61} & \Phi_{63} & \Phi_{65} & \ddot{z}_f \end{bmatrix}$$

where Φ_{ij} represents the term on row i and column j of the STM from t_0 to T . Alternatively, if one of the design variables is fixed to a desired value, the DF matrix becomes invertible and a single solution is available. An L_1 Lyapunov in the Earth-Moon CRTBP is computed using the aforementioned process

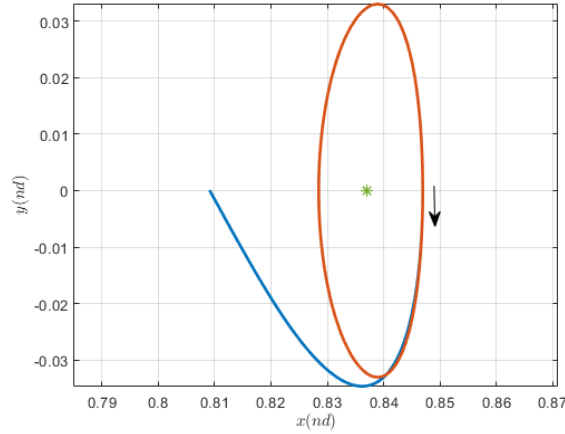


Figure 3.2. Initial guess (blue) and corrected (red) L_1 Lyapunov orbit in Earth-Moon system

where the blue arc represents the initial guess from the linearized system, propagated until the next \hat{x} -axis crossing, in the CRTBP non-linear model, and the red arc is the corrected orbit. Periodic orbits are of interest as they provide repeatable motion where a spacecraft can loiter and complete their mission.

3.4 Continuation Methods

It is possible for solutions to come in sets of families[24], hence, a continuation scheme that provides adequate initial guesses, and allows for the exploration of structures near a converged solution, is necessary. Families of periodic orbits and transfer solutions are studied in this investigation.

3.4.1 Natural Parameter Continuation

A simple continuation scheme, natural parameter continuation, allows for the exploration of solutions while following a natural parameter of the system, such as, position, velocity, time of flight or JC . This method provides an initial guess in the vicinity of a previously converged solution, by using the design variables of the previous solution. This parameter, along which the continuation takes place, remains fixed for the corrections process. Fixing the continuation parameter is achieved by either, explicitly constraining it to the desired

value, or, by excluding it from the design variables. The initial guess is then corrected at the new location, in order to generate an additional solution. This process is repeated until the desired amount of solutions is found, or the end of the family is reached [24].

3.4.2 Natural Parameter Continuation Application to Periodic Orbits in CRTBP

Natural parameter continuation is applied to periodic orbits in the CRTBP to compute families that are leveraged for transfer design. To implement this method, a parameter is fixed for the corrections process. For this example, x is fixed by removing it from the design variable vector shown in equation (3.8), providing a square system. Given that x is fixed, a natural parameter continuation scheme along this variable is used. Define the design vector of a previously converged solution as \bar{X}_{k-1} , with an initial set of conditions $\bar{x}_{k-1} = [x_0 \ 0 \ z_0 \ 0 \ \dot{y}_0 \ 0]^T$ and time of flight T_0 . The continued solution is then computed at location $x_0 + s_{cont}$, where s_{cont} is the continuation step, with initial guess $\bar{x}_k = [x_0 + s_{cont} \ 0 \ z_0 \ 0 \ \dot{y}_0 \ 0]^T$ and time of flight T_0 . This approach provides the initial design vector $\bar{X}_{k,0} = [z_0 \ \dot{y}_0 \ T_0]^T$. Notice this design vector matches that of the previous solution as

$$\bar{X}_{k,0} = \bar{X}_{k-1}$$

Alternatively, once more than one solution has been computed, a linear prediction of the next solution is available to be used for the initial guess

$$\bar{X}_{k,0} = \bar{X}_{k-1} + s_{cont,k} \frac{\bar{X}_{k-1} - \bar{X}_{k-2}}{s_{cont,k-1}}$$

where $s_{cont,k}$ is the continuation step used to go from solution $k - 1$ to solution k . An application of this method on an L_1 Lyapunov orbit in the CRTBP provides the L_1 Lyapunov family of periodic orbits. This process is then repeated for L_2 and L_3 to compute the respective families.

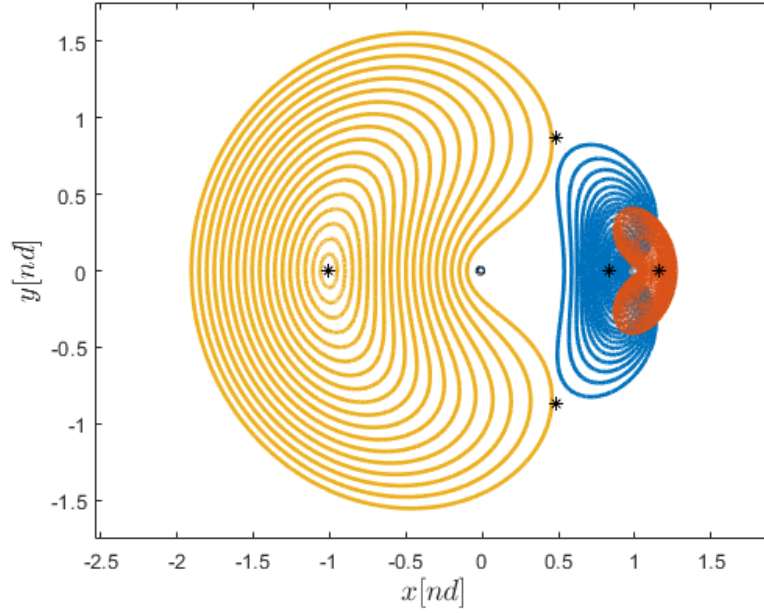


Figure 3.3. Lyapunov orbit families in the Earth-Moon system

Note that these are not the entirety of the Lyapunov families, simply a representative set of the orbits that encompass them. The computation of families expands the available trade space of solutions that can be targeted for mission design.

3.5 Stability of Periodic Orbits

An analysis of the stability of periodic orbits in the CRTBP provides information about structures in their vicinity, such as pathways in and out of the orbit, or other periodic orbits. To analyze the stability characteristics of a periodic orbit in the CRTBP, the orbit is discretized into returns to a stroboscopic map. Doing this provides that the linear stability of the orbit is given by the STM after one period of the orbit, denoted the Monodromy matrix (M). The eigenspace of the Monodromy matrix then provides the desired stability information. In contrast to the stability analysis of the equilibrium points, the Monodromy matrix maps the variation of a discrete time system. Recall that

$$\delta\bar{x}(T_P) = \Phi(T_P + t_0, t_0)\delta\bar{x}(t_0) = M\delta\bar{x}(t_0)$$

where T_P is the orbital period. Notice, that, $\delta\bar{x}(T_P)$ represents the variation from the reference state on the map. Consider the case after N returns to the map, when the initial variation occurs along an eigenvector

$$\delta\bar{x}(NT_P) = M^N \vec{v}_i$$

where \vec{v}_i is an eigenvector of M . Using the eigenvalue equation $M\vec{v}_i = \lambda_i \vec{v}_i$, this expression becomes

$$\delta\bar{x}(NT_P) = \lambda_i^N \vec{v}_i \quad (3.9)$$

Hence, the eigenvalues represent the rate of departure from a reference point on the map, which, in this case, is the fixed point representing the periodic orbit. From equation (3.9), notice that when $|\lambda| > 1$ a variation along the corresponding eigenvector leads to motion departing the periodic orbit, when $|\lambda| < 1$ a variation along the corresponding eigenvector leads to motion approaching the periodic orbit, and when $|\lambda| = 1$ a variation along the corresponding eigenvector leads to motion that maintains a constant distance away from the orbit. These eigenvectors are leveraged to compute motion near a periodic orbit that follows the desired characteristics.

3.5.1 Invariant Manifold Theory

The eigenspace of the Monodromy matrix provides key information about motion into and out of a periodic orbit. Given that a certain periodic orbit has an eigenvalue $|\lambda| > 1$, a variation along the corresponding eigenvector leads to departing behavior. This variation is applied along all the states on a periodic orbit, and propagating the perturbed solutions forward in time generates a surface of solutions. This surface is dubbed the unstable manifold. Similarly, a stable manifold exists when $|\lambda| < 1$ and is computed by propagating the corresponding perturbed states in backwards time. The eigenvalues of the Monodromy matrix in the CRTBP come in reciprocal pairs [25], hence, if a periodic orbit possesses an unstable manifold, it also possesses a stable manifold. The stable and unstable manifolds of a sample L_1 Lyapunov orbit in the Earth-Moon system are shown

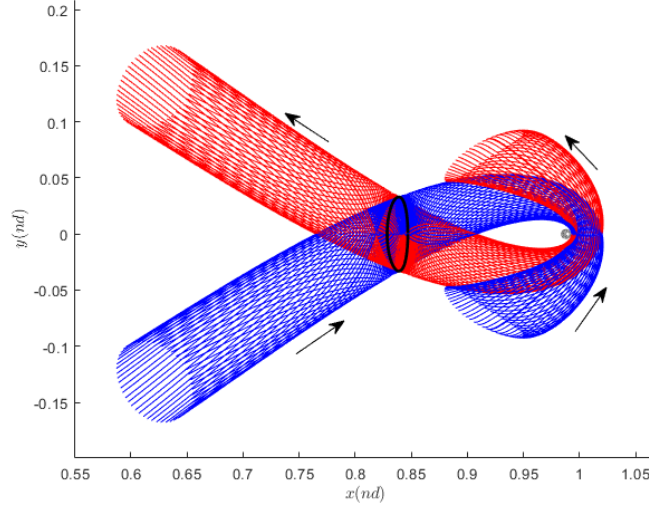


Figure 3.4. L_1 Lyapunov orbit invariant manifolds in the Earth-Moon system

Stable manifold arcs are leveraged for transfer design in this investigation, since they provide natural pathways that approach orbits ballistically.

3.5.2 Bifurcation Theory

Bifurcation theory allows for the discovery of periodic orbit families, through the evaluation of the eigenvalue evolution of periodic orbits. A bifurcation occurs when the order of stability of a fixed point changes. Recall that the stability of periodic orbits in the CRTBP is analyzed through the use of a stroboscopic map, such that the periodic orbit becomes a fixed point on said map. Notice from equation (3.9), if an eigenvalue of the Monodromy matrix is equal to one, then the perturbed solution will remain fixed relative to the reference solution on the map. The corresponding eigenvector then must point in the direction of a periodic orbit. Eigenvalues of the Monodromy matrix in the CRTBP come in reciprocal pairs, and there is always a pair that is equal to one [25]. This trivial pair of eigenvalues correspond to, a mode that follows the periodic orbit in question, and a mode that follows the periodic

orbit family that encompasses it. A change in order of stability then occurs when one of the non-trivial pairs of eigenvalues along the family does one of three things:

- **Tangent Bifurcation:** A tangent bifurcation occurs when the family crosses over $\lambda = 1$. An additional pair of eigenvalues equal to one suggests additional periodic modes, meaning, new variation directions which point to a periodic solution on the map exist. It is important to note that not every tangent bifurcation leads to a new family of solutions [26]. If a tangent bifurcation occurs at a JC extremum of the family, it is denoted a cyclic fold, and does not result in a new family of solutions.
- **Period Doubling Bifurcation:** A bifurcation for which the period of the underlying orbit is doubled occurs when $\lambda = -1$. Notice that after an initial variation of the state along the corresponding eigenvector, the first return to the map will not match the varied state in this case

$$\delta\bar{x}(1T_p) = \lambda^1 \vec{v}_i = -1\vec{v}_i$$

However, the second return matches the initial variation

$$\delta\bar{x}(2T_p) = \lambda^2 \vec{v}_i = \vec{v}_i$$

This means that a periodic orbit exists along this variation direction, though it has a period that is twice the period of the bifurcating orbit.

- **Secondary Hopf Bifurcation:** This kind of bifurcation occurs when the eigenvalues along a family collide on the unit circle and depart it, at a location other than $\lambda = \pm 1$. This type of bifurcation is less typical in the CRTBP than the other bifurcations described.

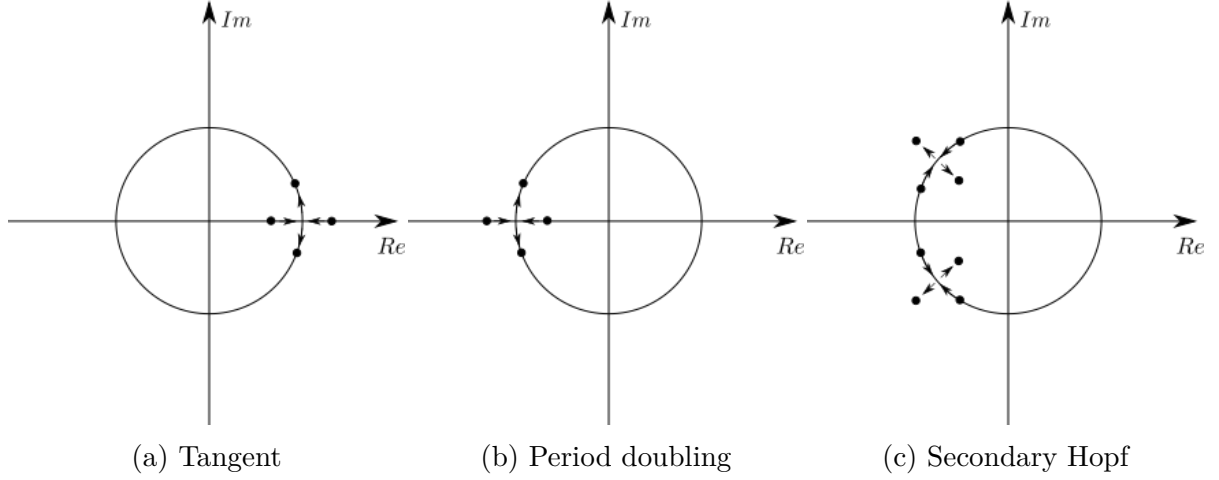


Figure 3.5. Eigenvalue behavior for different types of bifurcations, visualized on unit circle

Analyzing the eigenvalues of the orbits in the L_1 Lyapunov family leads to the discovery of a tangent bifurcation in close vicinity to L_1 . The initial state of the bifurcating orbit is perturbed by the eigenvector of the second pair of unity eigenvalue. This perturbed state is then used as an initial guess for the corrections process. This application leads to the generation of a spatial Halo orbit. Using a continuation scheme the Halo family is computed from this first generated orbit. A set of orbits from the L_1 and L_2 Halo families is shown

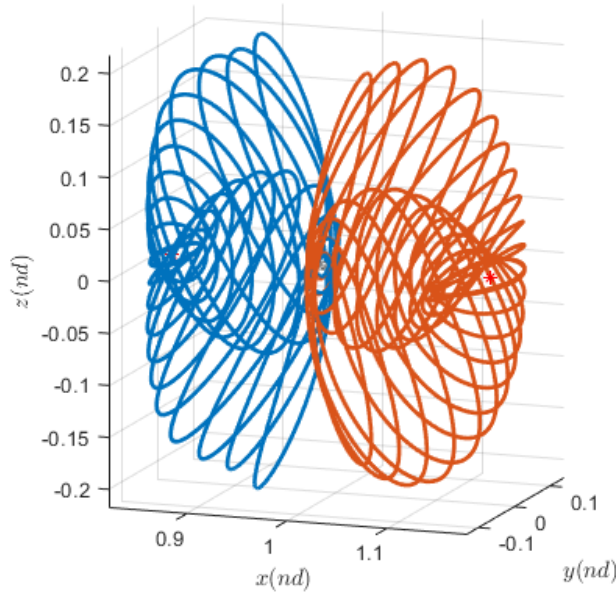


Figure 3.6. L_1 and L_2 Halo orbit family in Earth-Moon system

Note, that, this kind of family also exists around L_3 . These Halo orbit families possess spatial target orbits, which provide alternate lunar coverage options, that may be desirable for mission design.

Other Period Multiplying Bifurcations

Period multiplying bifurcations exist at locations where the order of stability of the underlying orbit does not change. Recall the analysis of a period doubling bifurcation. A similar analysis can be conducted for an arbitrary period NT_p . An N-period bifurcation then occurs when an initial variation off of a periodic orbit returns to itself after N returns to the stroboscopic map. Hence, for an N-period bifurcation to exist, we must have

$$\delta\bar{x}(NT_p) = \lambda^N \vec{v}_i = \vec{v}_i$$

Notice, that, in order for this expression to hold, λ must be an Nth root of unity, such that $\lambda^N = 1$. For example, consider a 3-period bifurcation. For this bifurcation to exist, the eigenvalues of the bifurcating orbit must be the third root of unity, which corresponds with

an angle in the unit circle of $\frac{2\pi}{3}$ and $\frac{4\pi}{3}$. An angle of 0 corresponds to $\lambda = 1$ and is technically a root of unity, and, since a variation along this eigenvector is fixed after 1 revolution, it is clear that it must then also remain fixed for 3 revolutions. However, since this location corresponds to a tangent bifurcation, it is excluded from consideration for an N-period bifurcation location, as it simply represents the same underlying orbits, propagated for N revolutions of their orbital period. For $\frac{2\pi}{3}$ and $\frac{4\pi}{3}$ the variation will not repeat onto itself after the first return, but it will after the third return to the map, leading to an orbital period of 3 times that of the initial orbit.

Analyzing the eigenvalues of the L_2 Halo family shows that it possesses several opportunities for N-period bifurcations, as it possesses eigenvalues that evolve along the unit circle. These bifurcations include one 3-period bifurcation, three 4-period bifurcations and six 5-period bifurcations. Following the notation introduced by Zimovan-Spreen [7], a set of 5-period families are generated

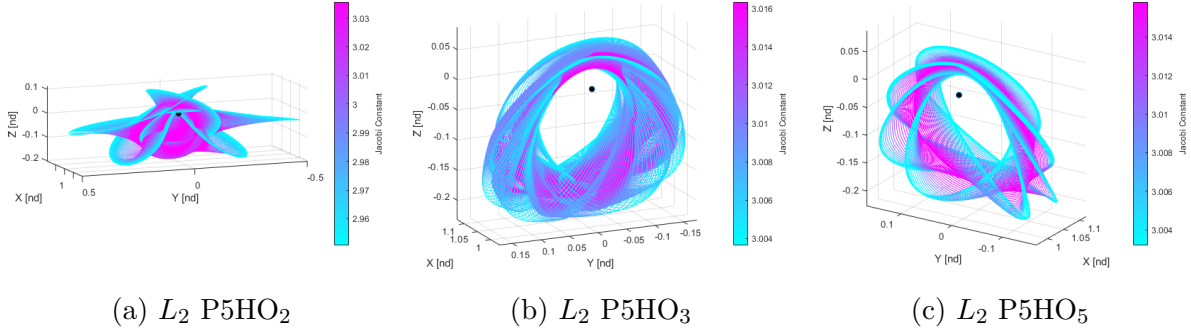


Figure 3.7. L_2 Halo 5-period orbit bifurcating families

where the black marker represents the lunar position. The discovery of new periodic orbit families provides an increased amount of natural structures that can be leveraged during mission transfer design.

3.6 Other topics to consider

May also write about multiple shooter and pseudo arclength if I have time at the end, but it's not necessary.

4. TRANSFERS TO THE EARTH-MOON L_1 VICINITY

The purpose of this investigation is to study the characteristics of two-maneuver transfers, from a 500 km altitude, circular Low Earth Orbit(LEO) to the Earth-Moon L_1 vicinity. As a baseline, a 59,000 km \hat{y} amplitude L_1 Lyapunov orbit, similar to that of the ARTEMIS mission[27], is considered. Transfers with direct insertion into a target orbit are analysed first, before expanding the trade space to leverage stable manifold arcs for orbital insertion. Tangent insertion transfers are studied first, as they represent the ideal maneuver direction and simplify the available transfer space. This transfer space is subsequently expanded, by studying transfers that leverage non-tangent insertions. Finally, transfer solutions are extended past the baseline case, through different orbits of the L_1 Lyapunov family. This extended transfer space provides opportunities that can be leveraged in support of mission design.

4.1 Transfers with Direct Insertion into Baseline Orbit

One of the simplest kind of transfers from LEO to an orbit in the L_1 vicinity, is a two-maneuver direct insertion transfer. The two maneuvers represent: a Trans-Lunar Injection maneuver (TLI) to depart LEO, and an insertion maneuver to enter the final orbit. Only TLIs that are applied along the velocity direction are considered for departure, to make efficient use of the typically large maneuvers[28][29]. Additionally, the study focuses on short time of flight (TOF) transfers that remain internal to the Earth-Moon system. Focusing on tangent insertion transfers allows for the reduction of the transfer space, as a first step to evaluate possible transfer solutions to the L_1 vicinity. A tangential insertion is defined as an insertion where the incoming velocity of the departure arc is parallel to the velocity of the target insertion state. From this definition, there are two possible scenarios for a tangential insertion, one where the incoming and target velocity are in the same direction and one where they are in opposite directions, as

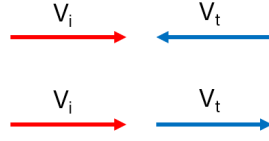


Figure 4.1. Tangent insertion options

where V_i is the incoming velocity on the transfer arc and V_t is the velocity of the target state. A tangential insertion where the incoming velocity and the target velocity point in the same direction, represents the theoretical minimum ΔV required to bridge the energy gap between the transfer arc JC and the target orbit JC . To construct such transfers, the fact that L_1 Lyapunovs have perpendicular crossings of the $\hat{x} - \hat{z}$ plane is leveraged. Starting at a perpendicular crossing on an orbit, vary \dot{y} and propagate in negative time until the transfer arc reaches perigee. These sets of arcs are evaluated to find which arc provides a similar perigee altitude to that of the desired LEO (500 km in this case). This solution is used as the initial guess for a corrections process, where \dot{y} and TOF are design variables used to target a final state perigee with a 500 km altitude. This process is continued to other orbits in the family, by varying the perpendicular crossing location. A set of transfers to the L_1 Lyapunov family leveraging the perpendicular crossing nearest to the Moon, are shown

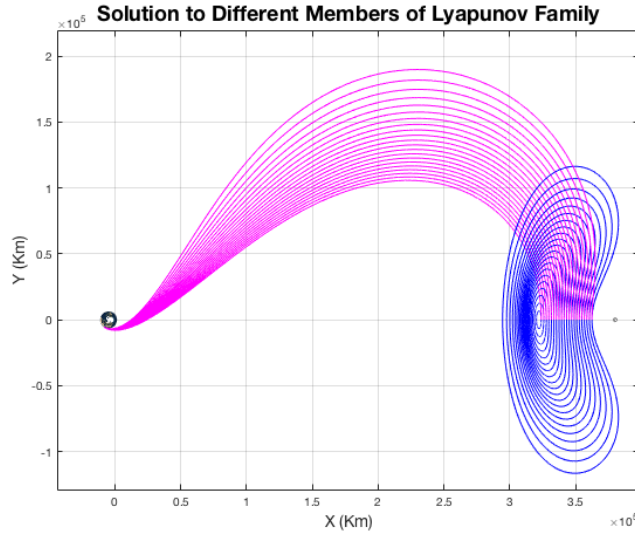


Figure 4.2. Transfers to L_1 Lyapunov orbits perpendicular crossings

Alternatively, instead of continuing along the family, a continuation scheme is applied to compute other transfer solutions along a given orbit. Since these other locations are no longer perpendicular crossings, both \dot{x} and \dot{y} at the insertion location are allowed to vary, while simultaneously constraining them to be tangent to the orbital velocity at that location. The application of this method on a sample L_1 Lyapunov is shown

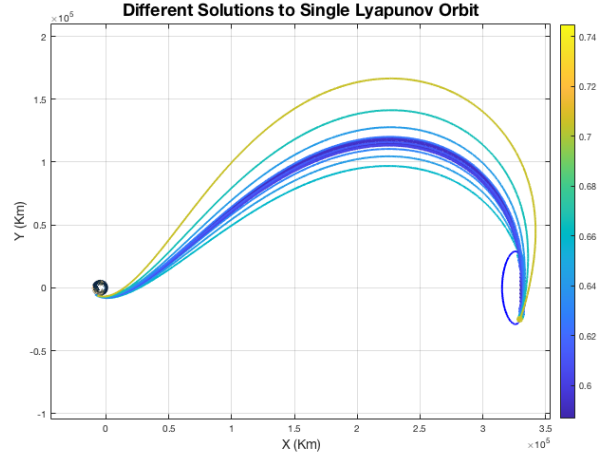


Figure 4.3. Tangent transfers to baseline orbit

where the color of the transfer arc represents the insertion ΔV in km/s. Define the departure angle (θ), as the angle between the Earth-Moon line and the line connecting the Earth to the point where the TLI is applied

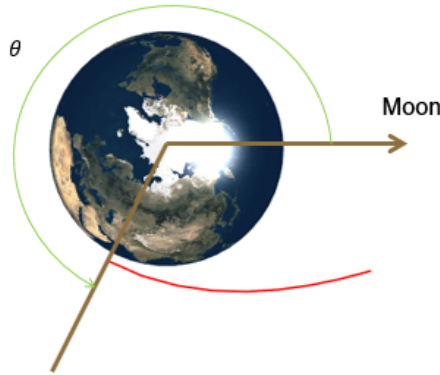


Figure 4.4. Departure angle definition

where the red line represents a departure arc (or transfer arc) after the TLI has been applied. This definition allows for the analysis of the departure characteristics of the family of solutions shown in Figure 4.3. Given that the transfer family maintains similar geometry for its entirety, it is expected that the departure characteristics are bounded within a small region of values, as shown in Figure 4.5. Note, that, the TLIs displayed fall near the lower limit of the TLIs used during the Apollo program[29], as they provide transfer arcs that don't reach the Moon. Additionally, notice that the solutions with the lowest insertion maneuver cost occurs a few hours past the Earth-Moon line along the orbit.

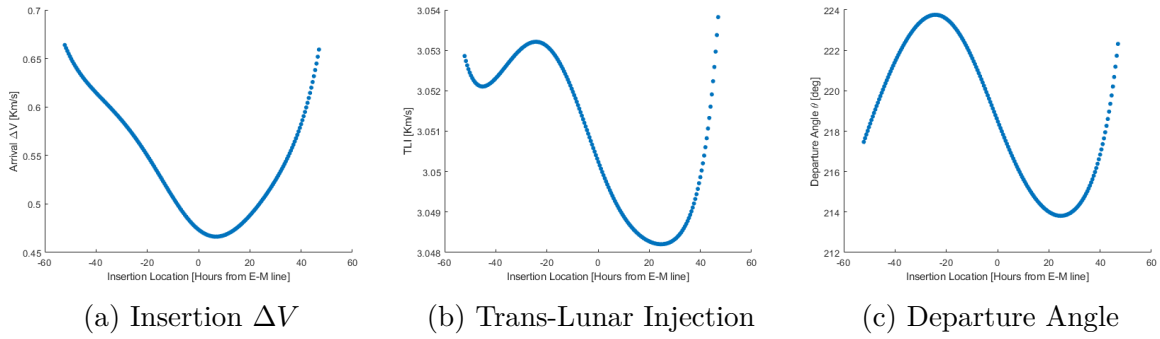


Figure 4.5. Tangent transfer characteristics to baseline orbit

As the continuation process approaches the region near the maximum \hat{y} amplitude of the orbit, the corrections algorithm has higher difficulty converging. This is explained by points near this location having an orbital velocity that points towards or away from the barycenter of the system, denoted as Zero Momentum Points (ZMP)[30]. These points denote the boundaries for the region where the continuation scheme for tangential transfers is successful. When the target velocity points away from the barycenter of the system, the corrector tends towards a solution with an infinitely large TLI, such that the transfer arc resembles a straight line. Alternatively, when the target velocity points towards the barycenter, the corrector tends towards a solutions that has an apogee past the Moon, before returning to the target location. This continuation barricade necessitates that solutions on one side of the ZMP are continued independently from solutions on the other side of it. Thus, the process is repeated from the alternate perpendicular crossing on the orbit (where the orbital velocity points along positive \hat{y} direction) and continued towards the ZMPs to generate a picture

of available direct transfers to the desired orbit. While tangent direct insertion provides relatively simple transfers, it is limited in breadth, resulting in a small solution space.

4.2 Transfers Leveraging Stable Manifolds of Baseline Orbit

Stable manifolds provide natural pathways into periodic orbits that expand available transfer options. L_1 Lyapunov orbits possess eigenvalues such that $|\lambda| > 1$, meaning they also possess stable and unstable manifolds. The stable manifold is of interest, as the focus of the investigation is to enter orbits in the L_1 vicinity. Stable manifolds arrive at the orbit from two different directions; for L_1 Lyapunov orbits one half-manifold arrives from the direction of the Earth (denoted left half-manifold) and the other arrives from the direction of the moon (denoted right half-manifold).

4.2.1 Tangent Vs Non-Tangent Insertion Transfers

Leveraging manifold arcs provides additional insertion locations that are leveraged for transfer design. The left half-manifold provides arcs with ample transfer insertion opportunities, which arrive onto the orbit from the Earth side of the orbit.

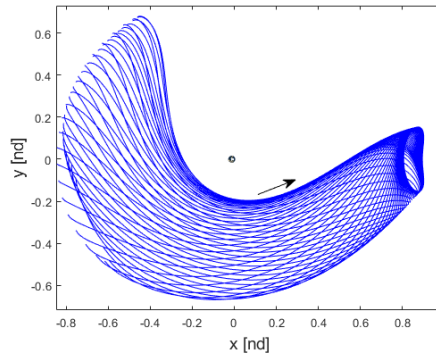


Figure 4.6. Left half-manifold arcs of baseline orbit

The right half-manifold is more complex, as it is comprised of arcs that arrive from the lunar side of the orbit. Propagating the stable right half-manifold in backwards time provides mostly arcs that approach the orbit from outside of the system, as they enter through the L_2 gateway. However, a portion of this half-manifold includes arcs that incorporate a lunar flyby

as they approach from the Earth vicinity. This excursion near the Earth vicinity provides similar insertion locations as the left half-manifold.

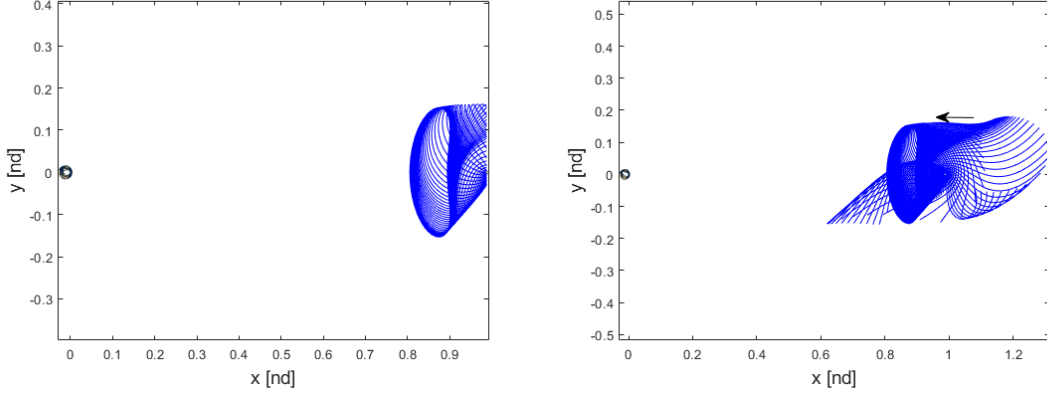


Figure 4.7. Stable right half-manifold arcs of baseline orbit

To characterize the effect of different insertion locations, consider a single manifold arc within the manifold tube. Since tangential transfers cover a narrower solution space, they are evaluated first. Transfers are generated by selecting a point on the manifold arc, and using differential corrections to target a perigee with 500 km altitude in backwards time, where the velocity magnitude at the insertion point and TOF are allowed to vary. Starting on a manifold state near the target orbit, an initial guess is generated by using a nearby direct insertion transfer solution. Once the converged transfer for the first state on the manifold arc is computed, it is leveraged in a continuation scheme that progresses to other insertion locations along the stable manifold arc, as it gets further away from the orbit. Given that the maneuver is constrained to be tangential, this continuation process struggles with convergence as it approaches the ZMPs on the stable manifold, as discussed with direct insertion transfers. Nonetheless, independently computing transfers to the different insertion locations is an option. By manually varying the velocity magnitude and propagating in backwards time, a feasible initial guess is procured at each desired insertion location. Following this methodology, a trade space of solutions is generated for a large portion of the manifold arc. A set of the available geometries is displayed

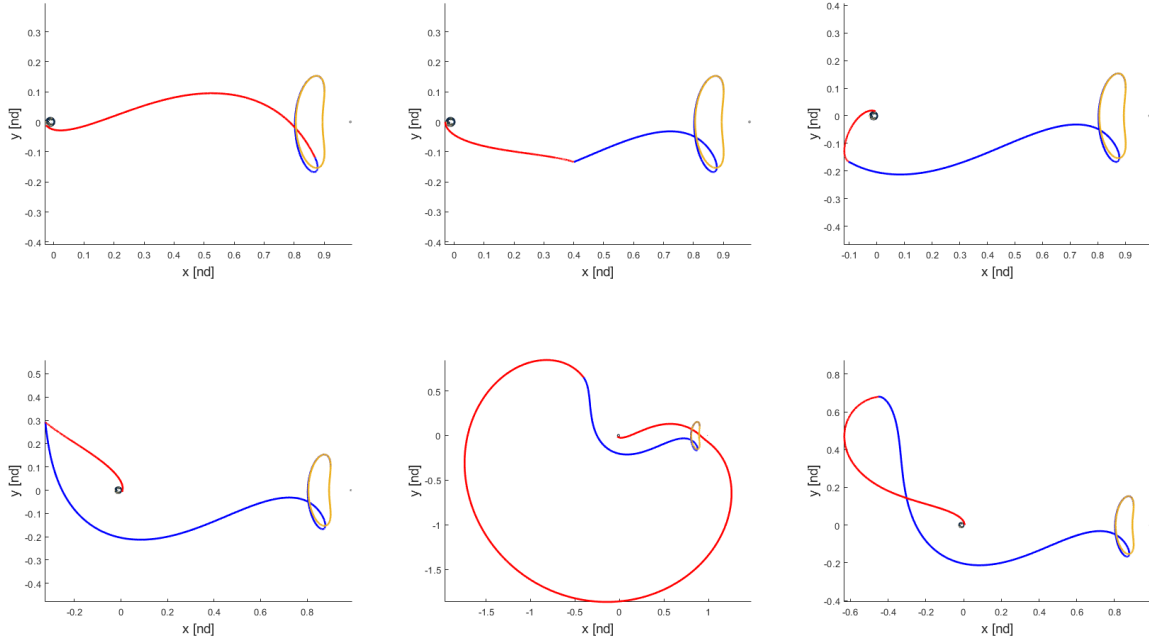


Figure 4.8. Tangential transfers to stable left half-manifold arc of baseline orbit

where the coasting arc between the TLI and the insertion maneuver, or transfer arc, is shown in red, the stable manifold arc is shown in blue and the target orbit is shown in yellow. Similarly, a single manifold arc is chosen on the right half-manifold. An arc that traverses from the Earth vicinity towards the orbit, and leverages a lunar fly-by before approaching the orbit from the right side is selected. Computing transfers in the same manner as for the left half-manifold arc, produces the geometries shown

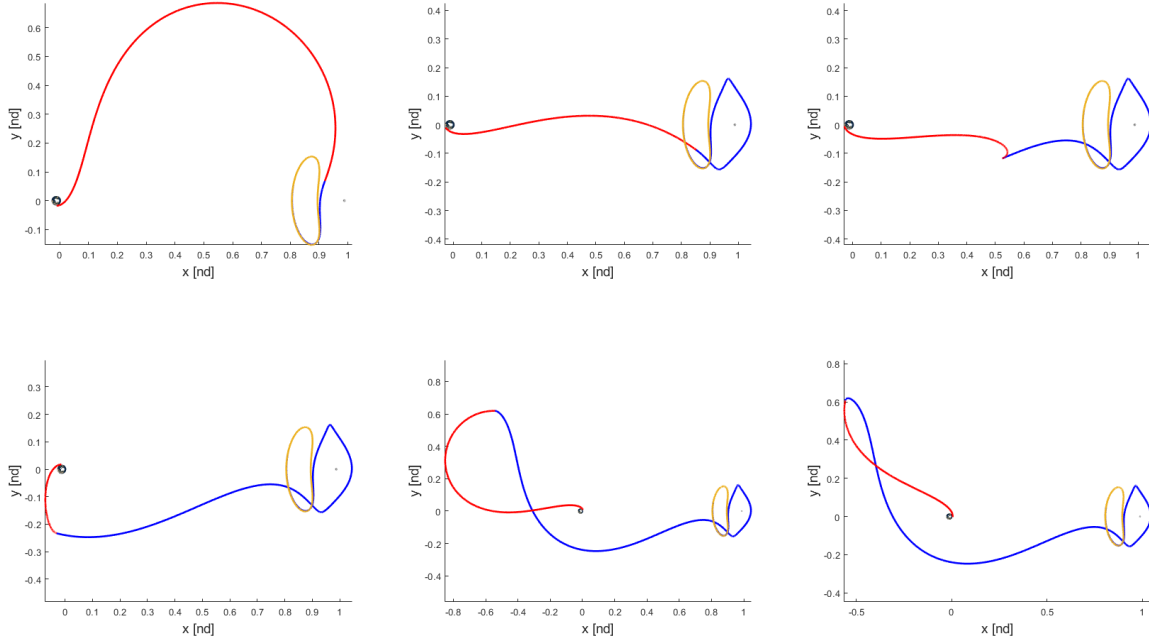


Figure 4.9. Tangential transfers to stable right half-manifold arc of baseline orbit

While this stable manifold arc provides a distinctly different lunar fly-by, notice the similarity in the available transfer geometries. Additionally, notice the large variety of transfer arc size, required to maintain the tangential insertion constraint for both manifold arcs considered. This large variety is achieved through the variation of TLI magnitude, which leads to a large transfer arc energy range over the solution space. While tangent insertion provides the theoretical minimum ΔV to bridge the energy gap between two states at a given location, the departure energy is largely variable for the computed tangent insertion transfers. Removing the tangentiality constraint provides additional flexibility, allowing for transfer options that possess a smaller energy gap at the insertion point. For this reason, transfers that are not constrained to possess tangential insertion are considered next, and are denoted non-tangent transfers. If no additional constraints are included, the corrections scheme for a non-tangent transfer represents an under-constrained system. To compare the performance of the two insertion methods, non-tangent insertion transfers are converged by using the same initial guess provided to the tangential insertion transfers. Since a minimum norm formulation is used for the convergence of the under-constrained system, it is expected that the converged

solution will remain near the initial guess. Insertion locations along the manifold arc are defined as the time away from manifold insertion into the target orbit, meaning, if insertion is conducted at -5 days, the spacecraft will coast on the stable manifold arc for 5 days before it naturally arrives at the target orbit. A visual representation of the insertion location on each of the manifold arcs to be analyzed is provided.

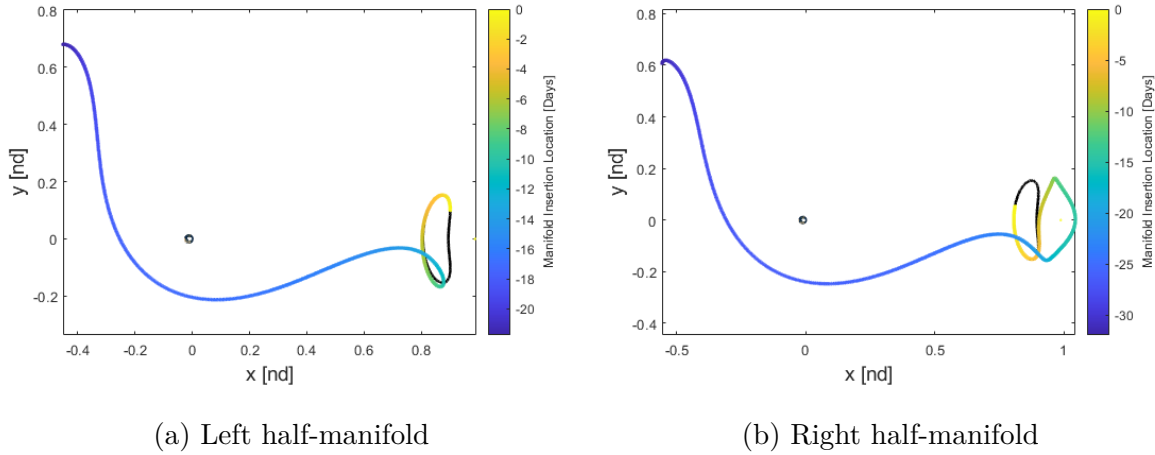


Figure 4.10. Insertion location along manifold arc

Once transfers using both methodologies are generated, their characteristics are compared. First, focus on the insertion maneuver angle, which is defined as the angle from the target velocity at the insertion point V_t to the incoming velocity on the transfer arc V_i .

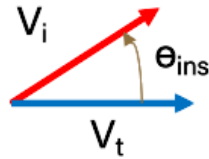


Figure 4.11. Insertion angle definition

Evaluating this quantity for the computed tangent and non-tangent insertion transfers provides

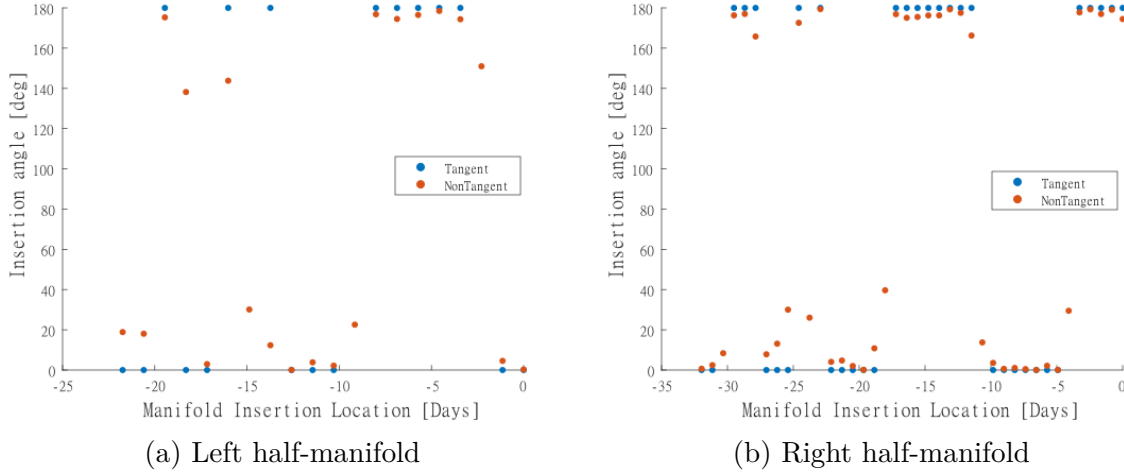


Figure 4.12. Insertion ΔV comparison

Notice that the tangent transfers have either $\theta_{ins} = 0 \text{ deg}$ or $\theta_{ins} = 180 \text{ deg}$, as expected from the definition in Figure 4.1. Additionally, notice that the non-tangent transfers do not deviate from their tangent counterparts significantly at most insertion locations, as the initial guess provided was tangent, and a minimum norm approach was implemented in corrections. Next, focus on the insertion maneuver magnitude

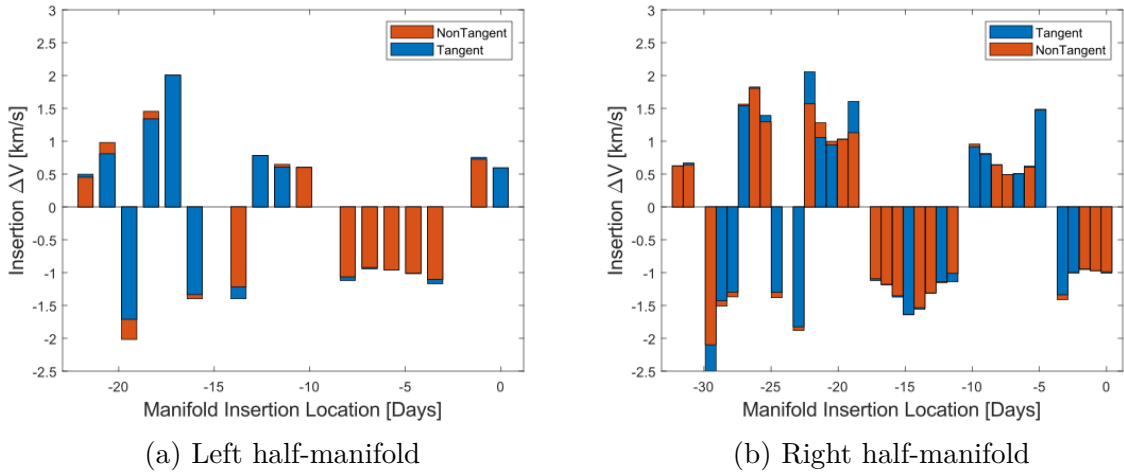


Figure 4.13. Insertion ΔV comparison

where the transfers denoted with a positive ΔV refer to the tangent type where the velocities are in the same direction and a negative ΔV refers to the tangent type where the velocities

are in opposite directions, as defined in Figure 4.1. Notice that the insertion locations that provide the lowest insertion ΔV s appear near the target orbit and near the first apogee after flying past the Earth, while the insertion locations near perigee display comparatively large insertion maneuvers for both kinds of transfers. Additionally, notice that both the left and right half-manifold arcs analyzed display the trend described. Given that a tangential maneuver, when the velocities are in the same direction, provides the theoretical minimum ΔV to bridge the energy gap at the maneuver location, one might expect for the non-tangential transfer to require a larger maneuver. However, since the transfer arc is not fixed to a given energy, it is possible for the non-tangent transfer to bear a smaller energy gap, between transfer and target arc, than the tangent transfer. This variation in energy gap can reduce maneuver size as displayed at various insertion locations in Figure 4.13. This variation is exemplified by evaluating the transfer arc JC characteristics for the computed transfers

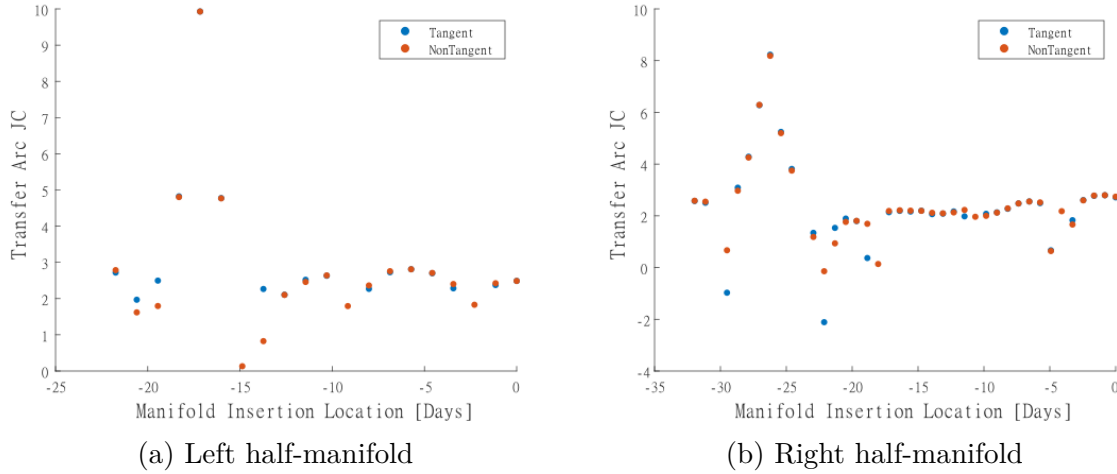


Figure 4.14. Transfer arc JC comparison

Notice again that, the characteristics remain similar between both types of transfers at most locations. However, at some insertion locations, a noticeable difference in transfer arc JC is apparent. These insertion locations correspond to the locations that display the largest insertion ΔV difference, between tangential and non-tangential transfers, in Figure 4.13. Recall that JC is a function of both position (through U^*) and velocity, hence, the transfer

arc JC is a function of the departure location along the 500 km LEO orbit as well as the initial velocity of the transfer arc, which is comprised of the circular velocity of the orbit in addition to the TLI applied. To understand how each of these conditions affect the JC , consider a sample departure trade. This trade is constructed by applying a TLI of 3 km/s at all departure angles θ on a 500 km LEO. The transfer arc JC at each location is then evaluated

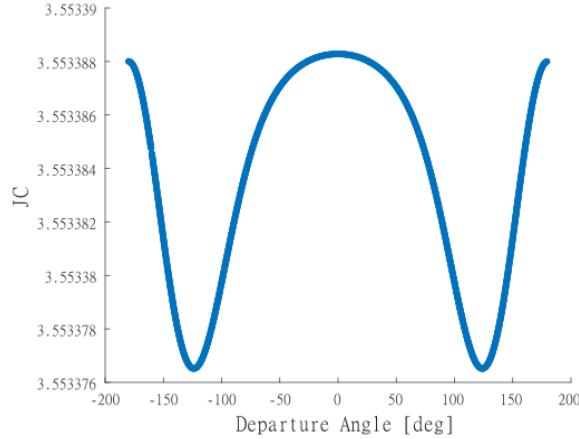


Figure 4.15. JC variation along 500 km LEO with 3 km/s TLI

Notice that JC varies very slightly with respect to departure location θ for a given TLI. Recall that JC varies with the magnitude of the non-dimensional velocity squared (equation (2.15)), and U^* is purely a function of position. For the range of TLIs witnessed in the solution space, the non-dimensional velocity magnitude is on the order of ten, hence, a small variation in TLI has a much larger effect on JC than the observed effect from varying departure angle. This is corroborated by the TLIs of the converged transfers

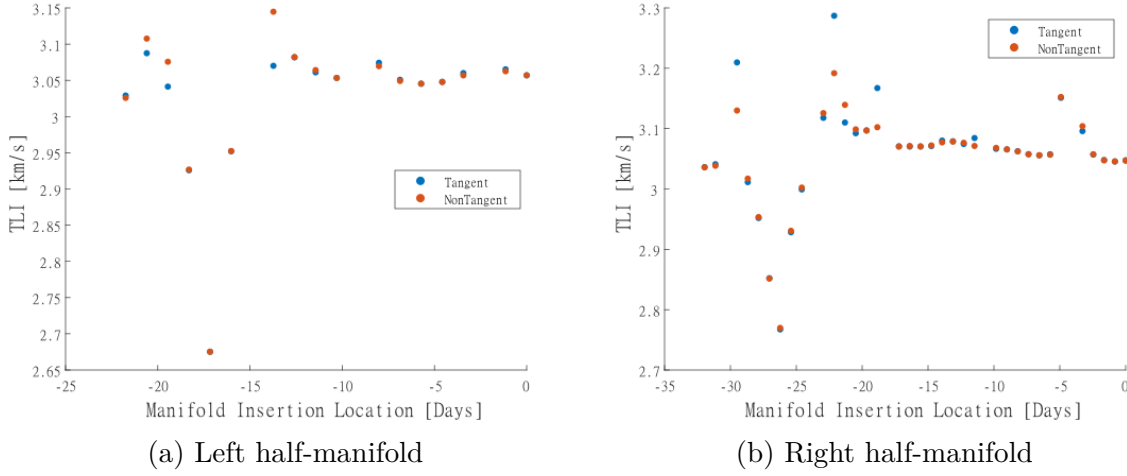


Figure 4.16. Transfer arc TLI comparison

Notice that the trend matches that of Figure 4.14 almost exactly, except for it being mirrored vertically, given that a smaller velocity corresponds to a larger JC . Recall that the theoretical minimum ΔV to overcome a given energy gap is a function of maneuver location and it is minimized when U^* is maximized, as seen in equation (2.17). Notice from the definition of U^* (equation (2.11)), that U^* is maximized when the distance to the primaries is minimized or when the quantity $x^2 + y^2$ is maximized. Hence, performing a maneuver in close proximity to the Earth presents a low transfer cost opportunity. However, the computed transfers show the opposite trend, displaying large insertion maneuvers for insertion locations near perigee. The explanation for this phenomenon is rather simple. Notice that the TLI of the transfers that use an insertion location near perigee is much lower than the TLI at other locations, as a factor of attempting a tangential insertion much closer to the original orbit. This smaller TLI leads to the energy gap to overcome at the insertion location being larger than the energy gap at the other locations analyzed. Essentially, the transfers that insert into the manifold near perigee partially delay the energy change, from LEO to the insertion location, leading to a higher insertion cost. Finally, analyse the range of departure angles available for the transfers computed

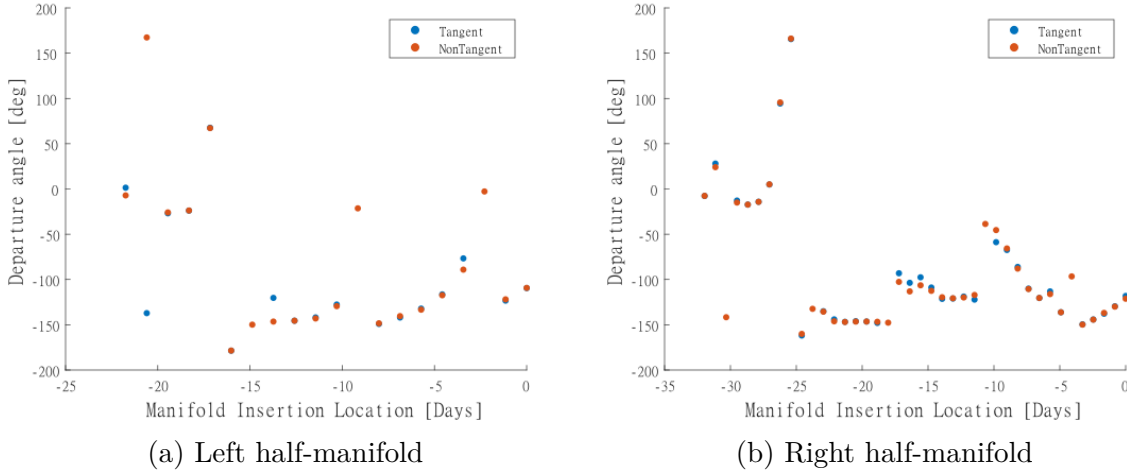
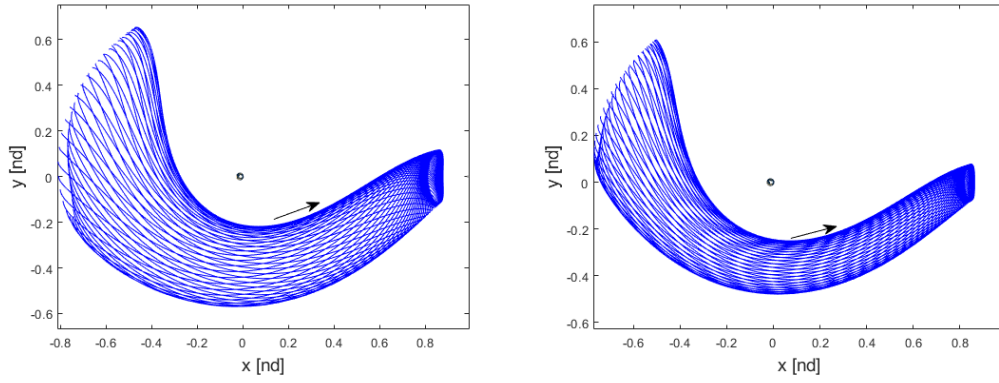


Figure 4.17. Departure angle (θ) comparison

The wide variety of departure angle options from both types of transfers is notable, given that direct insertion transfers provide a very limited range of options. Finally, note that the transfers that leverage the right half-manifold showcase similar cost and behavior as those that leverage the left half-manifold. Overall, transfers that leverage the stable manifolds provide transfer opportunities that cover a wider range of departure conditions, allowing for flexibility in mission transfer design.

4.2.2 Expanding Beyond Baseline Orbit

To verify that characteristics evaluated for the baseline orbit actually represent the characteristics of the general space, additional orbits in the L_1 vicinity are analyzed. Focus on two L_1 Lyapunov orbits, with 45,000 km and 30,000 km \hat{y} amplitudes. Consider first the left half-manifolds of these orbits. Notice that these half-manifolds are similar in geometry to the ones of the baseline orbit.

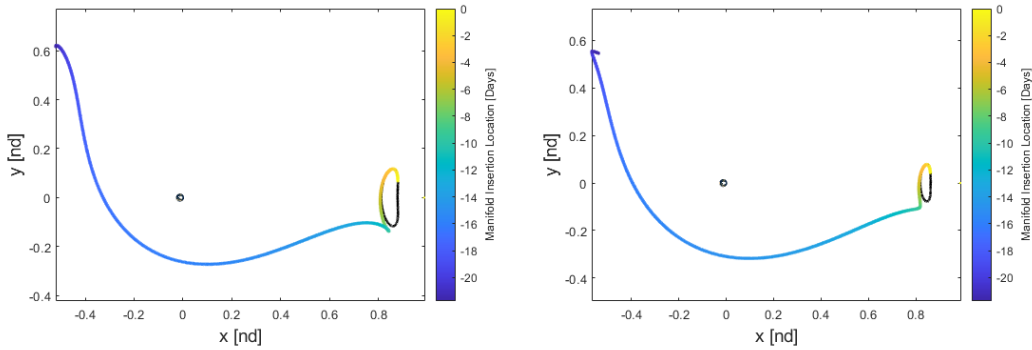


(a) 45,000 km \hat{y} amplitude

(b) 30,000 km \hat{y} amplitude

Figure 4.18. Left half-manifold of L_1 Lyapunov orbits

Individual manifold arcs that closely resemble the geometry shown in Figure 4.10 are selected for each orbit. Defining the insertion location as before, the selected arcs are shown

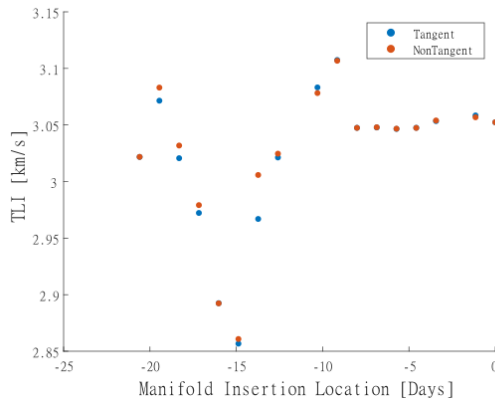
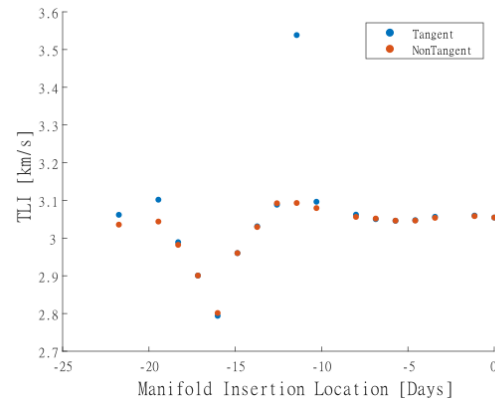
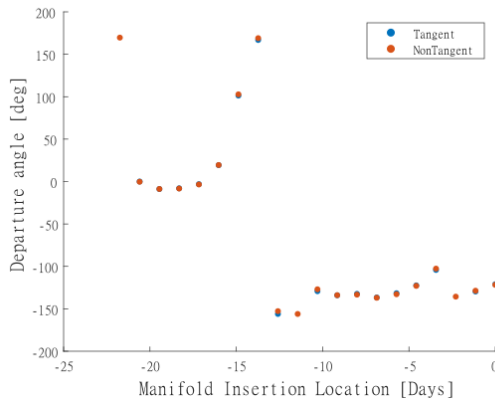
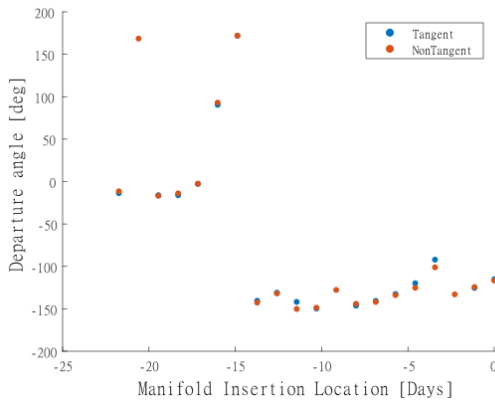
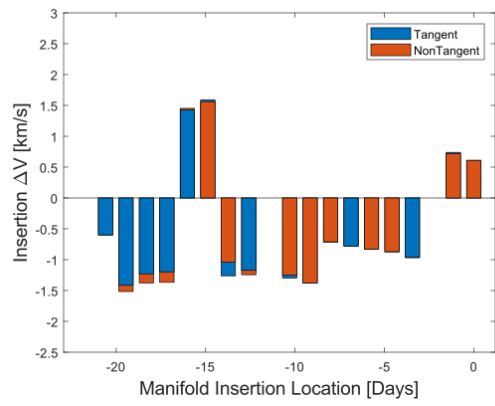
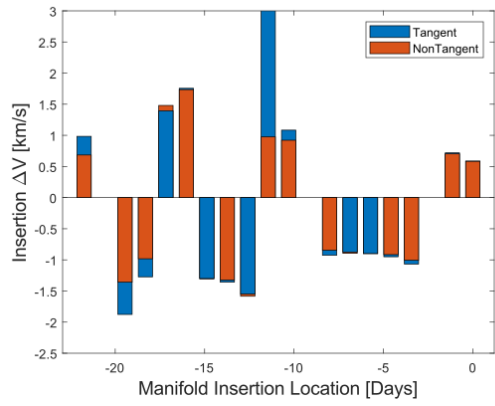


(a) 45,000 km \hat{y} amplitude

(b) 30,000 km \hat{y} amplitude

Figure 4.19. Selected left half-manifold arcs

Again, initial guesses for tangent maneuver solutions are generated independently for different insertion locations along the selected manifold arcs, and, these initial guesses are used to converge both the tangent transfer and the non-tangent transfer at each location. Similar trajectory geometries arise as those seen in Figure 4.8, which is expected, given the similarity in manifold arc geometry.

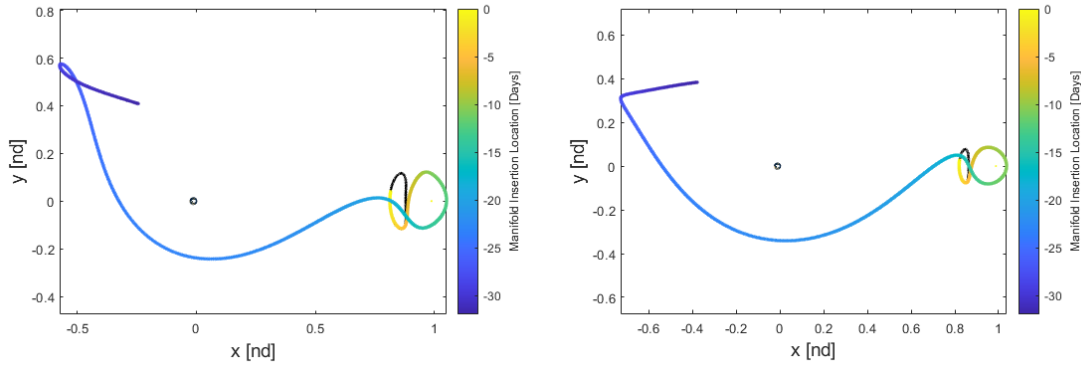


(a) 45,000 km \hat{y} amplitude

(b) 30,000 km \hat{y} amplitude

Figure 4.20. Transfer characteristics for left half-manifold arcs of alternate L_1 Lyapunov orbits

Characteristics of the computed transfers are shown in Figure 4.20. Notice again that non-tangent transfers provide lower maneuver cost solutions at several insertion locations as they provide more flexibility in transfer arc JC , through the variation of TLI. Additionally, transfers that possess insertion locations near the manifold arcs perigee display higher maneuver costs, as the TLI decreases, in order to accommodate for a tangential arrival in the initial guess at these locations. Notice as well that a large range of departure options are available and they vary based on insertion location along the manifold arcs. The similarity of these results to the characteristics of the baseline orbit suggest that continuation of transfers between orbits of the same family is possible, which allows for the construction of a more complete trade space of available solutions towards the L_1 vicinity. This process is then repeated on the same orbits, but with right half-manifold arcs. These orbits possess stable manifold arcs that approach from the Earth after a lunar fly-by as used on the baseline orbit. Right half-manifold arcs that display similar geometry to the one in Figure 4.10 are chosen

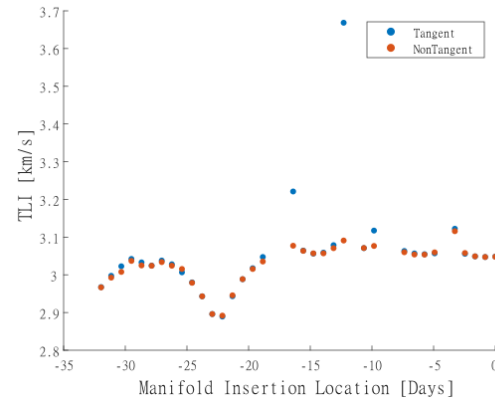
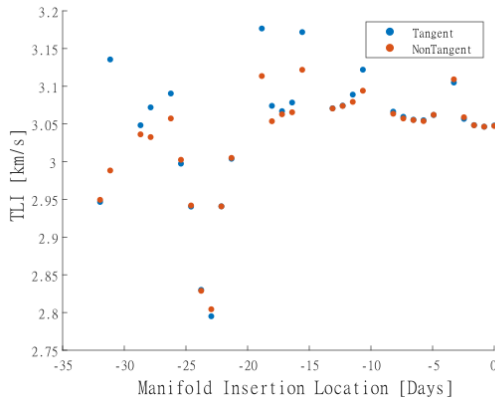
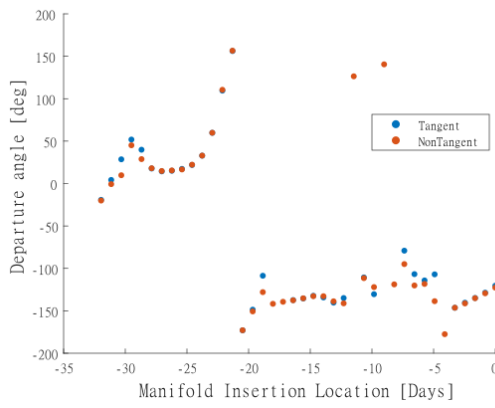
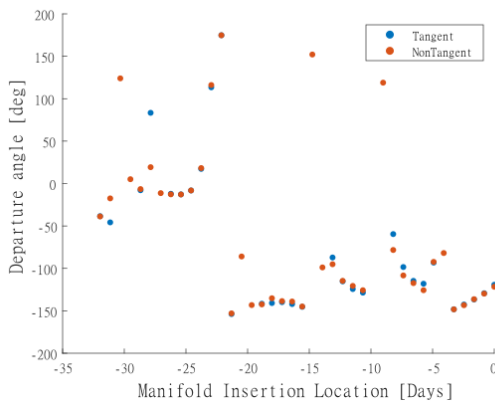
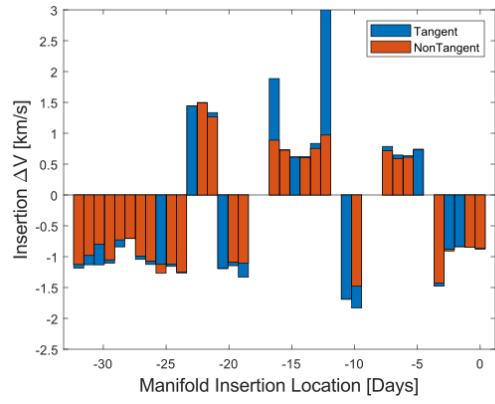
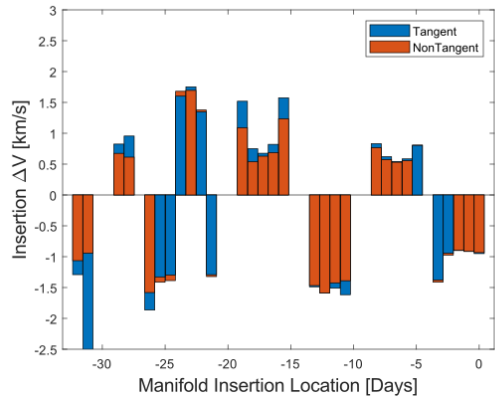


(a) 45,000 km \hat{y} amplitude

(b) 30,000 km \hat{y} amplitude

Figure 4.21. Selected left half-manifold arcs

Tangent and non-tangent transfers are generated following the methodology previously described, and their characteristics are compared in Figure 4.22.



(a) 45,000 km \hat{y} amplitude

(b) 30,000 km \hat{y} amplitude

Figure 4.22. Transfer characteristics for right half-manifold arcs of alternate L_1 Lyapunov orbits

Notice that the characteristics witnessed in the previously compared manifold arcs are repeated here. Mainly, non-tangent transfers provide the targeter more flexibility (uncovering lower cost transfers), lower insertion ΔV solutions are found near the target orbit and near the first apogee after Earth fly-by, a broad range of departure angles are available, and the lower TLI solutions near perigee lead to larger insertion costs. The similarity in solution characteristics across different sized orbits in the L_1 Lyapunov family, once again suggests that continuation, from one orbit to another in the same family, is a viable way to generate a larger trade space of transfer solutions. Notice from all the right half-manifold arcs evaluated, that including a lunar fly-by in the transfer solution does not provide lower insertion cost solutions. In the two-body problem, executing a fly-by of a secondary celestial body provides an effectively free ΔV relative to the primary celestial body, dubbed a gravity assist. However, in the CRTBP, simply flying near a primary does not change the energy of the trajectory, as the gravitational influence of the primary is already included in the model. Recall from the minimum theoretical ΔV equation (equation (2.17)) that the best locations to perform a maneuver are in close proximity to a primary. Hence, right half-manifold arcs that possess low-altitude lunar fly-bys can be leveraged through an insertion maneuver in the near vicinity of the Moon, however, simply transiting near the vicinity of the moon does not affect the energy of the trajectory. From this phenomenon, and the similarity in transfer characteristics discussed, it is noted that right half-manifold arcs add complexity and risk by performing a lunar fly-by, and do not improve transfer cost. As a result, the investigation will focus on transfers to the left half-manifold moving forward.

4.3 Expanding Transfer Trade Space on Regions of Interest

From the characteristics displayed in the analysis comparing tangent and non-tangent insertion transfers, two Regions of Interest (ROI) are introduced; a region near the target orbit, and a region near the apogee on the left side of the Earth. Orbits in the L_1 Lyapunov family have different periods and stability characteristics, which lead to different arrival rates of the stable manifold. Because of this variation, time of flight away from orbit insertion is not a good metric to define the ROI near the vicinity of the target orbit, instead a physical

boundary in position is used. The ROI near the target orbit is then defined as the area of the left half-manifold that is to the right of $x = 0.7[nd]$ (about 69% of the way to the Moon), since this location represent a point where the manifold arcs slow down as they approach from the Earth, allowing for cheaper non-tangential insertion maneuvers.

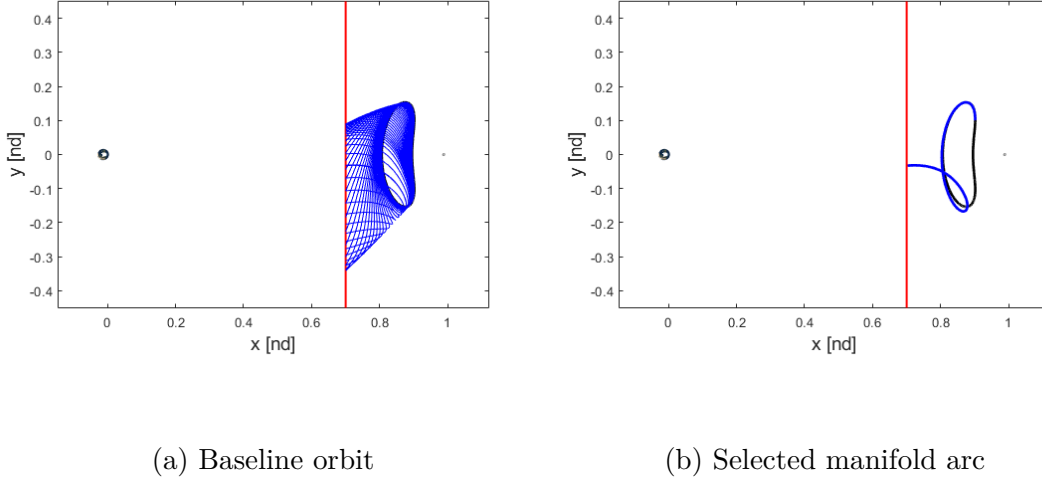


Figure 4.23. Near orbit ROI for baseline orbit

Continuation Methodology

A single arc on this half-manifold is selected and a trade space of transfer solutions is constructed. Starting with a non-tangent transfer solution previously computed at an insertion location of 0 days, a continuation scheme along insertion location is used to build a family of solutions. Notice that ZMPs are not a point of concern once the constraint for the insertion maneuver to be tangential is removed, as the velocity direction at the insertion location does not pose any issues for convergence with this formulation. Two different TOF quantities are then defined; the transfer arc TOF, which corresponds to the time from departure to manifold insertion, and total TOF, which corresponds to the time from departure to orbit insertion (transfer arc TOF plus time spent on manifold arc). To prevent the system from being under-constrained, transfer arc TOF is fixed for the corrections process. Then, a continuation scheme along TOF is implemented, where all the solutions along insertion location are computed for a given TOF before continuing to the next. To

conduct this continuation, the converged solution at a given insertion location with transfer arc TOF $k-1$ is used as an initial guess for the same insertion location and transfer arc TOF k . Once this initial solution at the new TOF is computed, it is continued onto the rest of the manifold arc (i.e., only a single solution at a given insertion location is continued along TOF, before being subsequently continued along insertion location).

Transfer Solutions

A sample set of computed transfers for different transfer arc TOF is shown

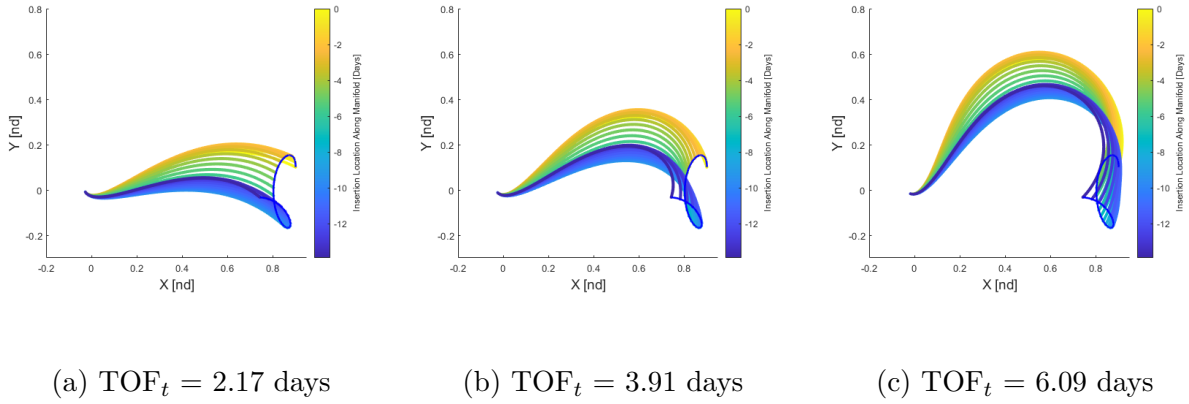


Figure 4.24. Sample transfers to baseline orbit ROI

where TOF_t refers to the transfer arc TOF. This application of continuation in two directions generates a surface of transfer solutions. The insertion ΔV variation along this surface is seen in Figure 4.25. Notice that the transfers with the shortest transfer arc TOF display the highest insertion cost, as they approach the insertion location at non-ideal angles and high velocity. Additionally, notice that the lowest ΔV transfers do not necessarily correspond to highest computed transfer arc TOF, instead they lay at some intermediate location along the surface. Finally notice that the lowest insertion ΔV magnitude varies depending on insertion location.

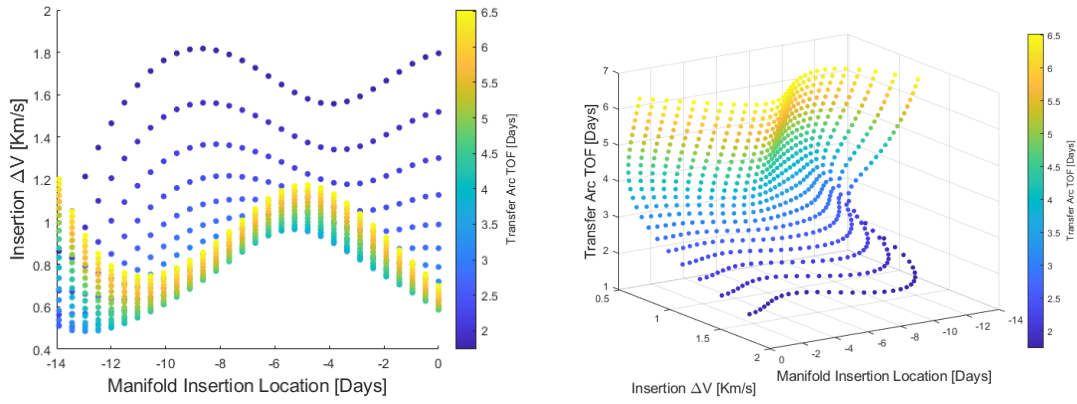


Figure 4.25. Insertion ΔV for ROI

Next, consider how the TLI varies along the surface of solutions

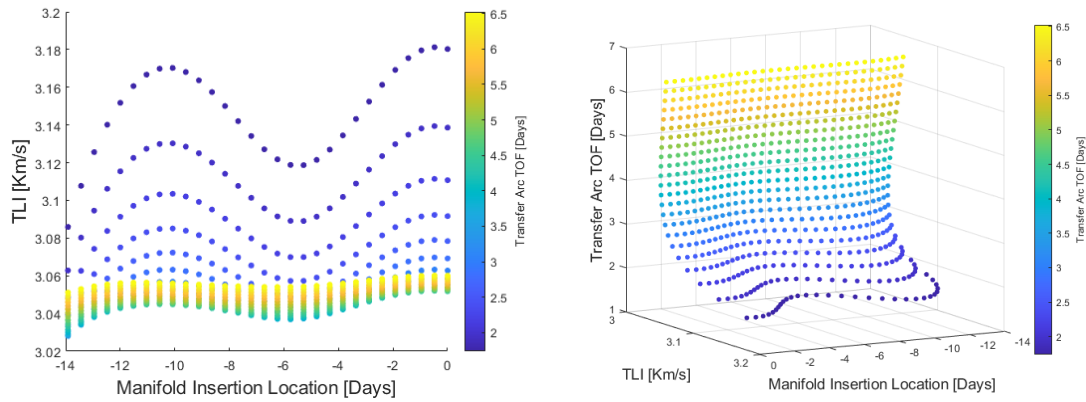


Figure 4.26. Trans-Lunar Injection for ROI

Notice that TLI remains bounded over a small range or maneuver sizes for most of the surface, with the exception of the shortest transfer arc TOFs, as these solutions require a higher departure speed in order to reach the target location in the desired time. This increase in TLI for the shorter transfer arc TOF transfers increases the energy gap that needs to be overcome at the insertion location, leading to higher insertion cost as seen in Figure 4.25. This observation is confirmed by evaluation the relationship between insertion ΔV and TLI

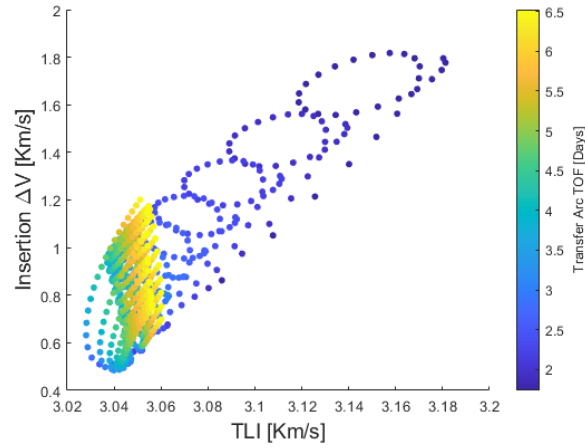


Figure 4.27. Maneuver characteristics for ROI

where the higher TLI transfers clearly show an increasing insertion ΔV cost. Finally, consider the departure angles available for the computed set of transfers

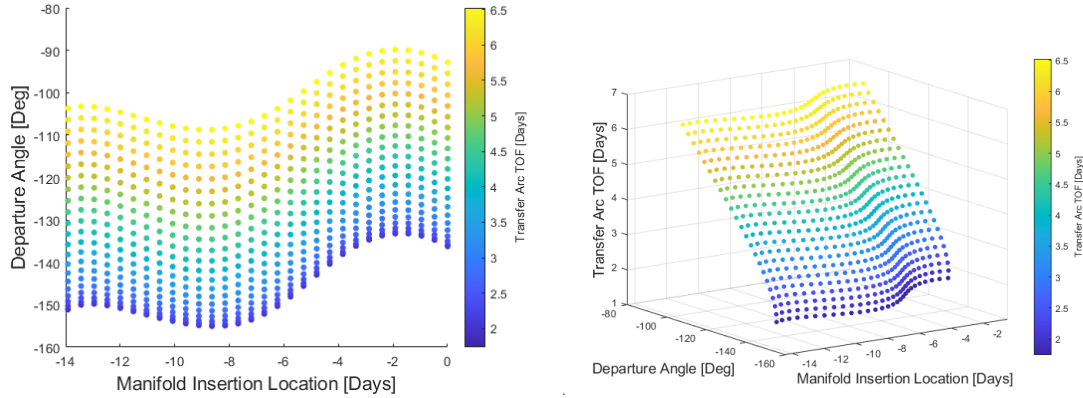


Figure 4.28. Departure angle for ROI

Notice that a larger range of departure angles are available as compared to the direct insertion transfers, shown in Figure 4.5. However, transfer arcs are still bounded to depart from the third quadrant around the Earth. A similar analysis is then conducted for the ROI that lays in the vicinity of the first apogee on the left side of the Earth. This ROI is defined as the region within 2.5 days of the apogee on the manifold arc. A representation of this region in the sample baseline manifold arc is shown

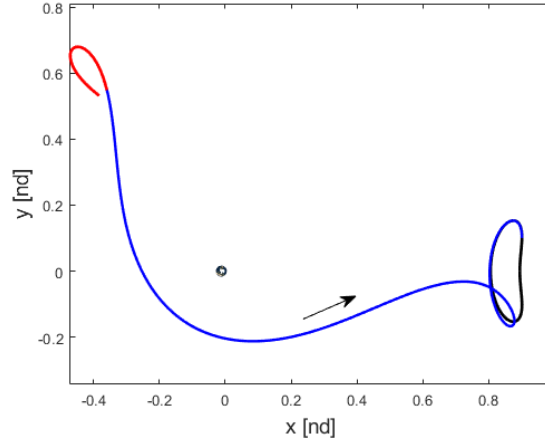
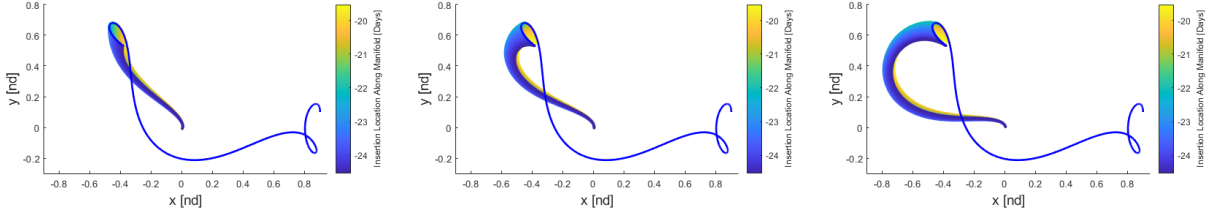


Figure 4.29. Apoapse ROI definition visualization

where the baseline orbit is shown in black, the selected manifold arc is shown in blue and the ROI in question is shown in red. The same methodology to generate a family of transfers is applied to this ROI; a previously computed non-tangent transfer solution is used as starting point, before continuing the solution to different insertion locations within this ROI, and continuing to other transfer arc TOFs. A sample set of transfer geometries available to the apogee ROI is shown



(a) $\text{TOF}_t = 2.17$ days

(b) $\text{TOF}_t = 3.91$ days

(c) $\text{TOF}_t = 6.09$ days

Figure 4.30. Sample transfers to baseline orbit apogee ROI

A surface of transfer solutions is again generated leveraging this multidimensional continuation scheme, as seen in Figure 4.31. Notice the larger availability of low insertion ΔV as

compared to the near orbit ROI (Figure 4.25), at the expense of a larger total TOF before reaching the target orbit.

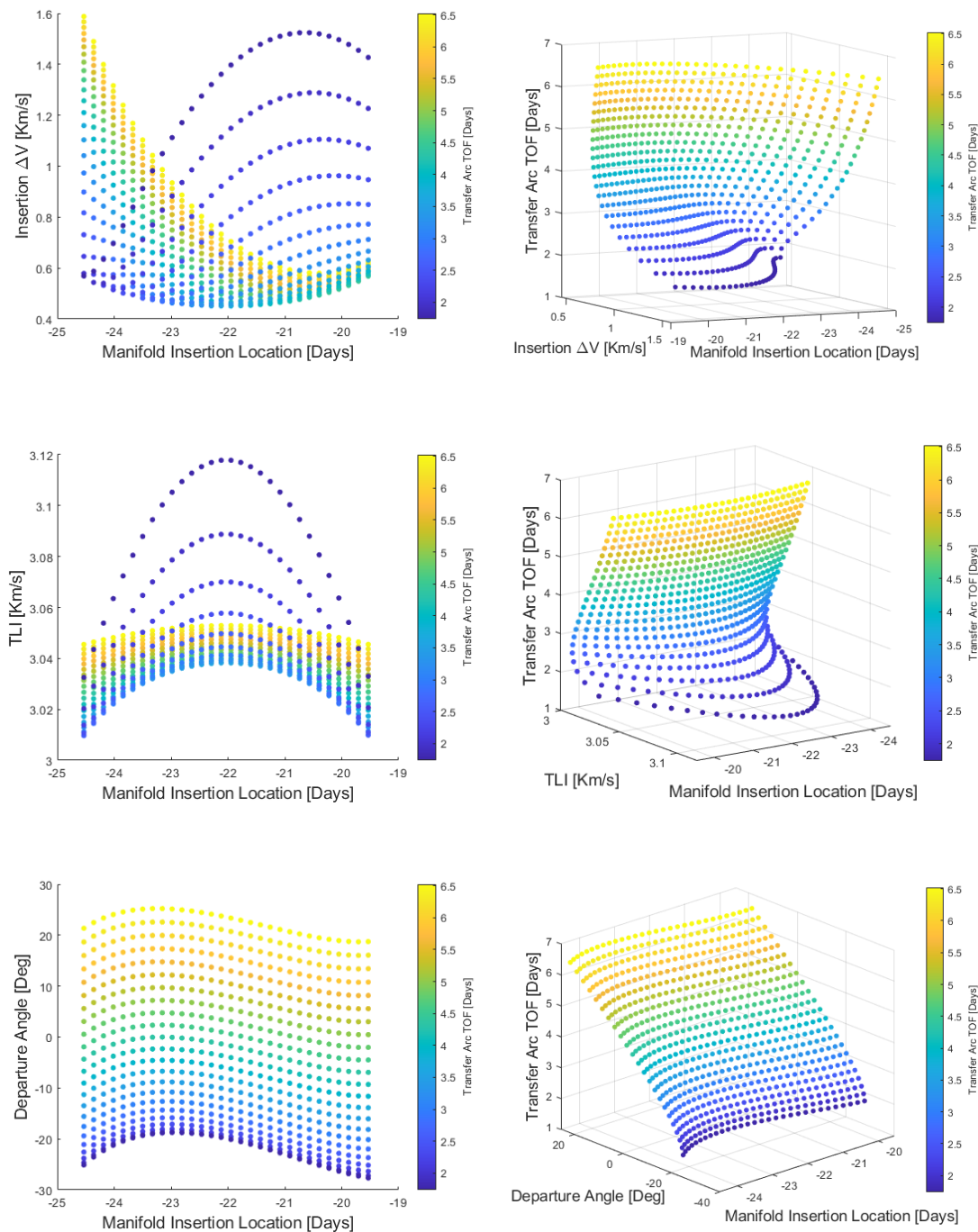


Figure 4.31. Transfer characteristics for apoapse ROI of baseline orbit

Notice the larger availability of low insertion ΔV as compared to the near orbit ROI (Figure 4.25), at the expense of a larger total TOF before reaching the target orbit. Additionally, notice that transfers with longer transfer arc TOF show larger insertion maneuvers in the region before apogee (insertion location < -22 days) and lower insertion maneuvers in the region after apogee, while transfers with shorter transfer arc TOF show the opposite trend. Evaluating Figure 4.30 suggests that this trend is explained by the velocities aligning more closely in the low cost regions, as transfers with short transfer arc TOF (a) display an insertion angle closer to zero in the region before apogee, while transfers with long transfer arc TOF (c) display an insertion angle closer to zero in the region after apogee. Notice again that TLI remains bounded over a small range for the majority of the surface, apart from it quickly raising to accommodate for the short transfer arc TOFs selected.

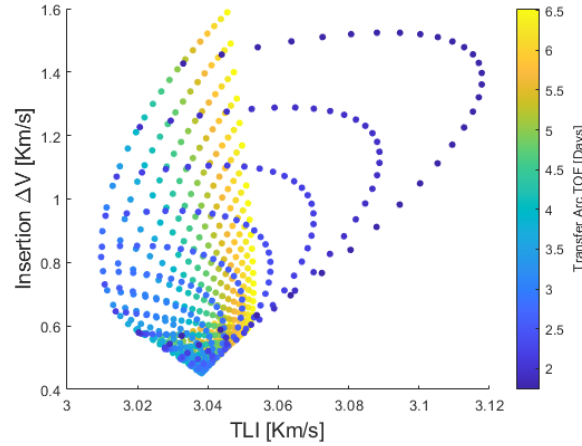


Figure 4.32. Maneuver characteristics for apoapse ROI

Notice that in this case not all solutions that possess higher insertion maneuvers also possess higher TLI values. That is, some of the solutions with TLI in the bounded region also possess high insertion maneuvers, in contrast to the other ROI, seen in Figure 4.27. This is attributed to the directionality of the insertion maneuver as described above, and corroborated by Figure 4.33

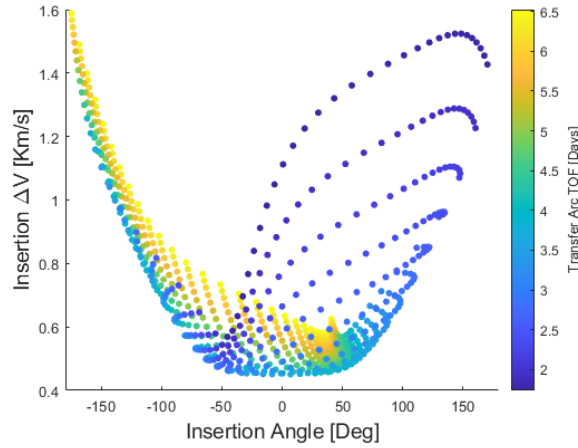


Figure 4.33. Insertion angle variation for apoapse ROI

where, as solutions approach ± 180 degrees, the insertion cost rapidly climbs. Additionally, notice that the high insertion cost solutions that possess more favorable insertion angles correspond to the solutions with shorter transfer arc TOF and higher TLI values seen in Figure 4.32. Finally, notice from Figure 4.31 that the departure arcs for the computed solutions remain bounded. However, these bounds are different than the ones seen in Figure 4.28. While the ROI near the target orbit displays transfer solutions that depart from the third quadrant around the Earth, the ROI near apogee contains solutions that depart from the first and fourth quadrants around the Earth. This variety provides flexibility in mission design, as different departure characteristics that can be leveraged, are included within this trade space.

4.3.1 Continuation to Alternate Manifold Arcs on Single Orbit

Traditionally, spacecraft don't target a specific manifold arc for insertion, apart from rendezvous missions. Instead, spacecraft tend to have a desired target orbit or a range of desired target orbits that they arrive upon to achieve their mission. Hence, transfers to a single manifold arc of a desired periodic orbit may not accurately represent the breadth of transfer options available for a mission. Given that manifold arcs are simply members of a continuous manifold surface, a continuation scheme is implemented to transition solutions from the presented manifold arc to other manifold arcs on the baseline orbit.

Continuation Methodology

A methodology to continue solutions for a single manifold arc has been previously defined. In order to expand this methodology to additional manifold arcs, a single solution at a given insertion location and TOF is used as an initial guess to transition from the current manifold arc to the next. After this first solution is converged, the transfer space for the entire manifold arc is, then, computed using the methodology previously described. Here, after the first solution for each manifold arc is computed, the transfer space for each manifold arc is computed independently from the rest.

Transfer Results

First, focus on the ROI near the target orbit, and choose a set of manifold arcs along the surface, as shown in Figure 4.23. Notice that, since transfers are continued in three separate dimension, a volume of available transfer solutions arises. This volume of solutions is comprised of continuously varying surfaces that each correspond to an individual arc within the manifold. Recall that the boundary of the ROI near the target orbit is not defined based on a specific time along the manifold arc, but instead as a location in space. From this definition, notice that if the surfaces are characterized using the previously seen definition of manifold insertion location (in days), the surface will span different ranges in this dimension, as different manifold arcs will take varying amounts of time to reach the defined boundary. To overcome this circumstance, a new definition of manifold insertion location is used for this ROI, normalizing each curve by the time at which the manifold arc intersects $x = 0.7$, so that the insertion location is defined as a percentage of time along the corresponding manifold arc. A sample set of surfaces using this definition is shown in Figure 4.34, where the red arc represents the arc used to generate the surface, 0% along the manifold represents the intersection with the orbit, and 100% along the manifold represents the intersection with $x = 0.7$. Notice that solutions are now colored by total TOF instead of transfer arc TOF. Additionally, since the curve representing the manifold arcs is a closed curve, the evolution of the solution surfaces is periodic.

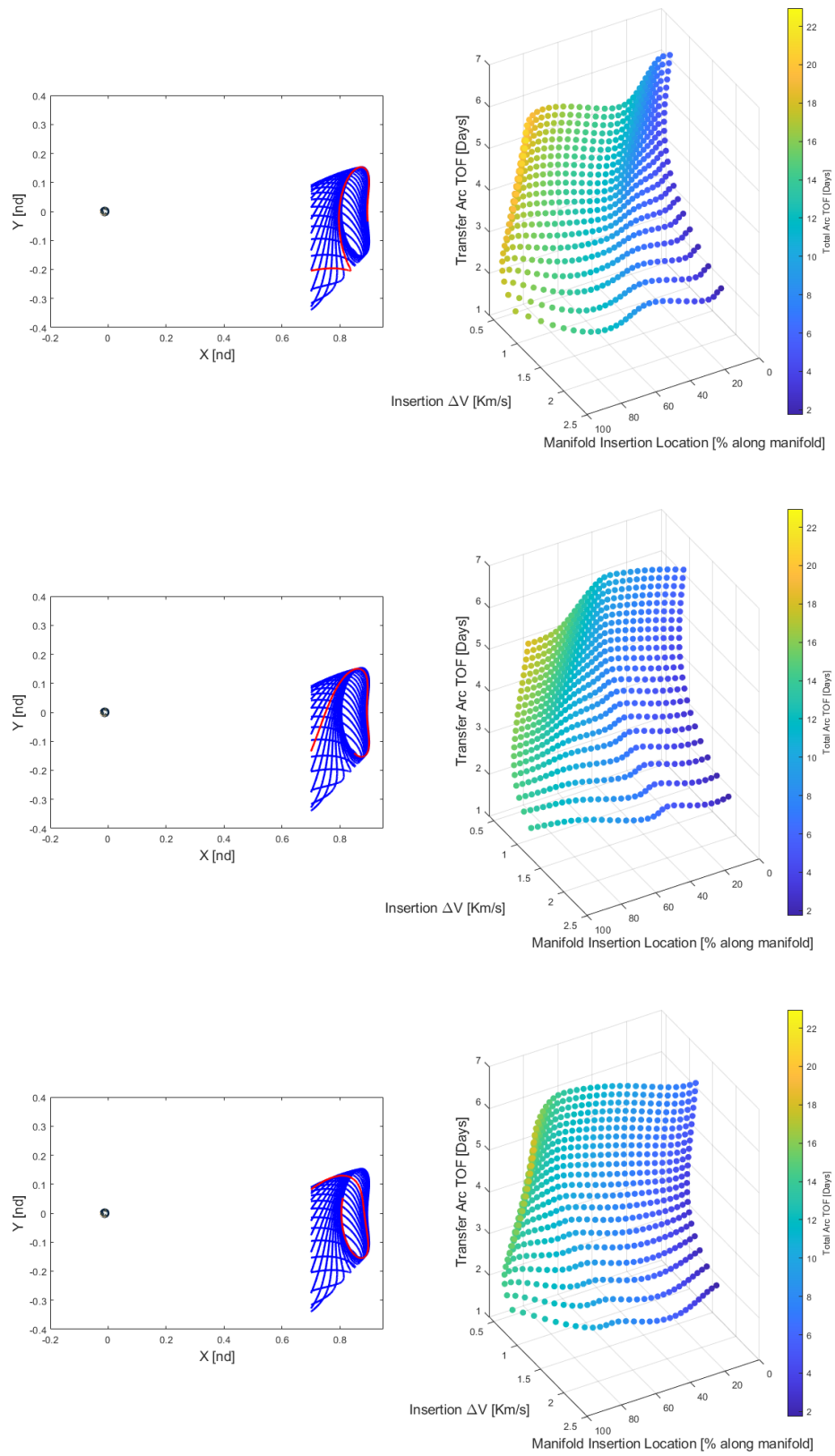


Figure 4.34. Solution surface evolution for different manifold arcs of baseline orbit

Notice that for this volume of solutions, the minimum insertion cost at all insertion locations remains around 450-500 m/s, in contrast to Figure 4.25, where the minimum insertion cost varied heavily with insertion location.

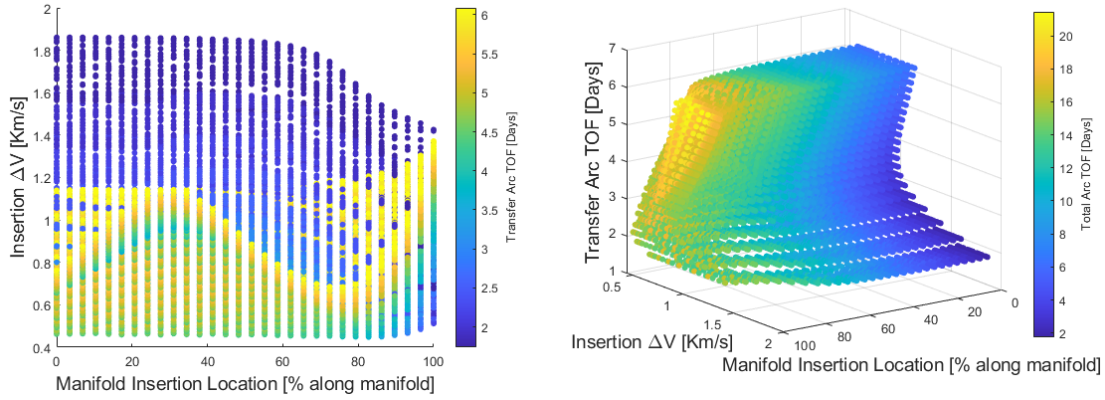


Figure 4.35. Insertion ΔV for ROI

Additionally, notice that most of the high cost solutions result from short arc TOFs as seen previously for the single arc.

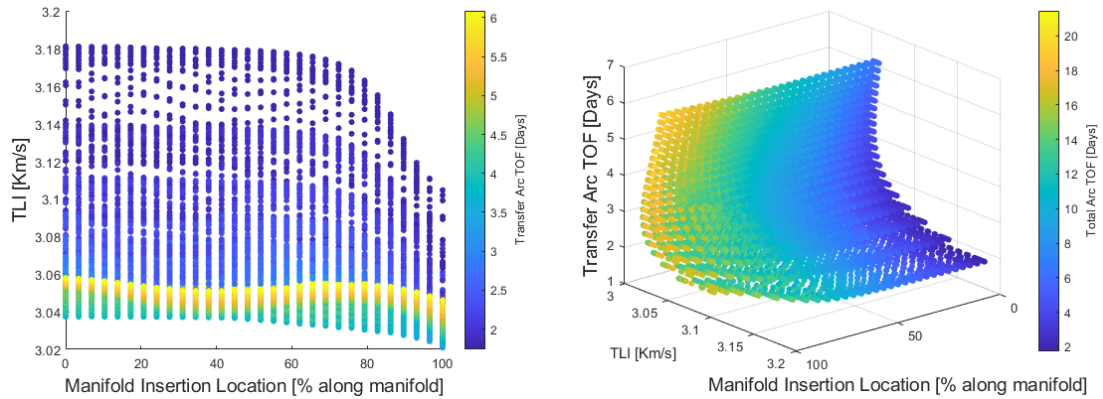


Figure 4.36. Trans-Lunar Injection for ROI

Again, notice that the TLI of the computed transfers remains bounded to a small range of values for the majority of the volume, with the exception of solutions that possess a short

transfer arc TOF, since a higher TLI is required to reach the vicinity of the orbit in a shorter amount of time.

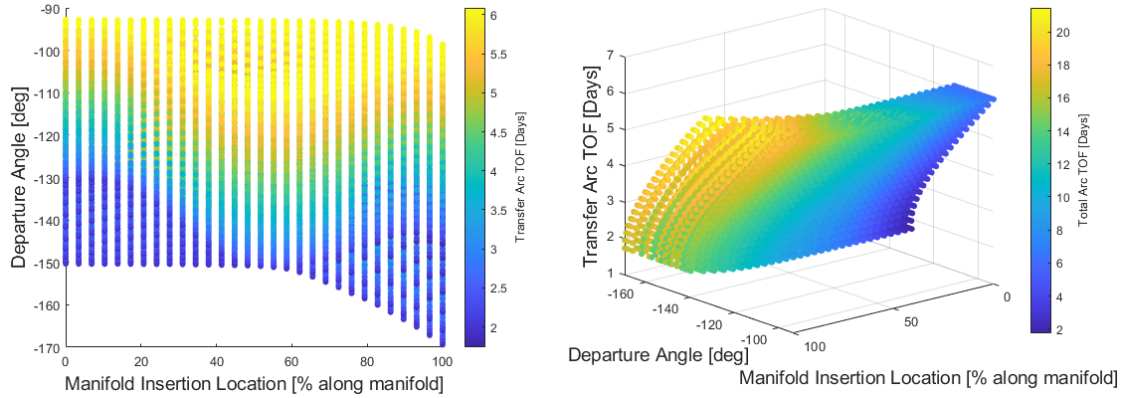


Figure 4.37. Departure angle for ROI

Further, notice that an increased range of departure angles is available, as compared to Figure 4.28, though, solutions are still bounded to the third quadrant around the Earth.

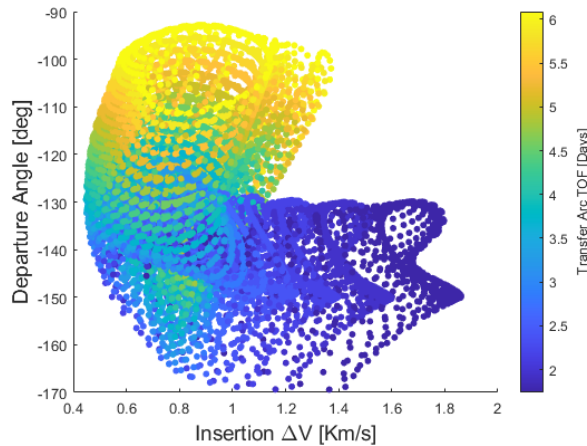


Figure 4.38. Insertion cost of solutions at various departure angles

Also, note, that not only is there solutions available over the shown range of departure angles, but there are relatively low insertion cost solutions for the majority of the range considered, with the exception of the -160 to -170 degree range, where the minimum insertion cost rises to between 700-800 m/s. Similarly, this methodology is applied to the ROI near the first

apogee prior to Earth fly-by. Since the time of flight along the manifold, between apogee and orbit insertion, varies for different manifold arcs, surfaces along the volume representing transfers to this ROI will span different ranges of the initial definition for manifold insertion location. To overcome this, an alternate definition of insertion location is devised, using days away from apogee as the characteristic that provides insertion location information, since this is how the ROI is defined.

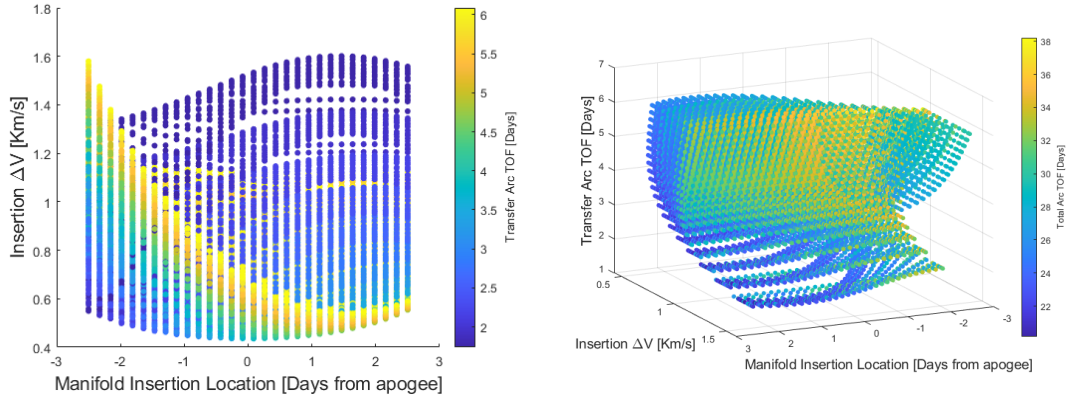


Figure 4.39. Insertion ΔV for apoapse ROI

Insertion maneuver cost displays similar characteristics as those seen in Figure 4.31, where negative time represents days before reaching apogee. Notice again that low-cost solutions appear at all insertion locations relative to apogee, with low transfer arc TOF solutions favoring insertion locations before apogee and high transfer arc TOF solutions favoring insertion locations after apogee. Additionally, notice the large range of total transfer TOFs available (21-38 days) for this ROI.

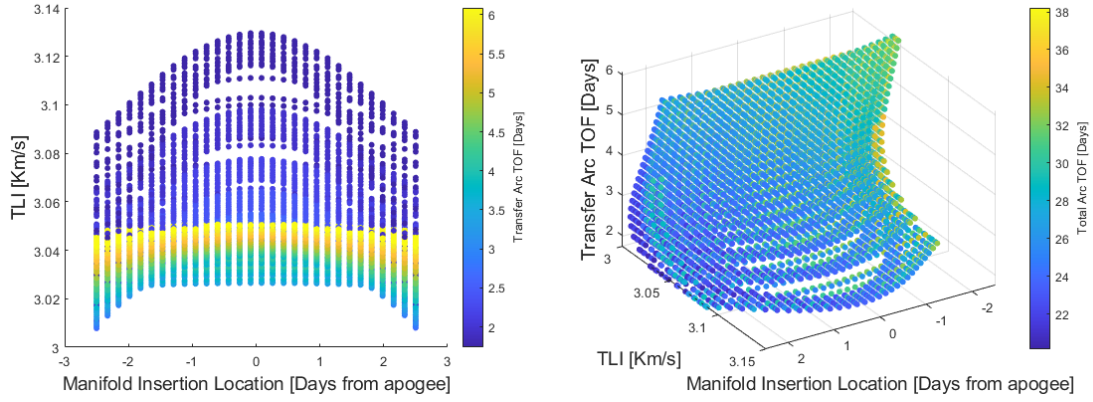


Figure 4.40. TLI for apoapse ROI

TLI characteristics for all manifold arcs along the baseline orbit closely resemble those for the initially computed arc in Figure 4.31, where TLI remains bounded over a small range of values for most transfer solutions, with the exception of the short transfer arc TOF transfers, as a higher departure velocity is required to reach the insertion location in the desired amount of time, as described previously.

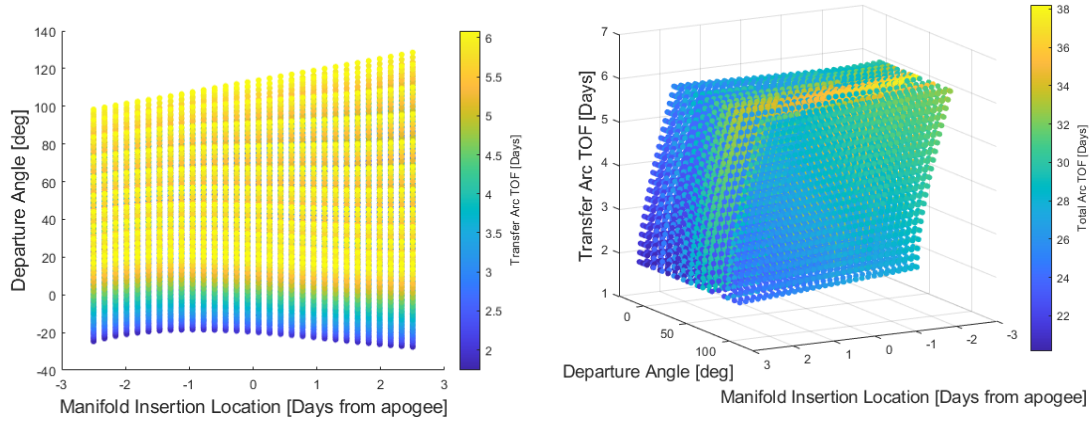


Figure 4.41. Departure angle for apoapse ROI

Additionally, transfer solutions to this ROI display an increased range of departure angles available, as compared to the ROI near the target orbit. Again, the displayed departure

angles not only encompass a larger range, but they cover an entirely different set of angles (-25 to 125 degs), as compared to those available for the ROI near the target orbit (-170 to -90 degs). However, in contrast to Figure 4.38, a smaller percentage of departure angles available possess insertion maneuvers in the lower range of cost. While approximately 86% of the available departure angles possess solutions with an insertion maneuver < 700 m/s in Figure 4.38, only about 65% of the available departure angles display this behavior.

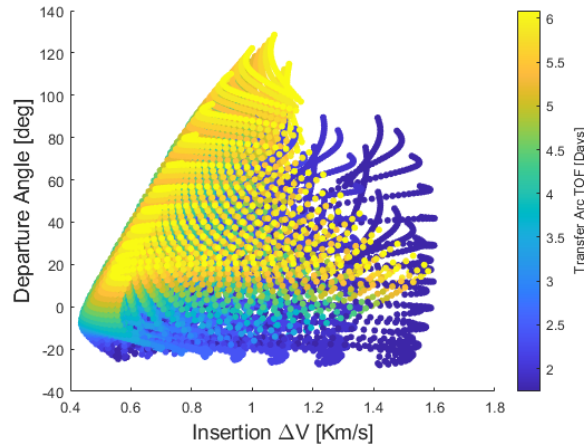


Figure 4.42. Insertion cost of solutions at various departure angles

The volumes displayed in this section provide a representation of the available trade space of transfer solutions, that leverage stable manifold arcs into the baseline orbit, for the TOF and ROIs considered.

4.3.2 Continuation to Similar Manifold Arcs on Additional Orbits Along the Family

The volumes of solutions computed for the baseline orbit provide a plethora of available transfer solutions. However, transfer solutions to additional orbits in the L_1 vicinity are of equal interest. As suggested in section 4.2.2, manifold arcs and transfer solutions maintain similar characteristics for different orbits in the L_1 Lyapunov family. Therefore, solutions can be continued from one orbit to the next along the family. Manifold arcs from a range of L_1 Lyapunov orbits (24,000-79,000 km \hat{y} -amplitude) are selected to implement this continuation scheme. Similar manifold arcs are chosen along the family by stepping from the orbit onto

the manifold at similar locations along each orbit. Recall that one can step onto the manifold at any location along the orbit. This location is characterized by a certain TOF away from the perpendicular crossing nearest to the moon. Then, to maintain this similarity across orbits, a parameter to represent the location at which the step onto the manifold occurs, is defined as $\tau = \frac{TOF_{pc}}{T_p}$, where TOF_{pc} is the TOF from the perpendicular crossing nearest to the moon to the step off location, and, T_p is the period of the orbit at hand. This definition is analogous to the percentage of the TOF along the orbit at which the step off onto the manifold is conducted. An implementation of this strategy, provides the manifold arcs that are used for this continuation scheme, as shown

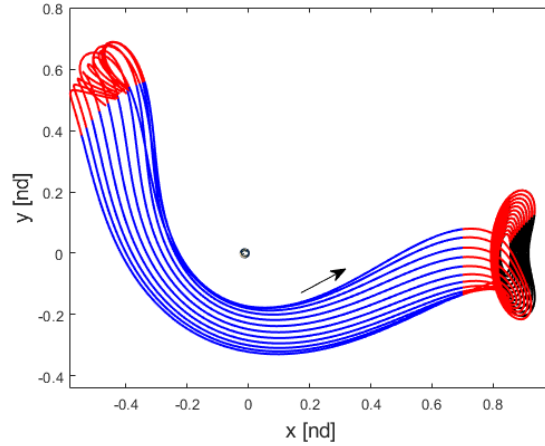


Figure 4.43. Similar manifold arcs along L_1 Lyapunov family

where the target orbits are shown in black, and the ROIs are shown in red.

Continuation Method

Continuing from one manifold arc to a similar arc in a nearby orbit is a similar process to continuing from one manifold arc to the next one along the same orbit. Hence, a similar process is used. A single solution at a given insertion location and TOF is used as an initial guess to transition from the current orbit to the next in the family. Again, once this first solution is computed, the process outlined to build a surface of solutions for a given manifold arc is followed.

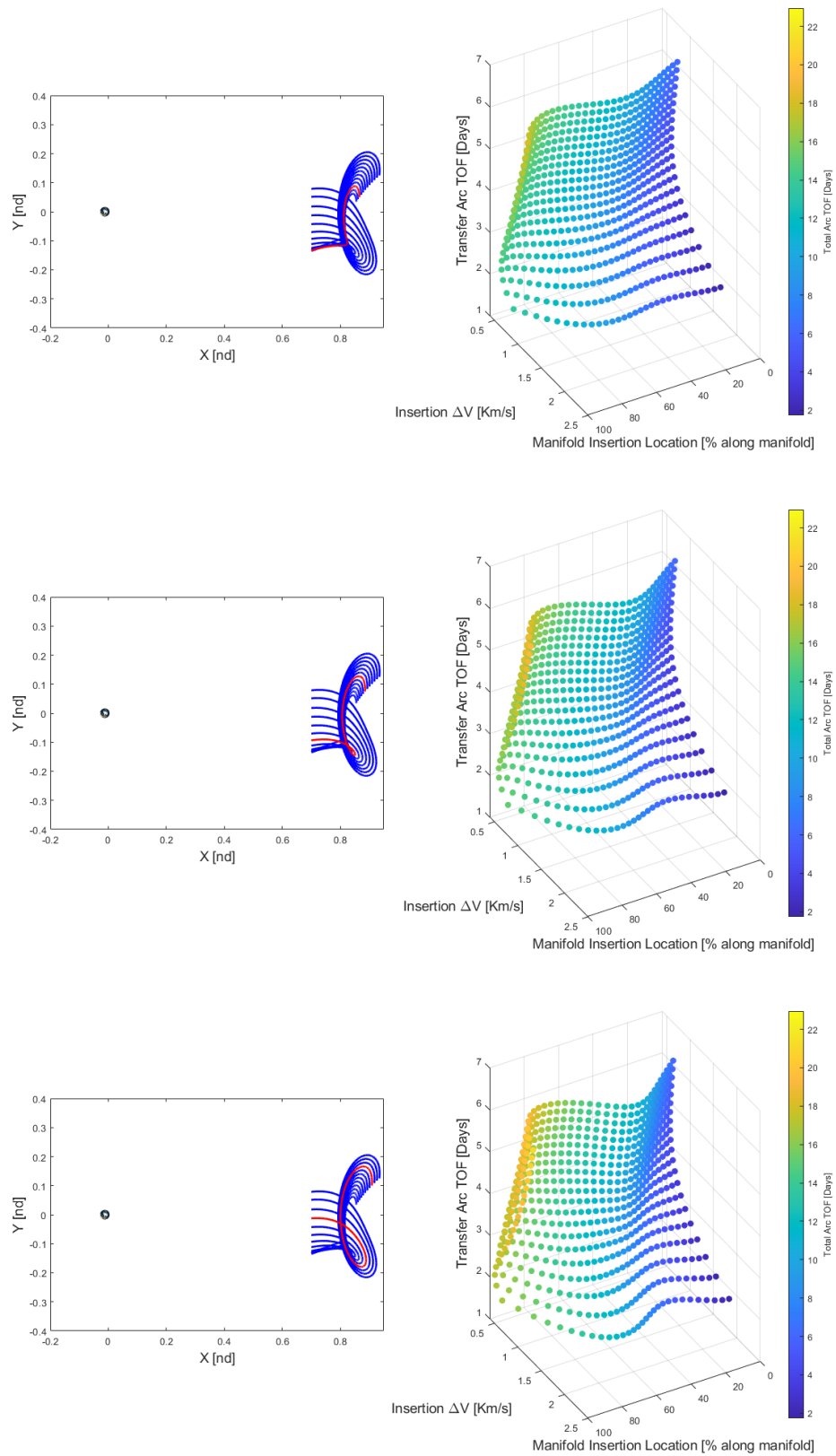


Figure 4.44. Solution surface evolution for manifold arcs of varying orbits

Transfer Solutions

First, focus on the ROI near the target orbit. Recall that since we are continuing in three dimensions, a volume of solutions arises. This volume is comprised of surfaces, where each surface represents the manifold arc of a different orbit. Since the orbital family is not represented by a closed curve, the evolution of these surfaces will not be periodic as seen in the previous example. The evolution of these surfaces is depicted by displaying a subset of them, as the continuation process progresses through orbits of increasing amplitude, as seen in Figure 4.44. Notice that the surfaces shown all display fairly similar shape, in contrast to Figure 4.34, which shows much more variation from one surface to the next. This small variation in surfaces suggests that a small, contained, volume is formed from this continuation process.

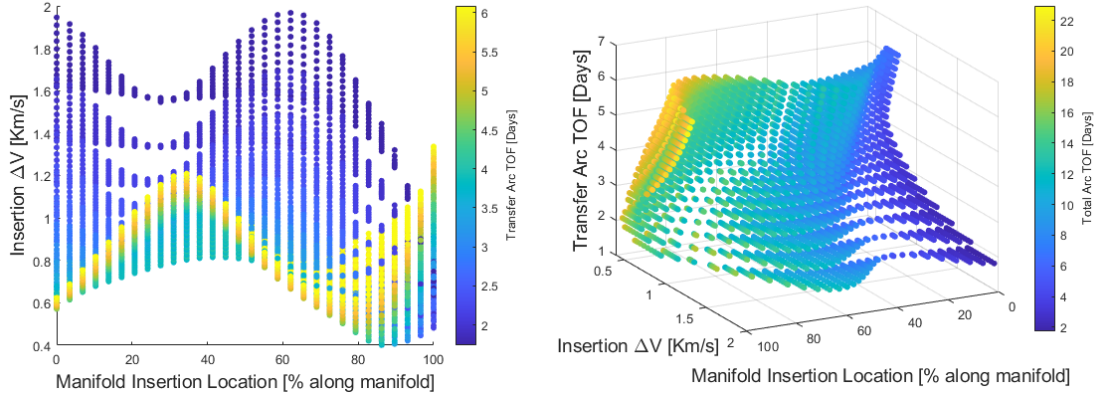


Figure 4.45. Insertion ΔV for ROI

Notice that the volume of solutions remains remarkably similar to the surface displayed by the single manifold arc, as seen in Figure 4.25 (the x-axis of these plots are inverted as 100% along the manifold corresponds to the insertion location furthest away from the target orbit). In contrast, Figure 4.35 displays a much larger trade space of solutions when continuing to other manifold arcs on the same orbit, and produces a larger volume.

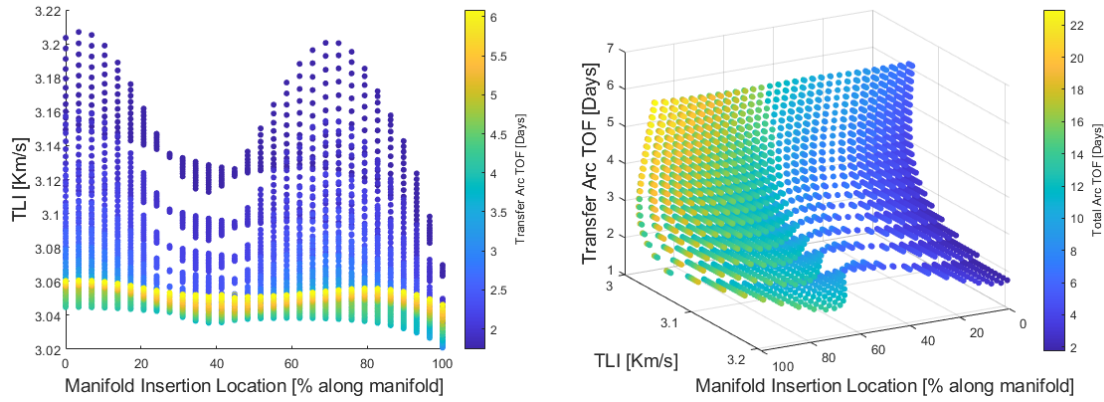


Figure 4.46. Trans-Lunar Injection for ROI

Again, TLI displays bounded motion for the majority of the space, with the exception of short transfer arc TOF solutions where the TLI increases significantly. Similarly to the insertion maneuver cost, this volume of solutions remains largely similar to the surface generated for a single manifold arc, seen in Figure 4.26, while the continuation to other manifold arcs on the same orbit shows a much larger volume.

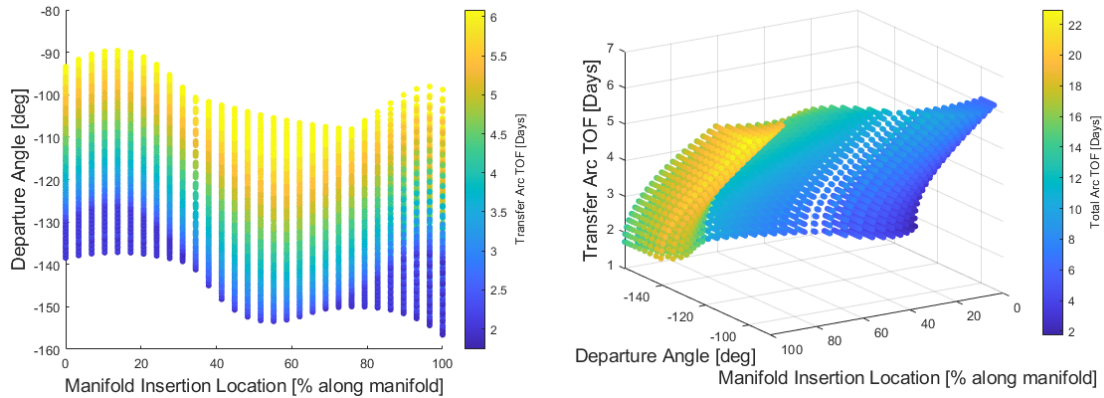


Figure 4.47. Departure angle for ROI

The departure angles available in the volume of solutions generated again remains in the near vicinity of the surface generated for a single manifold arc, as seen in Figure 4.28. So, if the geometry from the selected manifold arcs is desired, the departure characteristics remain

fairly bounded to the range shown above. The evolution of the surfaces throughout the volume is also visible when coloring transfer solutions by orbital amplitude as

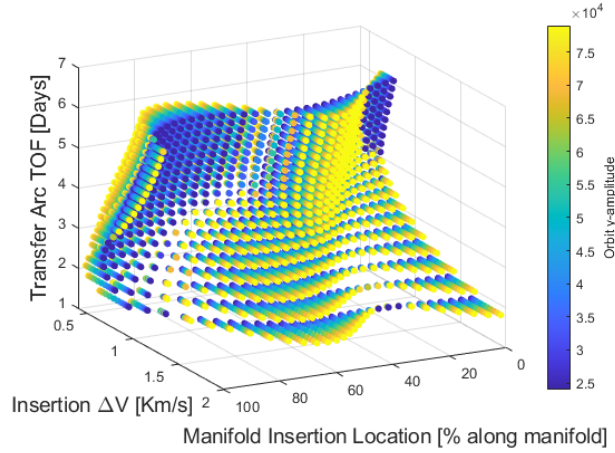


Figure 4.48. Surface variation along L_1 Lyapunov family

Again, notice that solutions vary continuously and show limited deviation from the smallest to the largest orbit considered. From these results, it is fair to say that variation in the solution space to the ROI near the target orbit, is much larger along different manifold arcs on the same orbit, than it is for similar manifold arcs on different orbits of the L_1 Lyapunov family.

To analyze the variation in transfer characteristics to the apogee ROI, along the Lyapunov family, a similar study is conducted for the set of desired insertion locations corresponding to this ROI. The transfer characteristics of the volume generated by this process are shown in Figure 4.49. Similar to the ROI near the target orbit, the volume of solutions is relatively small and contained. This volume does not deviate far from the surfaces generated for the single manifold arc, seen in Figure 4.31 (recall that the x-axis of these plots are mirrors of each other, as 100% along the manifold represents the location furthest away from the target orbit). Insertion maneuvers available display similar values and a matching trend, to the solutions space for a single manifold arc. TLI again remains bounded for the majority of transfer arc TOF, deviating when transfer arc TOF is reduced past a certain point.

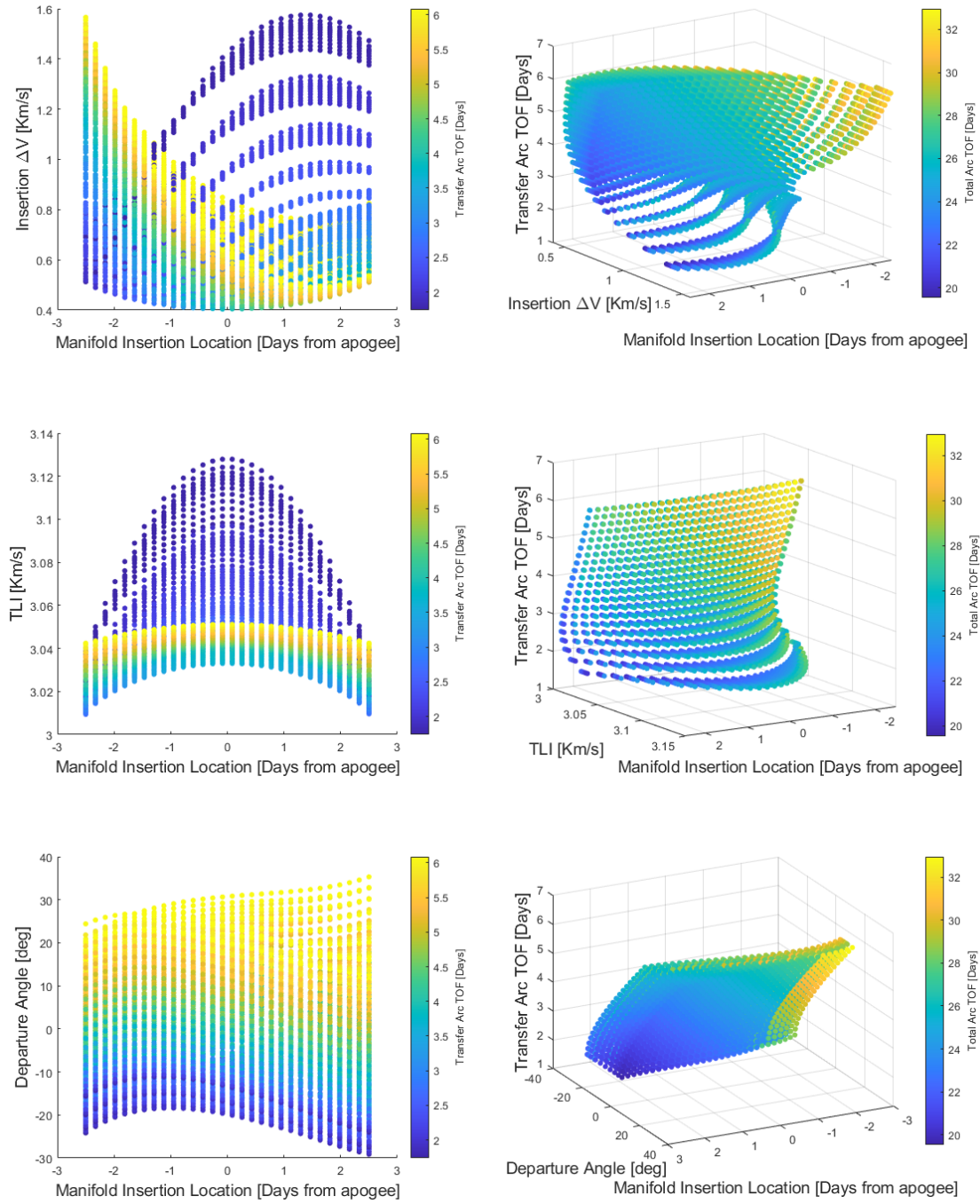


Figure 4.49. Transfer characteristics for apoapse ROI of various orbit

The similarity of departure angles again demonstrates that, if the geometry shown on this manifold arc is desired, a comparable range of options are available regardless of which orbit

along the family is desired. In contrast, recall that continuation to other manifold arcs on the same orbit increased the available departure geometries, as seen in Figure 4.41. Given these transfer characteristics, a similar conclusion is made for the apoapse ROI, as is made for the ROI near the target orbit; variation along different manifold arcs on the same orbit has a much larger effect on the size of the volume of available transfers, as compared to the variation to similar manifold arcs on different orbits of the L_1 Lyapunov family. These results additionally suggest that, a generated volume of transfer solutions to a representative set of manifold arcs on any given L_1 Lyapunov orbit will be similar to the volumes seen in Figures 4.35-4.37 and Figures 4.39-4.41.

4.3.3 Continuation to Several Manifold Arcs Along Family of Orbits

A complete trade space of two-maneuver transfers from LEO to a range of orbits in the L_1 Lyapunov family, not only encompasses a single manifold arc over on each orbit, but, includes all the manifold arcs on each orbit. To create a representation of this space, a set of 12 orbits with 24,000-79,000 km \hat{y} -amplitude is selected, as well as 25 manifold arcs along each of these orbits.

Continuation Methodology

In order to achieve this continuation in one additional dimension, two previous methodologies are combined. A starting orbit is first selected, and the trade space to all of its manifold arcs is computed, using the methodology discussed in section 4.3.1. After this volume of solutions is computed, a single solution is continued from this orbit to the next, following the methodology discussed in section 4.3.2. Next, once this initial solution is converged on the new orbit, it is continued onto the rest of the manifold arcs on this orbit, again, following the methodology described in section 4.3.1. This process is repeated until all the desired orbits have been evaluated. Since continuation occurs in 4 different dimensions (insertion location, TOF, manifold arc and orbit), a 4-dimensional surface of solutions is generated. This higher dimensional surface is comprised of volumes of solutions, each representing one of the orbits analyzed. A representative volume is seen in section 4.3.1.

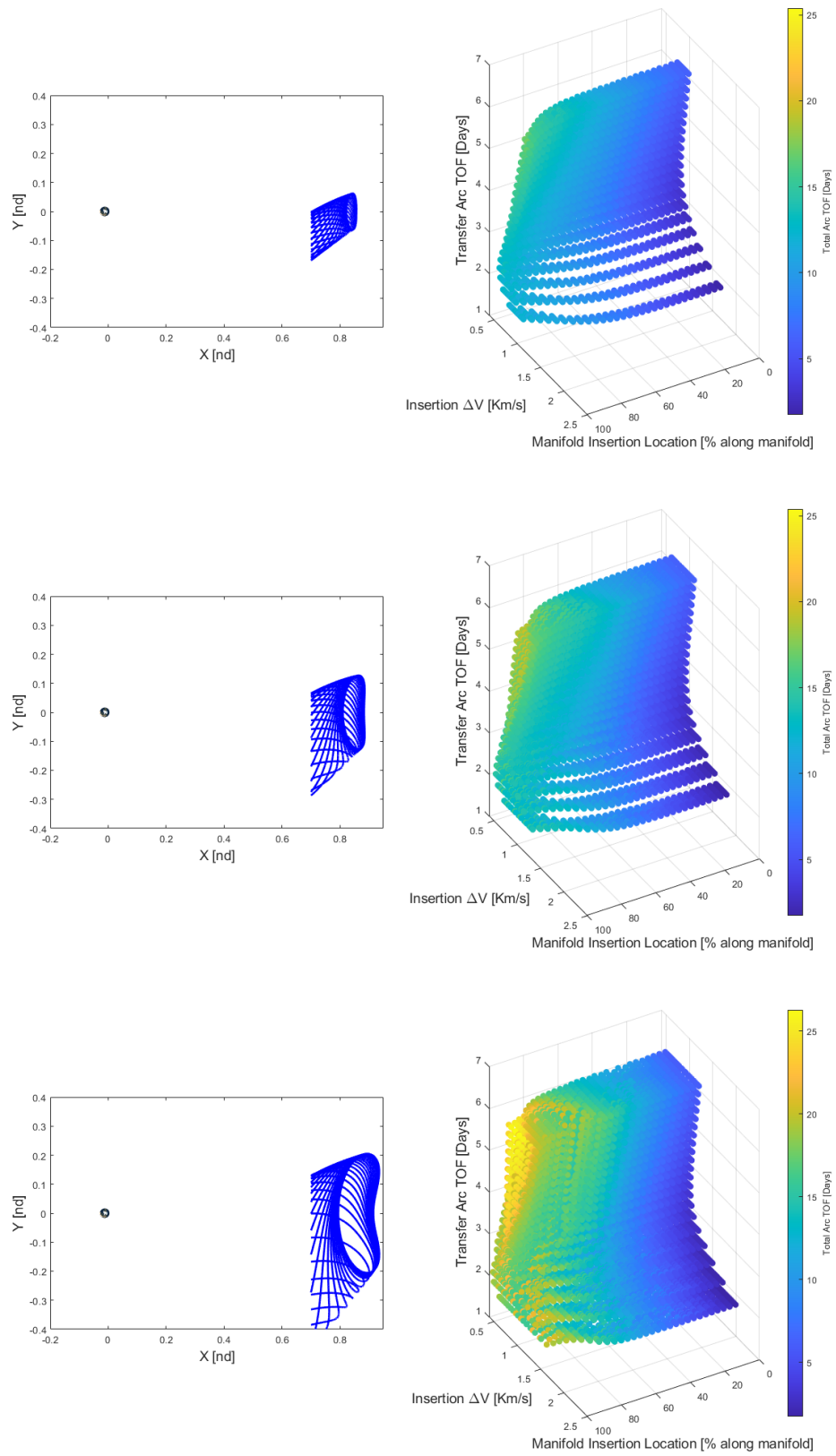


Figure 4.50. Solution volume evolution for manifold arcs of varying orbits

Transfer Solutions

First, focus on the ROI near the target orbit. The evolution of the volumes described along the selected range of the L_1 Lyapunov family is displayed in Figure 4.50. Notice that, as the algorithm progresses through the family, the volumes expand in size, while maintaining similar shape. This evolution suggests that larger amplitude L_1 Lyapunov orbits have a larger variety of solutions available, but maintain similar trade space trends as the smaller orbits in the family. Of course, the transfer characteristics of this 4-dimensional surface can be represented in 2-D and 3-D space, as accomplished previously.

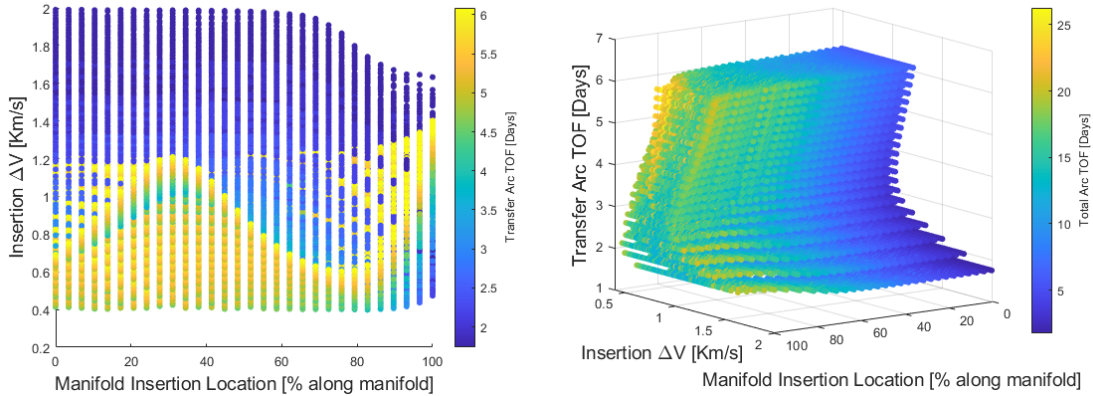


Figure 4.51. Insertion ΔV along L_1 Lyapunov family

Notice the similarity of the insertion ΔV s to the solutions seen in Figure 4.35, particularly, the availability of low cost transfers at all insertion locations along the manifolds analyzed. Note, that, there is an increase in the range of available solutions seen in Figure 4.35, as this 4-d surface of solutions possesses transfers with lower and higher insertion costs. As displayed in Figure 4.50, the volume of available solutions, for each orbit along the family, expands as orbit \hat{y} -amplitude increases.

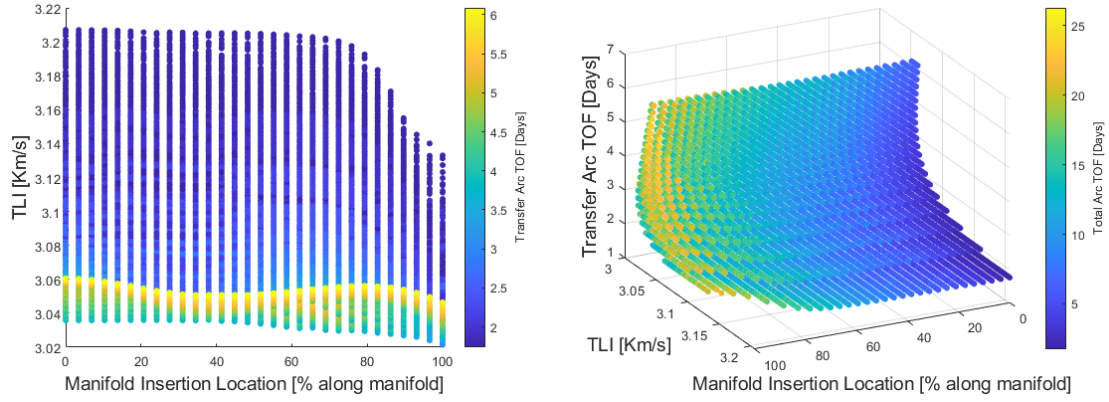


Figure 4.52. TLI along L_1 Lyapunov family

TLI is again bounded to a small region of maneuver costs for the majority of the surface, with the exception of a portion of the low transfer arc TOF transfers, where the TLI increases in order to accommodate the shorter transit time. The total surface trend is repeated from Figure 4.36, as predicted.

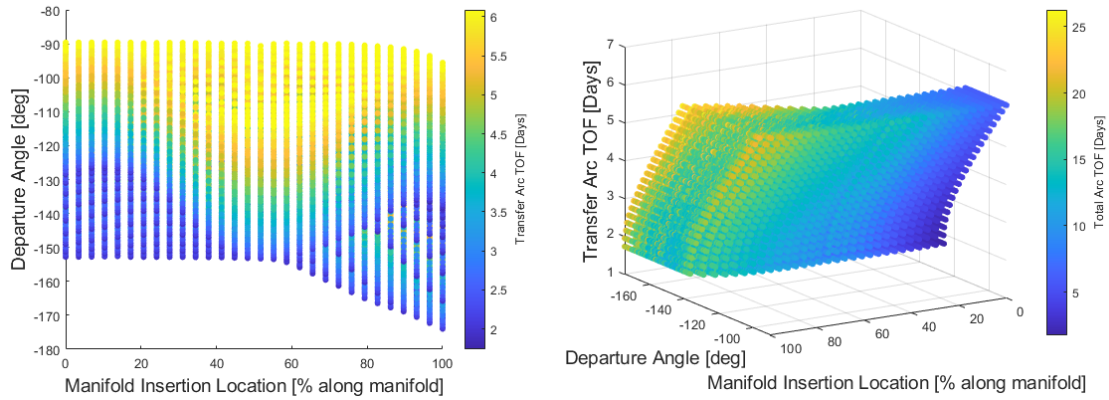


Figure 4.53. Departure angle along L_1 Lyapunov family

Again, notice that the trend from Figure 4.37 is maintained. However, notice that the range of departure angles is slightly increased, with some long transfer arc TOF solutions moving slightly into the fourth quadrant around the Earth. Next, repeat the analysis for the ROI near apogee. The characteristics of these transfer solutions are shown in Figure 4.54.

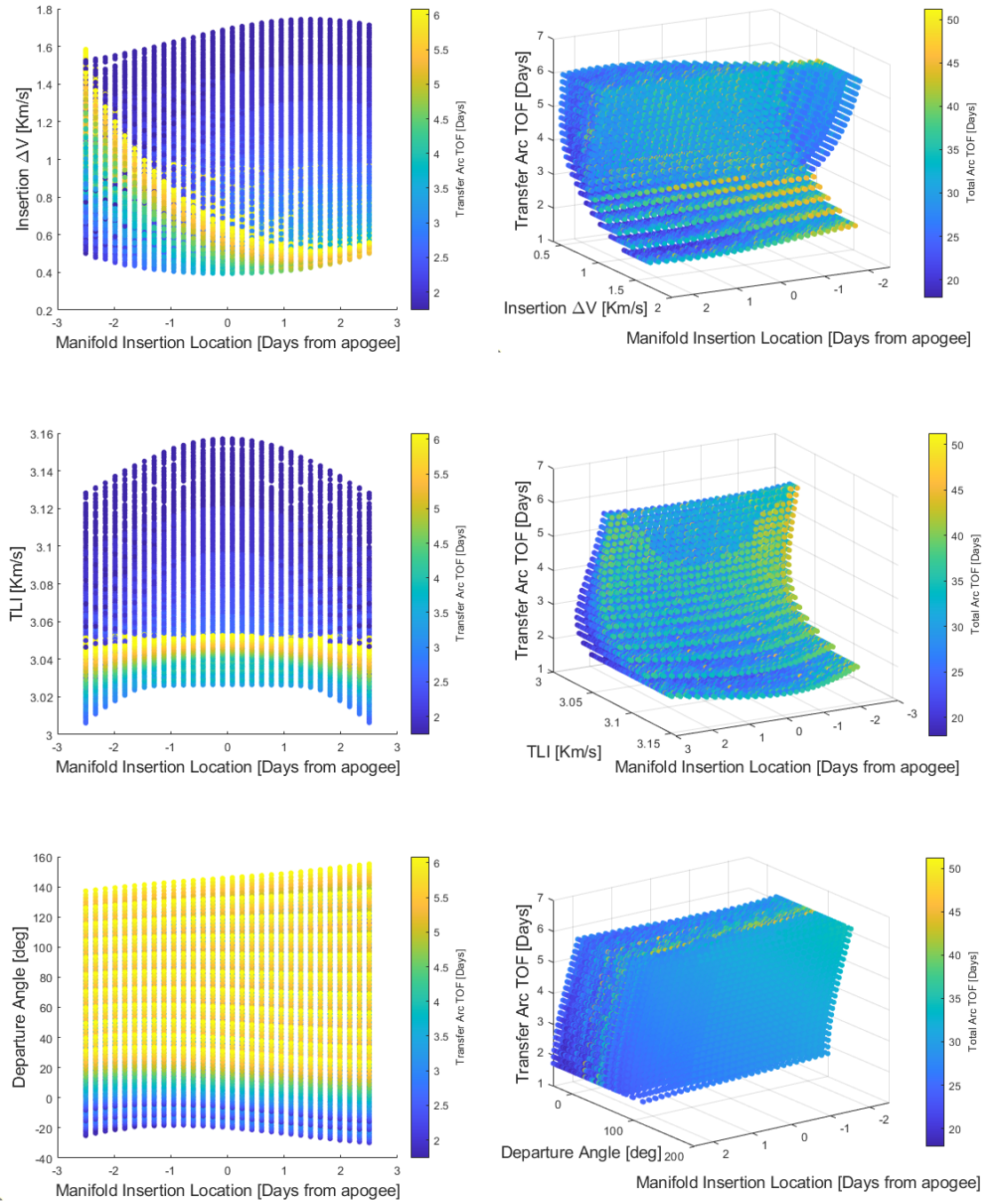


Figure 4.54. Transfer characteristics for apoapse ROI along L_1 Lyapunov family

Again, notice that the solution characteristics closely resemble those seen in Figures 4.39-4.41, as projected. While trends are maintained, notice that the range of available solutions char-

acteristics is increased, as seen in the ROI near the target orbit. Again, notice that the inclusion of larger L_1 Lyapunov orbits provides transfer options that possess departure angles outside of the range displayed in Figure 4.41. Additionally, the range of departure angles at which there is an insertion maneuver < 800 m/s available also increases.

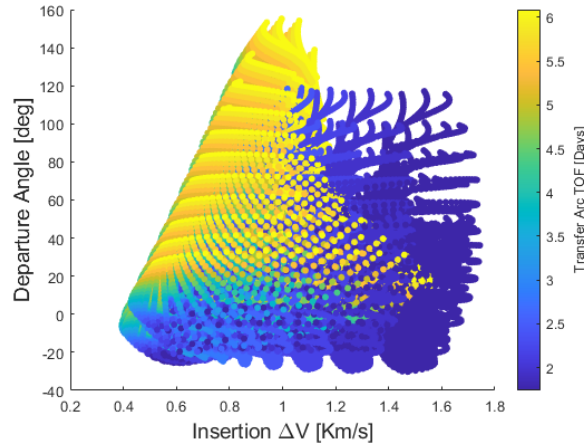


Figure 4.55. Insertion cost of solutions at various departure angles

Notice that the upper boundary on this condition is increased to approximately 120 deg, from just under 90 deg, as seen in Figure 4.42. As predicted in section 4.3.2, the trade space of solutions encompassing all the manifolds of the range of L_1 Lyapunovs selected closely resemble the volumes of transfer solutions calculated in section 4.3.1. These solution spaces computed, represent the entire set of available transfers to the ROIs, within the transfer arc TOFs defined. These 4-dimensional surfaces can be leveraged to select a desirable transfer that satisfies the conditions necessary to achieve a mission at hand.

5. SUMMARY AND FUTURE WORK

5.1 Investigation Summary

With the introduction of the gateway program, there is an increase in proposed missions to the cislunar vicinity, that leverage structures from the Earth-Moon Circular Restricted Three-Body Problem (CRTBP). Knowledge of transfer characteristics from Low Earth Orbit (LEO) to orbits in the lunar region is of great interest, as it allows for rapid mission design. Explicitly, this study focuses on relatively short time of flight, two-maneuver, transfers from a 500 km altitude LEO to the L_1 Lyapunov family of orbits. Underlying structures of the space are utilized in order to facilitate the construction of said transfers. A large set of transfers is generated and their characteristics are evaluated. From these transfer characteristics, a set of key takeaways arises:

- While a tangential maneuver in the CRTBP represents the minimum required ΔV to bridge the energy gap between two arcs, non-tangent transfers provide additional flexibility in departure arc geometry and energy. This flexibility allows for insertion maneuvers that possess a smaller energy gap than their tangent counterparts, even if the maneuver direction is sub-optimal. From this, non-tangent transfers provide viable low-cost solutions at an increased range of locations, when compared to tangential transfers.
- Transfers leveraging right half-manifold of L_1 Lyapunov orbits incorporate a ballistic lunar fly-by. This fly-by introduces additional complexity without improving transfer performance, when compared to the left half-manifold. A simple transit near the lunar region does not change the energy of the transfer arc, as the gravitational influence of the Moon is already accounted for within the model.
- When considering transfers that leverage the left half-manifold, two regions of interest appear: one near the target orbit and one at the first apogee prior to Earth fly-by. These locations are regions of interest as they possess low cost transfer solutions.
- Continuation schemes can be applied to non-tangent transfers in order to expand the trade space to other manifold arcs on the same manifold, and to other orbits in

the family. Continuation to various manifold arcs on the same orbit provides larger variation in the solution space, when compared to continuation to other orbits in the family. Though the variation of the transfer space along the family is limited, larger orbits provide lower insertion cost opportunities when compared to smaller orbits in the family.

These key takeaways, along with the transfer characteristics presented, can be leveraged to rapidly construct desired solutions for the mission at hand.

5.2 Future work

While the work presented in this investigation provides great insight into two-maneuver transfers to the L_1 Lyapunov family, other orbits in the cislunar vicinity are also of interest for mission design. A set of tasks that expand the work of this study are proposed:

- The L_1 Halo family shares a common orbit with the L_1 Lyapunov family, as continuation has been proven to be successful from one orbit to another along the same family, it follows that a continuation scheme can be implemented to transition solutions from the planar Lyapunov family to the spatial Halo family.
- Similar structures of interest exist around Earth-Moon L_2 . Hence, an extension of this work, to orbits in the L_2 vicinity, would provide additional insight of interest to mission designers.
- A subsection of the halo family, the Near Rectilinear Halo Orbits (NRHOs), possesses stable or nearly stable orbits which do not have well-defined stable manifolds. Previous authors have implemented methodologies to generate transfers to specific orbits within this range, through the use of other dynamical structures in their vicinity [7]. An expansion of this methodology to the more general case, as well as to L_1 , would allow for the generation of a trade space of solutions to these orbits. Such a trade space would provide insight to designers that wish to leverage these nearly stable orbits.
- The incorporation of intermediate maneuvers are also of interest. This study focused purely on two-maneuver transfers, however, intermediate maneuvers may be imple-

mented to the benefit of performance, or, to meet additional constraints required by the mission scenario.

- Finally, transitioning these solutions to the Ephemeris model is a key validation step. A step required before designers can leverage the structures demonstrated in the real mission scenario.

These additional tasks would provide additional insight into the transfer space from the Earth to orbits in the cislunar vicinity, leading to rapid, informed, mission design.

REFERENCES

- [1] M. Woodward, D. Folta, and D. Woodfork, “Artemis: The first mission to the lunar libration orbits,” NASA/Langley Research Center, 2009.
- [2] R. Funase, S. Ikari, K. Miyoshi, *et al.*, “Mission to earth–moon lagrange point by a 6u cubesat: Equuleus,” *IEEE Aerospace and Electronic Systems Magazine*, vol. 35, pp. 30–44, 3 Apr. 2020, ISSN: 0885-8985. DOI: [10.1109/maes.2019.2955577](https://doi.org/10.1109/maes.2019.2955577).
- [3] D. Reeves, J. Williams-Byrd, M. Simon, *et al.*, “Earth-moon l1 / l2 infrastructure-what role does it play? hat cis-lunar destination team human exploration community workshop on the global exploration roadmap,” 2011.
- [4] *Nasa space science data coordinated archive: Queqiao*. [Online]. Available: <https://nssdc.gsfc.nasa.gov/nmc/spacecraft/display.action?id=QUEQIAO>.
- [5] M. L. Mcguire, S. L. Mccarty, and L. M. Burke, “Power and propulsion element (ppe) spacecraft reference trajectory document,” 2020. [Online]. Available: <http://www.sti.nasa.gov>.
- [6] R. E. Pritchett, “Strategies for low-thrust transfer design based on direct collocation techniques,” Ph.D. dissertation, Purdue University, West Lafayette, Indiana, 2020.
- [7] E. M. Zimovan-Spreen, “Trajectory design and targeting for applications to the exploration program in cislunar space,” Ph.D. dissertation, Purdue University, West Lafayette, Indiana, 2021.
- [8] S. T. Scheuerle, “Construction of ballistic lunar transfers in the earth-moon-sun system,” M.S. thesis, Purdue University, West Lafayette, Indiana, 2021.
- [9] R. R. Rausch, “Earth to halo orbit transfer trajectories,” M.S. thesis, Purdue University, West Lafayette, Indiana, 2005.
- [10] D. C. Folta, T. A. Pavlak, A. F. Haapala, and K. C. Howell, “Preliminary design considerations for access and operations in earth-moon l1/l2 orbits,” NASA/Langley Research Center, 2013.
- [11] D. W. Dunham, R. W. Farquhar, N. Eismont, and E. Chumachenko, “New approaches for human deep-space exploration,” *The Journal of the astronautical sciences*, vol. 60, pp. 149–166, 2 2014, ISSN: 0021-9142. DOI: [10.1007/s40295-014-0025-x](https://doi.org/10.1007/s40295-014-0025-x).
- [12] M. C. Jesick, “Abort options for human missions to earth-moon halo orbits,” NASA/Langley Research Center, 2013.

- [13] J. S. Parker and G. H. Born, “Direct lunar halo orbit transfers,” *The Journal of the astronomical sciences*, vol. 56, pp. 441–476, 4 2012, ISSN: 0021-9142. DOI: [10.1007/BF03256561](https://doi.org/10.1007/BF03256561).
- [14] T. A. Pavlak, “Trajectory design and orbit maintenance strategies in multi-body dynamical regimes,” Ph.D. dissertation, Purdue University, West Lafayette, Indiana, 2013.
- [15] E. Perozzi and A. D. Salvo, “Novel spaceways for reaching the moon: An assessment for exploration,” *Celestial mechanics and dynamical astronomy*, vol. 102, pp. 207–218, 1-3 2008, ISSN: 0923-2958. DOI: [10.1007/s10569-008-9156-3](https://doi.org/10.1007/s10569-008-9156-3).
- [16] G. Gómez, *Dynamics and mission design near libration points. Volume 3, Advanced methods for collinear points*. World Scientific, 2001, ISBN: 1-281-93456-9.
- [17] N. L. Parrish, E. Kayser, S. Udupa, J. S. Parker, B. W. Cheetham, and D. C. Davis, “Survey of ballistic lunar transfers to near rectilinear halo orbit.”
- [18] I. Newton, *Sir Isaac Newton’s Principia*, W. T. Kelvin and H. Blackburn, Eds. J. MacLehose, 1871.
- [19] A. E. Roy, *Orbital motion*, Fourth edition. CRC Press, 2004, ISBN: 0-367-80662-2.
- [20] F. M. Callier, *Linear system theory*, C. A. Desoer, Ed. Springer Science+Business Media, 1991, ISBN: 1-4612-0957-9. DOI: [10.1007/978-1-4612-0957-7](https://doi.org/10.1007/978-1-4612-0957-7).
- [21] C. T. Kelley, *Solving nonlinear equations with Newton’s method*. Society for Industrial and Applied Mathematics, 2003, ISBN: 9780898715460.
- [22] J. E. Gentle, *Numerical Linear Algebra for Applications in Statistics*. Springer, 2012, ISBN: 9780387985428.
- [23] A. E. Roy and M. W. Ovenden, “On the occurrence of commensurable mean motions in the solar system: The mirror theorem,” *Monthly notices of the Royal Astronomical Society*, vol. 115, pp. 296–309, 3 1955, ISSN: 0035-8711. DOI: [10.1093/mnras/115.3.296](https://doi.org/10.1093/mnras/115.3.296).
- [24] H. Araki, R. Beig, and J. Ehlers, *Generating Families in the Restricted Three-Body Problem*. Springer Berlin / Heidelberg, 1997, vol. 52, ISBN: 9783540638025. DOI: [10.1007/3-540-69650-4](https://doi.org/10.1007/3-540-69650-4).
- [25] D. J. Grebow, “Trajectory design in the earth-moon system and lunar south pole coverage,” Ph.D. dissertation, Purdue University, West Lafayette, Indiana, 2010, ISBN: 112415504X.
- [26] R. U. Seydel, *Practical Bifurcation and Stability Analysis*, 3rd ed. 2010. Springer New York, 2010, ISBN: 1-280-39127-8. DOI: [10.1007/978-1-4419-1740-9](https://doi.org/10.1007/978-1-4419-1740-9).

- [27] D. C. Folta, T. A. Pavlak, K. C. Howell, M. A. Woodard, and D. W. Woodfork, “Stationkeeping of lissajous trajectories in the earth-moon system with applications to artemis.”
- [28] C. D. Souza, T. Crain, and F. C. Clark, “Orion cislunar guidance and navigation.”
- [29] *Translunar injection*. [Online]. Available: https://history.nasa.gov/SP-4029/Apollo_18-24_Translunar_Injection.htm#_ftnref1.
- [30] R. T. Eapen, K. C. Howell, and K. T. Alfriend, “Aas 21-310 on the use of zero-momentum surfaces to identify transport opportunities to planar lyapunov orbits.”